

SUPERCOMPUTING IN SCIENCE AND ENGINEERING 2019–2020

IT4Innovations National Supercomputing Center
Ostrava, Czech Republic



Supercomputing in Science and Engineering 2019–2020

Editors: Vit Vondrak, Tomas Kozubek, Branislav Jansik
Language Correction: Renata Plouharova, John Cawley
Ostrava, 2021

Published by VSB – Technical University of Ostrava

Design and typesetting: Nina Kavan

Page count: 94

Edition: 1st

Printed by: Moravapress s.r.o.

Copies: 100

Not for sale

© IT4Innovations National Supercomputing Center

This work is subject to copyright. All rights reserved.

Reproduction or publication of this material, even partial,
is allowed only with the editors' permission.

ISBN 978-80-248-4567-8

SUPERCOMPUTING IN SCIENCE AND ENGINEERING 2019–2020

IT4Innovations National Supercomputing Center
Ostrava, Czech Republic



MINISTRY OF EDUCATION,
YOUTH AND SPORTS

This publication was supported by The Ministry of Education, Youth and Sports from the Large Research Infrastructures project “e-INFRA CZ – LM2018140”.

TABLE OF CONTENTS

TABLE OF CONTENTS	4
MANAGEMENT'S INTRODUCTION	7
THE INFRASTRUCTURE OF IT4INNOVATIONS	9
OPEN ACCESS GRANT COMPETITIONS 2019-2020	10
01 / APPLIED MATHEMATICS	
Advanced Incompressible Flow Simulations for Vortex Identification Jakub Sistek	14
02 / ASTROPHYSICS	
Migration of Giant Planets in Stellar-Irradiated Disks Ondrej Chrenko	18
Thermomechanical Processes in Icy Moons Marie Behounkova	21
03 / EARTH SCIENCES	
Validation and Parallel Benchmarking of the New Radiative Transfer Model Version 3.0 for PALM-4U Urban Climate Model Jaroslav Resler, Pavel Krc	26
Validation of the model PALM-4U Against Observation Campaign in Prague-Dejvice Ondrej Vlcek	28
Assessing the Sensitivities of Urban Climate Model PALM-4U Jan Geletic	31
04 / ENGINEERING	
Numerical Modeling of Load of Structures in Quasi-Static Effect of Wind Ivan Kolos	36

05 / INFORMATICS

Research and Development of Libraries and Tools in the INFRA Lab Petr Strakos	42
Natural Computation-Based Design Techniques for Cellular Automata and Applications Michal Bidlo	45

06 / LIFE SCIENCES

In Silico Drug Design Pavel Hobza	50
Reliable Structural Ensembles of Intrinsically Disordered Proteins Jozef Hritz	52
Photoacoustic Tomography of the Breast Executed on Nvidia DGX-2 and Fat GPU Nodes Jiri Jaros	56
Fiji Bioimage Informatics on HPC – Path to Exascale Michal Krumnikl	59
Interactions of Macrocyclic Inhibitors with STING Protein – Novel Route to Treat Cancer and Chronic Hepatitis B Lubomir Rulisek	62

07 / MATERIAL SCIENCES

Novel 2D Magnetic Semiconducting Materials; Multiscale Design of Novel Rare Earth Free Permanent Magnets Dominik Legut	68
Energetics and Dynamics of the Initial Step of the Birch Reduction Pavel Jungwirth	70
Accuracy and Precision for Extended Systems Jiri Klimes	74
Large-Scale Benchmarking of Non-Covalent Interactions – London Dispersion and Sigma-Hole Bonds Jan Rezac	77
Structure and Properties of Novel Nanocomposites Formed by Intermetallic Compounds Mojmir Sob	79

08 / PLASMA AND PARTICLE PHYSICS

Laser-Driven Acceleration of Charged Particles Martin Matys	86
Particle-in-Cell Simulations of Combined Thermionic and Secondary Electron Emission Michael Komm	89

Dear readers,

The third edition of our Supercomputing in Science and Engineering publication is now in your hands. We present to you 21 selected scientific projects that took place between 2019 and 2020 and were made possible thanks to the computing systems located at IT4Innovations National Supercomputing Center.

The demand for computational resources is steadily increasing, and each new open access grant competition confirmed that the scientific community in the Czech Republic relies on powerful supercomputers and builds its scientific work on them. In 2019–2020, we supported 409 projects through seven open access grant competitions, among which we have distributed almost 500,000,000 core hours. The projects covered a variety of scientific domains; some of them offer answers in the search for new energy sources, others, for example, develop new materials or medicines. You can read about these and many more in the following pages.

Our supercomputers have therefore contributed significantly to the achievement of many research goals of scientists from all over the Czech Republic. The increased demand for computational resources led us to increase computing capacity by purchasing two new supercomputers in 2019. In the spring, an NVIDIA DGX-2 system specialising in AI computations was installed; a few months later, the 849 TFlop/s Barbora supercomputer was added, bringing the latest supercomputing technology to our users.

What is more, in 2019 we also succeeded in a Europe-wide competition to host one of the EuroHPC petascale systems to be built as part of the EuroHPC Joint Undertaking. Subsequently, an open selection procedure was held for the supplier of this system, and the winner was Hewlett Packard Enterprise. The new supercomputer is named Karolina, and will offer a theoretical peak performance of 15.7 PFlop/s to the scientific community and industry from August 2021. At the same time, in 2019, we became a member of the LUMI consortium (Large Unified Modern Infrastructure), a consortium of 10 European countries which, together with the European Commission, is currently acquiring and will soon operate a supercomputer of the same name located in Kajaani, Finland. It will undoubtedly be among the absolute world leaders in terms of performance, and will be available to our users as early as 2022.

In 2020, the e-INFRA CZ large research infrastructure was also created by merging IT4Innovations with two other e-infrastructures: CESNET and CERIT-SC operated by Masaryk University. e-INFRA CZ is registered in the Czech Republic's Roadmap of Large Infrastructures for Research, Experimental Development and Innovation managed by the Ministry of Education, Youth and Sports of the Czech Republic; it offers complex capacities and resources for transfer, storage, and processing of scientific data to all entities engaged in research, development, and innovation across the Czech Republic.

We hope that you will continue to support us in the future, and that our supercomputers will continue to help you achieve breakthroughs in your research.

Vit Vondrak
Managing Director

Tomas Kozubek
Scientific Director

Branislav Jansik
Supercomputing Services Director

THE INFRASTRUCTURE OF IT4INNOVATIONS

IT4Innovations operates the largest supercomputing facility in the Czech Republic in the public sphere, currently four clusters named Salomon, Anselm, Barbora and NVIDIA DGX-2.

The supercomputer infrastructure was installed in several stages. The first cluster, Anselm (94 TFlop/s), was installed in temporary mobile units in May 2013. The supercomputer Salomon (2 PFlop/s) became operational in September 2015 and was ranked No. 40 on the TOP500 list of the most powerful supercomputers in the world. In 2019 Barbora (849 TFlop/s) and the NVIDIA DGX-2 system specialized for artificial intelligence (130 TFlop/s and 2 PFlop/s for AI) were installed. All clusters are now permanently

located in the new IT4Innovations building, which has a 500 m² server room.

The construction of the IT4Innovations building started in December 2012, the administrative section being completed in March 2014. The physical infrastructure supporting the supercomputers has fully redundant power and cooling, using direct hot water cooling (2 x 600 kW), cold water cooling (200, 400 and 600 kW), and heat recovery (up to 380 kW) for building heating to lower operational costs. The backup power is provided through diesel rotary UPSs, each with a capacity of 2.5 MVA. The Internet connection is 2x40 Gb/s connected to two different endpoints of the CESNET network.



OPEN ACCESS GRANT COMPETITIONS 2019–2020

Researchers can apply for computational resources of IT4Innovations supercomputers through Open Access Grant Competitions. These are announced three times a year and are open to employees of research, scientific, and educational organisations based in the Czech Republic.

In 2019 and 2020, IT4Innovations supercomputers were used for 409 projects within 7 Open Access Grant Competitions. Researchers applied for a total of nearly 630 million core hours. Given the high demand for computing time relative to the available resources, the allocation committee proceeded to reduce the allocations of the projects evaluated. The reductions affected all projects proportionally.

The committee decided on the allocations based on the results of an evaluation of scientific readiness,

computational readiness, and socioeconomic impact. Within the 13th up to the 19th Open Access Grant Competitions, nearly 500 million core hours were distributed across 409 projects.

Projects in material sciences received the most computational resources, totalling 64%. Life sciences projects received the next largest amount of resources (18%), and the third largest amount was shared by three disciplines, with a total of 4% (see Figure 1 on the opposite page).

By institution, IT4Innovations supercomputers were mostly used by scientists from VSB – Technical University of Ostrava (25%), followed by researchers from the Czech Academy of Sciences (21%) and CEITEC – Central European Institute of Technology (18%); see Figure 2 on the opposite page.

629 881 868 requested core hours

7 open access grant competitions 409 supported projects

498 019 000 allocated core hours

Figure 1. Computational Resources Allocated within the Open Access Grant Competitions in 2019–2020 by Scientific Discipline

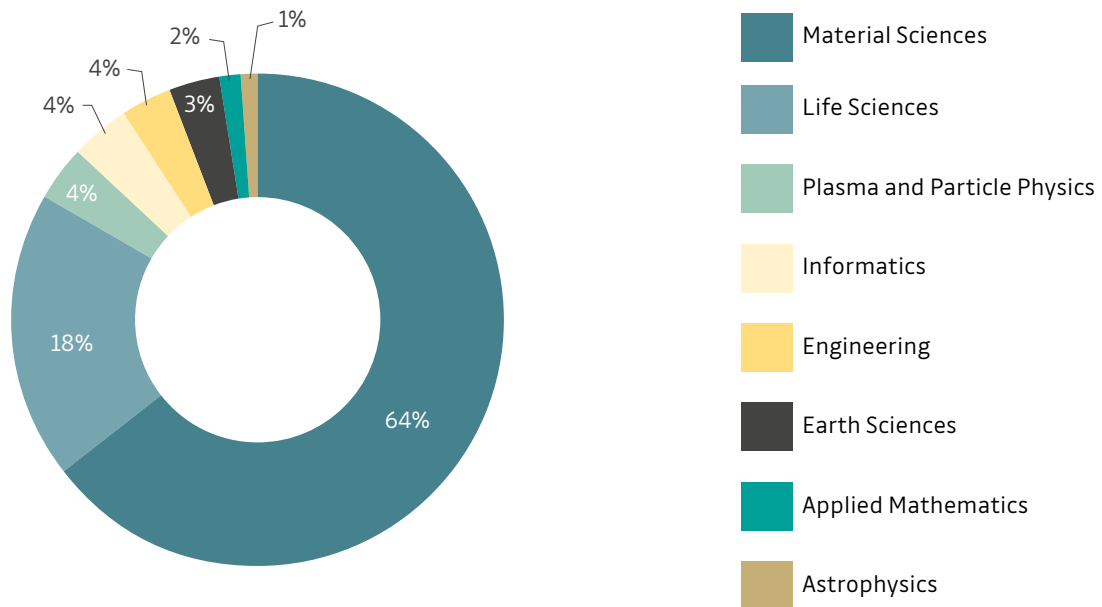
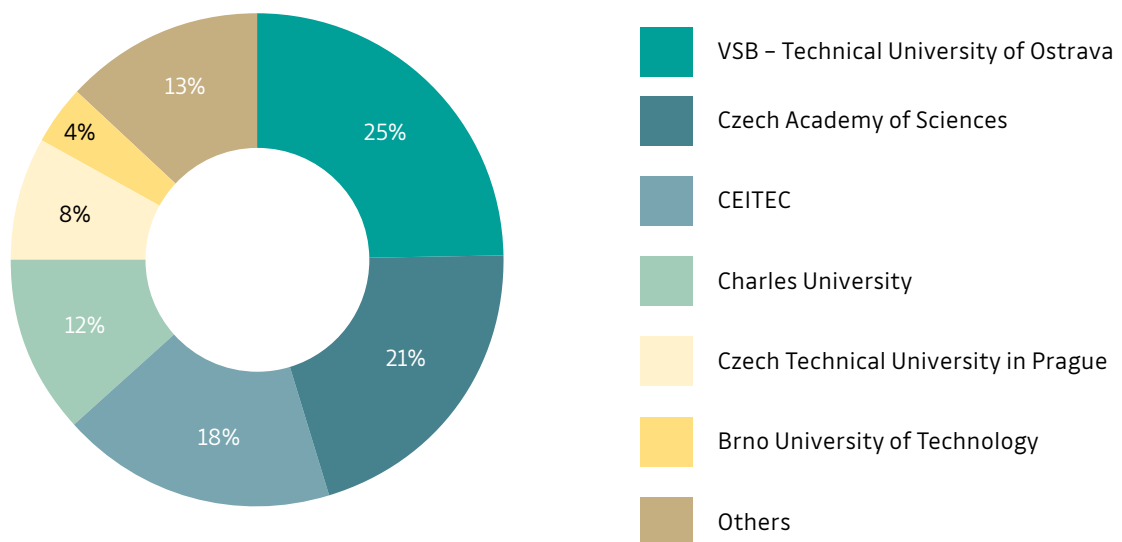


Figure 2. Computational Resources Allocated within the Open Access Grant Competitions in 2019–2020 by Institution



APPLIED MATHEMATICS

ADVANCED INCOMPRESSIBLE FLOW SIMULATIONS FOR VORTEX IDENTIFICATION

Research institution
Czech Academy of
Sciences, Institute of
Mathematics

Principal investigator
Jakub Sistek

Researchers
Martin Hanek,
Pavel Kus

Project ID
OPEN-17-40

Introduction

The main aim of the project was performing high-resolution computational fluid dynamics simulations of prototype problems of incompressible viscous flows. The primary goal of these simulations was to generate high-resolution 3-D data with vortical structures. These data have subsequently been used for the development of new methods for flow-field analysis and vortex identification and visualisation, supporting the research project Advanced flow-field analysis granted by the Czech Science Foundation. Unsteady flows considering very fine computational meshes are required for this purpose as the analysis is based on the velocity gradient tensor.

The computations were performed using an in-house parallel finite element solver based on the pressure correction method and multilevel domain decomposition, with the aid of an existing parallel implementation of the method in the open-source BDDCML library. A subsequent goal of the project was the further development of the computational method and optimization of the BDDCML library for large numbers of computer cores.

Methods and Results

Obtaining reliable datasets for flow-field analysis and feature detection by numerical methods represents a challenge from the mathematical viewpoint, namely the solution of unsteady Navier-Stokes equations (NSE) in 3D with a very high mesh resolution. While a variety of methods have been developed for computational fluid dynamics (CFD), our parallel solver relies on the finite element method (FEM) for unstructured meshes [1,2]. A critical problem in this as well as other numerical methods with implicit time-stepping is how to efficiently solve the system of nonlinear algebraic equations arising at every time step. To this end, we have combined FEM with a variant of the pressure-correction method (see e.g. the review in [3]), which reduces solving the large systems of nonlinear equations to a sequence of smaller linear problems for velocity components and pressure. We have used the multilevel version of the Balancing Domain Decomposition by Constraints (BDDC) method for the sequence of the arising problems for pressure.

The main prototype flow we solved within the project was the unsteady incompressible flow around

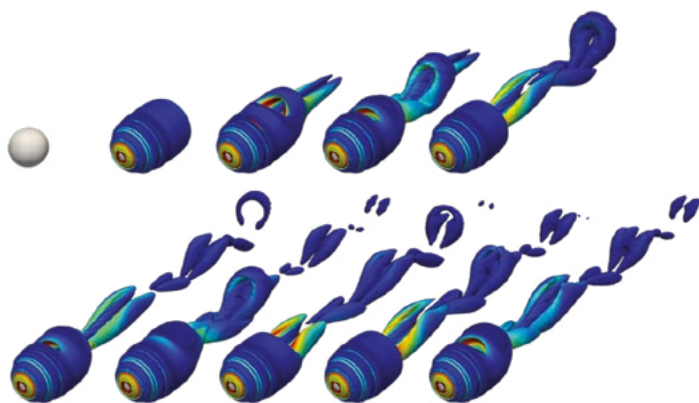


Figure 1. Incompressible flow around a sphere at Reynolds number 300. Vortices in the wake of the sphere are visualized by the magnitude of the vector of average corotation ([4], isovalue 0.1) and coloured by the magnitude of vorticity. Flow after time in seconds: 0, 50, 70, 75, 80 (top row), 90, 100, 110, 150, and 200 (bottom row).

a sphere at Reynolds number 300. We studied the problem on two computational meshes with different resolutions. The smaller one contained approximately 1.8 million unknowns, whilst the larger one contained approximately 15 million unknowns. These meshes were divided into 16 and 128 subdomains, and the corresponding problems were solved using 16 and 128 CPU cores of the supercomputer Salomon at IT4Innovations National Supercomputing Center in Ostrava, the Czech Republic.

In Figure 1, we present several snapshots of the flow. Vortical structures behind the sphere are visualized by means of average corotation [4]. These results have subsequently been used for the development of new advanced methods for flow-field analysis. In particular, a modification of the popular Q criterion [5], Q_w , has been tested on this dataset (see Figure 2). Details are available in [6].

Within the project, we have also developed a multi-level variant of the BDDC method suitable for solving the linear systems with non-symmetric matrices arising from the Navier-Stokes equations. Large-scale scalability tests were performed on Salomon as well, and the results are published in [7].

Conclusion

Within the project, we have managed to perform challenging parallel simulations of incompressible flows. Computed datasets were used for the development of new advanced methods for flow-field analysis, namely for identification and visualisation of vortices and high-strain-rate zones. These methods have been implemented into our open-source Vortex Analysis Library (VALIB). We have also performed a number of scalability tests of the proposed multi-level extension of the BDDC method for problems with non-symmetric matrices.



Figure 2. Vortices identified by Q , Q_w and Q_M (isovalue 0.1). The criterion Q_w is optimal, see [6] for details.

References

- [1] Sístek, J., Cirak, F. Parallel iterative solution of the incompressible Navier-Stokes equations with application to rotating wings. *Computers & Fluids*. 2015, 122, 165–183. DOI: 10.1016/j.compfluid.2015.08.026.
- [2] Sístek, J. A parallel finite element solver for unsteady incompressible Navier-Stokes equations. In David Šimurda and Tomáš Bodnár, editors, *Proceedings of Topical Problems of Fluid Mechanics*. 2015, Prague, Czech Republic, February 11–13, 2015, pages 193–198. Institute of Thermomechanics AS CR, 2015.
- [3] Guermond, J., Mineev, P., Shen, J. An overview of projection methods for incompressible flow. *Computer Methods in Applied Mechanics and Engineering*. 2006, 195, 6011–6045. DOI: 10.1016/j.cma.2005.10.010.
- [4] Kolar, V., Sístek, J., Cirak, F., Moses, P. Average corotation of line segments near a point and vortex identification. *AIAA Journal*. 2013, 51, 2678–2694. DOI: 10.2514/1.J052330.
- [5] Hunt, J. C. R., Wray, A. A., Moin, P. Eddies, Streams, and Convergence Zones in Turbulent Flows, pp. 193–208, Center for Turbulence Research, Stanford, 1988, Report CTR-S88.
- [6] Kolar, V., Sístek, J. Vortex and the balance between vorticity and strain rate. *International Journal of Aerospace Engineering*. 2019, Article ID 1321480. DOI: 10.1155/2019/1321480.
- [7] Hanek, M., Sístek, J., Burda, P. Multilevel BDDC for incompressible Navier-Stokes equations. *SIAM Journal on Scientific Computing*. 2020, 42, C359–C383. DOI: 10.1137/19M1276479.

ASTROPHYSICS

MIGRATION OF GIANT PLANETS IN STELLAR-IRRADIATED DISKS

Research institution
Charles University,
Astronomical Institute

Principal investigator
Ondrej Chrenko

Project ID
OPEN-16-50

Introduction

Planets form in protoplanetary disks. These disks, composed of gas (99%) and dust (1%), surround young stars and provide material for growing planets. Moreover, their gravity is substantial enough to perturb the orbits of embedded planets and cause a process known as planet migration [1]. A planet is said to be migrating when its orbital distance with respect to the central star changes over time (inward migration pushes the planet closer to the star; outward migration shifts the planet farther away from the star). Planet migration is therefore an important evolutionary phase that co-determines the orbital properties of newborn planets. It is valuable to compare theoretical predictions for planet migration with the observed population of exoplanets because such comparisons allow a deepening of the understanding of the processes that shaped planetary systems in our galaxy, including our own Solar System.

For example, there is a long-standing mismatch between the theory and observations concerning giant planets (similar to Jupiter or Saturn). Theoretical and numerical models [e.g. 2] often predict inward migration of giant planets that is relatively fast (compared to the lifetime of protoplanetary disks), and thus the majority of giant planets should orbit close to their stars. This however contradicts astronomical observations which tell us that there are a substantial number of giant planets orbiting at several astronomical units [3] (members of this population are referred to as 'cold Jupiters'). Therefore, the theory of planet migration clearly requires improvement.

[4] suggested that the inward migration of giant planets could be slowed down or even reversed by the following interplay: A giant planet carves a gap in the disk along its orbit. As the gap opens, its outer edge

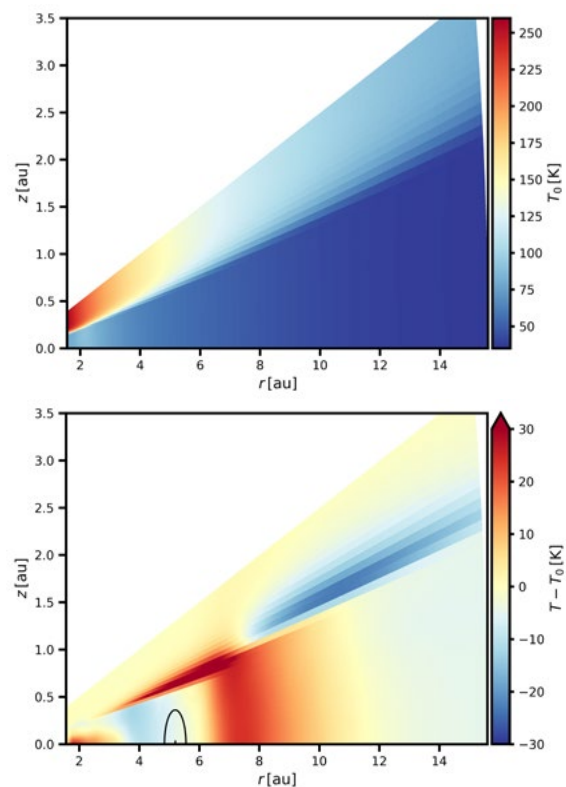


Figure 1. Top: Temperature in a gas disk irradiated by the central star (located at $r=0, z=0$ au). The figure shows a slice through a single vertical plane of the 3D disk; the orbital midplane coincides with the horizontal axis. The disk has an optically thin atmosphere (the rapidly varying colour gradient in the upper third of the disk) and an optically thick interior (blue) into which the stellar irradiation cannot directly penetrate. Bottom: A Jupiter-mass planet is placed at $r=5.2, z=0$ au. The figure now shows a temperature difference with respect to the top panel (i.e. how the temperature changes after planet insertion). The black curve shows the extent of the planetary Hill sphere. As the gap is opened, the stellar irradiation penetrates deeper into the disk, which results in the overheated (red) column of gas between 6 and 10 au. As the overheated region starts to expand vertically, it shadows a part of the outer disk which cools down (the blue strip between 8 and 15 au).

receives an increased amount of stellar irradiation, and the local temperature increases. Consequently, the outer gap edge becomes 'puffed up', its gravitational back-reaction on the planet is reduced, and the inward migration slows down. Since [4] explored the proposed mechanism via simplistic 2D simulations, I focused in this project on verifying the mechanism via realistic 3D simulations with radiation transfer (see Fig. 1).

Methods and Results

The problem was simulated on computers of IT4Innovations using the hydrodynamic computer code Fargo3D [5] (<https://bitbucket.org/fargo3d/public>). The gaseous component of the protoplanetary disk was modelled as an ideal fluid on a staggered spherical mesh. I extended Fargo3D to account for the energy evolution of the disk, including the radiative diffusion and radially ray-traced stellar irradiation. The planet was treated as an embedded point mass generating a gravitational potential. The computer code was fully parallelized using a domain decomposition strategy and a hybrid combination of MPI and OpenMP. A typical simulation was launched over ~500 CPU cores and consumed ~50,000 CPU hours.

I explored the dependence of the described effects on the planet mass and disk viscosity. For each set of parameters, I numerically evolved the star-disk-planet system until a quasi-equilibrium was reached (typically after several thousand orbital timescales). Subsequently, I analysed the perturbed disk structure (namely the temperature excess caused by the gap opening) and I measured the gravitational torque exerted by the disk material onto the planet. The torque is a direct measure of the migration rate, and I compared the obtained torque with a reference set of simulations in which the stellar irradiation was neglected.

The results (Fig. 2) suggest that the reduction of inward migration due to the stellar-irradiated gap edge exhibits a complex dependence on the width and depth of the gap, which scales with the planet mass (more massive planets open wider and deeper gaps). For masses $>1 M_J$ (where M_J is the mass of Jupiter), there is no torque reduction. In the mass range $0.25-1 M_J$, the torque reduction becomes more prominent with decreasing planet mass. In other words, the reduction becomes stronger as the gap becomes

narrower and shallower and the temperature excess recedes towards the planet. For masses $0.1-0.25 M_J$, the reduction becomes weaker with decreasing planet mass because the gap starts to vanish, and the temperature excess diminishes accordingly. Similar behavior can be recovered by changing the disk viscosity (while keeping the planet mass fixed) because the gap becomes narrower with increasing viscosity.

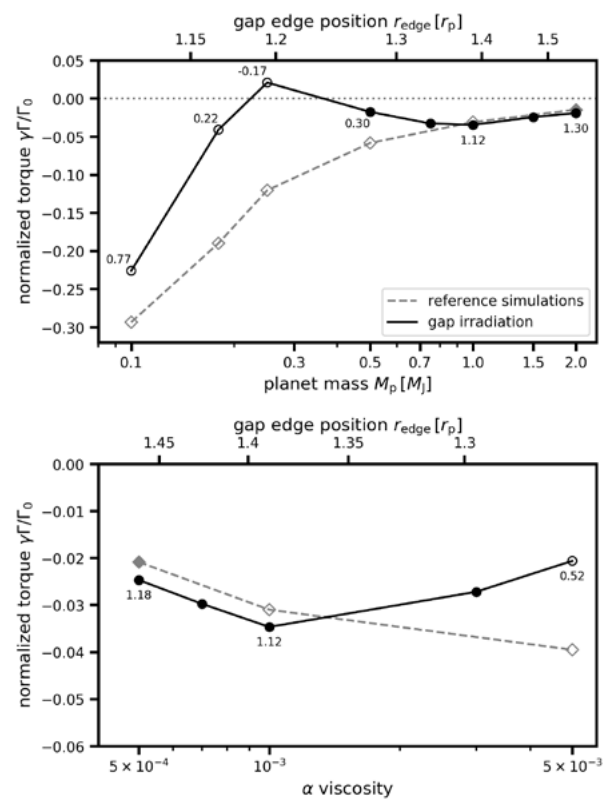


Figure 2. Gravitational torque (vertical axis) exerted by the disk onto an embedded planet. Dependences on the planet mass (top) and disk viscosity (bottom) are shown by the respective horizontal axes. For comparison, the distance of the outer gap edge from the planet is shown by the secondary horizontal axis in each panel. The black solid line and circles show measurements from simulations with stellar irradiation. The grey dashed line and diamonds represent measurements from simulations without stellar irradiation. Negative torque value means inward migration. The figure demonstrates that gap edge irradiation reduces the magnitude of the torque (and therefore slows the migration down), especially for planet masses that are $<1 M_J$. The most prominent torque reduction appears for $0.25 M_J$.

Conclusion

By means of 3D computer hydrodynamic simulations with radiation transfer, I explored the interactions of giant planets with gaseous protoplanetary disks irradiated by the central star. The aim was to improve the match between observations of cold Jupiters (orbiting at several astronomical units) and the theory of planet migration (in which the explanation of the origin of cold Jupiters is troublesome). I focused on a situation where a giant planet opens a gap in the disk along its orbit, the outer gap edge becomes efficiently heated by the irradiating flux from the central

star (Fig. 1), and the structural changes of the outer gap edge slow down the inward migration.

I found that, overall, the reduction of inward migration is less efficient than predicted in the 2D simulations of [4] but I was able to identify several intervals of the parametric space for which the inward migration is indeed substantially stalled (Fig. 2). For the standard disk viscosity $\alpha=10^{-3}$, I concluded that the torque reduction is the most efficient for moderately wide and deep gaps. Therefore, Saturn-mass planets can easily survive planet migration at separations >1 au (where au is the astronomical unit) if their gap is irradiated. The results were published in [6].

References

- [1] Goldreich, P., Tremaine, S. The excitation of density waves at the Lindblad and corotation resonances by an external potential. *The Astrophysical Journal*. 1979, 233, 857–871. DOI: 10.1086/157448.
- [2] Nelson, R. P., Papaloizou, J. C. B., Masset, F., Kley, W. The migration and growth of protoplanets in protostellar discs. *Monthly Notices of the Royal Astronomical Society*. 2000, 318, 18–36. DOI: 10.1046/j.1365-8711.2000.03605.x.
- [3] Fressin, F., Torres, G., Charbonneau, D., et al. The False Positive Rate of Kepler and the Occurrence of Planet. *The Astrophysical Journal*. 2013, 766(2), 81. DOI: 10.1088/0004-637X/766/2/81.
- [4] Hallam, P.D., Paardekooper, S.-J. Investigating the possibility of reversing giant planet migration via gap edge illumination. *Monthly Notices of the Royal Astronomical Society*. 2018, 481(2), 1667–1678. DOI: 10.1093/mnras/sty2336.
- [5] Benitez-Llambay, P., Masset, F. FARGO3D: A New GPU-oriented MHD Code. *The Astrophysical Journal Supplement*. 2016, 223, 11. DOI: 10.3847/0067-0049/223/1/11.
- [6] Chrenko, O., Nesvorný D. Migration of gap-opening planets in 3D stellar-irradiated accretion disks. *Astronomy & Astrophysics*. 2020, 642, A219. DOI: 10.1051/0004-6361/202038988.

THERMOMECHANICAL PROCESSES IN ICY MOONS

Research institution
Charles University,
Faculty of
Mathematics and
Physics

Principal investigator
Marie Behounekova

Researchers
Ondrej Soucek,
Klara Kalousova,
Katerina Pleiner
Sladkova

Project ID
OPEN-16-29

Introduction

Jupiter's moon Europa attracts a lot of attention as a primary target of search for life beyond the Earth, which is demonstrated by the planned missions to Jupiter's system (ESA's JUICE) and to Europa in particular (NASA's Europa Clipper). With a radius of 1560 km, Europa is the smallest among the Galilean moons. Its interior is differentiated into an iron-rich core, a silicate mantle, and a hydrosphere. The deep and salty internal ocean is in direct contact with the silicate mantle and, sheltered from space by the outer ice shell, provides an environment hospitable to life beyond the Earth. The outer ice shell is expected to be between a few kilometers and several tens of kilometers thick depending on the efficiency of heat transfer and the internal heat sources. The tectonically modified shell with a geologically young surface points to recent or ongoing geological activity in Europa's interior.

Tidal deformation and heat transport in the shell are thought to be the main processes shaping the ice shells and surfaces of icy moons. The tidally induced

periodic deformation can be particularly pronounced for thin shells that are mechanically separated from the deeper parts by ocean, as is present on Europa. Many of the observed surface lineaments are driven by the tidally induced tension and compression. On several of them, a lateral offset (displacement of one side of the fault with respect to the other) of several kilometers has been measured. Such observations indicate that a strike-slip, i.e. horizontal motion on almost vertical fractures, has taken place on Europa. To explain the gradual development of lateral offset on already existing faults, a conceptual model called 'tidal walking' has been proposed by Hoppa et al. (1999). In this model, the offset is produced by an interplay between normal and shear tidal forces acting on the fault plane. The normal forces open and close the fault and, consequently, facilitate or impede the lateral motion induced by the shear force (see Figure 1 for a detailed explanation).

To test the hypothesis of tidal walking, we have developed a numerical tool, which treats a part of Europa's ice shell with an embedded strike-slip fault.

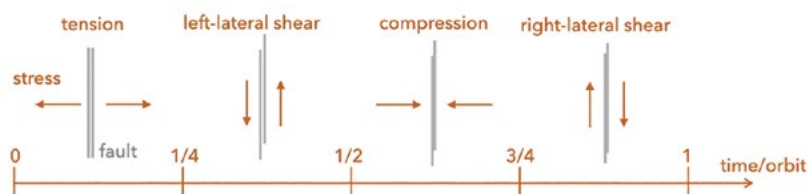


Figure 1. A simplified diagram of the tidal walking process: the tension opens the existing fault, then the left-lateral shear produces an offset (enabled by the opened fault). In the third quarter of the orbital period, the compression closes the fault preventing or diminishing the right-lateral offset. In this case, all processes result in small left-lateral offset. The specific tidal forces and final (if any) offset are dependent on the orientation and position of the fault on Europa's surface.

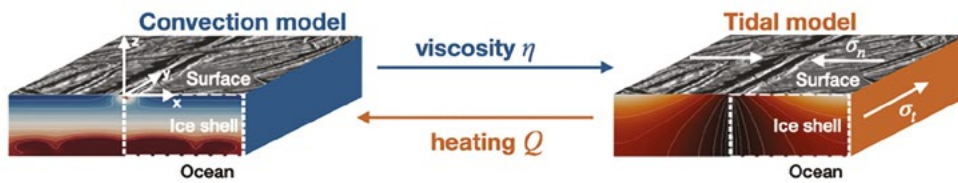


Figure 2. Diagram of the model: the tidal model (right) solves for the strike-slip motion due to diurnal tides, and the convection model (left) computes the long-term thermal evolution. The models exchange information through heating Q and viscosity h . For both models, the actual computational domain is two-dimensional and it is indicated by the dashed rectangles. The left boundary is the fault plane, the top boundary is the surface, the bottom boundary is the shell-ocean interface, and the right boundary is an interior surface within the shell.

Methods and Results

To describe the behavior of strike-slip faults' surroundings on Europa, we have to couple processes on two different timescales: the fault formation timescale (tens of thousands of years) and the diurnal tides timescale (days). The coupled model consists of two parts:

- i) a convection model based on the work of Kalousova et al. (2016) solving the evolution of the ice shell via thermal convection with non-Newtonian viscosity, where tidally induced frictional heating at the fault and shear heating are considered as energy sources,
- ii) a tidal model describing a viscoelastic continuum with an embedded fault plane subjected to tidal stresses with the viscosity determined by the convection model – this model provides the heating for the convection model.

These two parts are, therefore, coupled through viscosity and heating, see Figure 2.

The ice shell convection code is based on Boussinesq approximation with composite rheology (Kalousova et al., 2016). The tidal model solves the mass and momentum balances of the incompressible Maxwell medium, with the preexisting fault subjected to externally prescribed diurnal stresses: shear $\sigma_t = \sigma_0 \sin(\omega t)$ and normal $\sigma_n = \sigma_0 \sin(\omega t - \phi)$, where σ_0 is forcing stress amplitude, ω is orbital frequency, t is time, and ϕ is the phase shift between the normal and shear stress. Thanks to the geometry of Europa's faults and symmetry of the problem, we can reduce the computational domain to a 2D rectangle (denoted by a dashed white line in Figure 2). We approximate the fault's behavior through pseudo-plasticity simulat-

ing Mohr-Coulomb friction. Such an approach allows self-consistent determination of the fault activation depth. Numerical solutions for both components are carried out using the open-source finite element software package FEniCS (www.fenicsproject.org).

We performed a parametric study concentrating on the key parameters: the amplitude of forcing stresses σ_0 , their mutual phase shift ϕ , the thickness of the ice shell and the friction coefficient. We evaluate the results through observable quantities: the accumulated surface offset at the fault and the heat flux anomaly on the surface.

A synthesis of results for an intermediate value of friction coefficient (0.4) is presented in Figure 3. The observable offset (denoted by walking figures) is defined as $>100\text{m}$ in 100 kyr. The prevailing standing figures indicate that it is challenging to obtain an observable offset within a chosen range of parameters. For a 1km thick shell, the models that successfully predict the offset feature a fault that is activated through the entire ice shell and high slip velocities. Such a setting probably leads to a high thermal signature, which cannot be quantified since a numerical stabilization had to be used.

The thermally activated case (5km thick ice shell and 600 kPa loading stress amplitude) exhibits a remarkable behavior, an observable offset and high heat flux might be obtained even though the fault is not mechanically activated throughout the entire ice shell. In this case, a substantial frictional heating on the fault warms its surroundings up to the melting temperature, raising a hot plume from the bottom of the ice shell. Consequently, an area of increased temperature and thermally-reduced viscosity is observed,

which produces an observable offset and considerable surface heat flux. For more details, see the complete results in Sladkova et al. (2020).

Conclusion

We showed that the tidal walking model could produce a lateral surface offset of a few kilometres over one hundred thousand years if the fault penetrates the high viscosity part of the ice shell. The conditions

favorable for whole shell penetration (thin shell, large stresses) are likely not met in the present-day Europa. However, earlier in Europa's history, the shell was thinner and the stresses might have been larger, thus indicating that the tidal walking process could have modified Europa's surface. In addition, we have demonstrated that the inclusion of thermo-mechanical coupling is key for understanding the behavior of strike-slip faults on Europa.

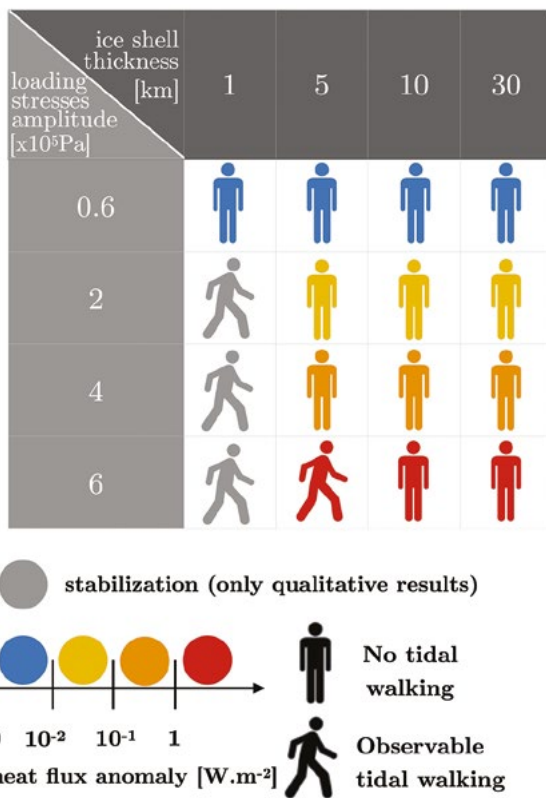


Figure 3. Table summarizing the results for various ice shell thicknesses (columns) and loading stresses amplitudes (rows). The walking/standing figure corresponds to the model producing visible offset or not, respectively. The color (red to blue) represents value of the heat flux anomaly on the fault. Grey color denotes simulations with stabilization giving only quantitative results.

References

- [1] Hoppa, G., Tufts, B. R., Greenberg, R., Geissler, P. Strike-slip faults on Europa: Global shear patterns driven by tidal stress. *Icarus*. 1999, 141(2), 287–294. DOI: 10.1006/icar.1999.6185.
- [2] Kalousova, K., Soucek, O., Tobie, G., Choblet, G., Cadek, O. Water generation and transport below Europa's strike-slip faults. *Journal of Geophysical Research: Planets*, 121(12), 2444–2462. DOI: 10.1002/2016JE005188.
- [3] Sladkova, K., Soucek, O., Kalousova, K., Behounkova, M. Tidal walking on Europa's strike slip faults – insight from numerical modeling. *Journal of Geophysical Research: Planets*. 2020, 125(8), e2019JE006327. DOI: 10.1029/2019je006327.

EARTH SCIENCES

VALIDATION AND PARALLEL BENCHMARKING OF THE NEW RADIATIVE TRANSFER MODEL VERSION 3.0 FOR PALM-4U URBAN CLIMATE MODEL

Research institution
Czech Academy of Sciences, Institute of Computer Science; Charles University, Faculty of Mathematics and Physics

Principal investigator
Jaroslav Resler,
Pavel Krc

Researchers
Jan Geletic,
Vladimir Fuka

Project ID
OPEN-15-69

Introduction

PALM is an open-source large-eddy atmospheric model developed jointly by Leibniz University of Hannover and other European academic institutions. The Institute of Computer Science is the main author of the urban surface energy balance model (USM) and the multi-reflection radiative transfer model (RTM) for PALM [2].

The current PALM version (6.0) contains an overall upgrade of the RTM (version 3.0), which increases the scope of modelled processes and enables modelling of larger areas by utilizing new algorithms with improved efficiency and scalability and reduced computational complexity. During the development and testing of this new complex model, we needed to run multiple simulations to verify the correctness and convergent properties of the model using different scenarios, and to test the scalability and efficiency of the parallelization. This new version was described in the Geoscientific Model Development journal (GMD) [1], [2].

Methods and Results

Microscale atmospheric modelling of urban areas requires a detailed three-dimensional description of all surfaces and materials within the modelled area and a model of energy balance between these surfaces and the atmosphere, in addition to modelling of atmospheric processes themselves. An important component of this energy balance is solar and thermal ra-

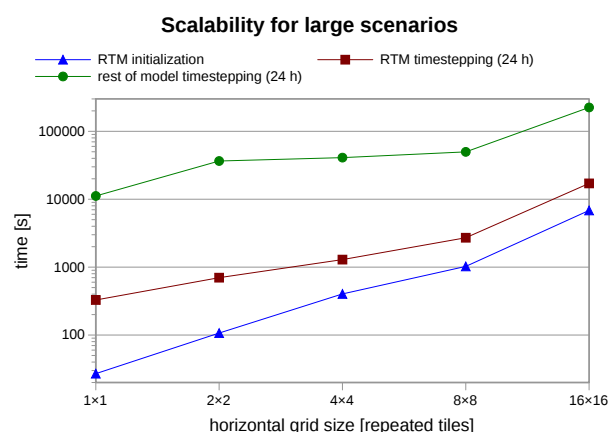


Figure 1. A double-logarithmic presentation of the computation time while simulating progressively larger domains (by means of horizontal quadruplication). Each simulation uses a constant number of processes per horizontal tile.

diation. Shading by buildings and structures, multiple reflections and spatial interaction with plant canopy play a significant role on street level and these processes are not fully captured by traditional radiation models utilized mostly by mesoscale atmospheric models.

The currently available models of radiative interactions in the complex urban environment either significantly simplify the modelled processes or are limited to small simulation areas due to missing or limited parallelization. The developers of the RTM for PALM

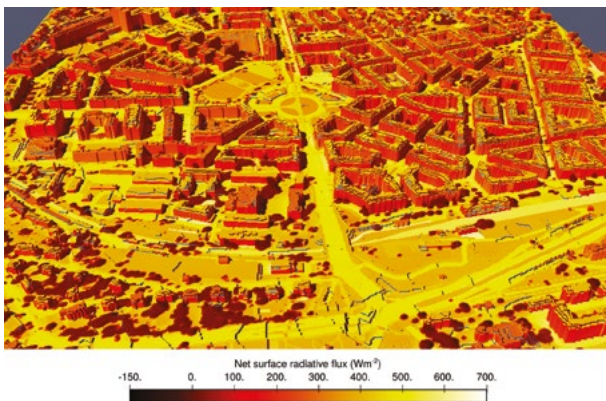


Figure 2. A 3-D representation of instantaneous net short-wave + long-wave radiative fluxes in a large urban scenario. A north-oriented view of the inner domain of the Prague-Dejvice validation scenario.

thus decided to develop such a model from scratch (RTM 1.0, see [3]). The first version of RTM became a standard component of PALM in 2016 and it was able to simulate domains to the extent of a few hundred grid points in each dimension. However, for the next planned simulations, domains with thousands of grid points in each dimension were required, and the authors had to look for innovations in model principles and design to reach this performance.

A newly developed RTM version 3.0 adds a number of important features: a new representation of the sky for direct and diffuse solar irradiance and sky thermal irradiance; a new raytracing algorithm with reduced complexity and optimized MPI communication; a new discretization scheme for reflected and surface thermal radiation with reduced CPU and memory complexity and greater scalability; provision of resolved radiative fluxes for calculation of human thermal comfort; absorption and emission of longwave radiation by plant leaves (in addition to shortwave radi-

ation) and provision of radiative heat fluxes for modelling transpiration of resolved plant canopy.

A set of experiments was performed in order to verify the convergence of the model with respect to various parameters, and to demonstrate the superior scalability in actual simulations. The first set of simulations described how fast the modelled results approach the finest-resolution scenario when the resolution of the scenario is increased progressively. The second set of simulations demonstrated the convergence with increasing angular resolution of the novel angular discretization method. The third set of simulations verified the convergence and error limits for the increasing number of reflections in the multiple-reflection model.

Another set of simulations tested the scalability of the model for large scenarios using progressively larger, horizontally tiled domain setups. The largest simulated scenario had a size of 6400 x 4096 with a 2 m resolution and was simulated using 8129 parallel processes (see Figure 1). The fifth set of simulations tested the efficiency of the model parallelization on a single scenario that was simulated using a progressively larger number of parallel processes. Many of these simulations exceeded the capacity of the ICS in-house cluster. It was necessary to perform them in a supercomputing centre, and we successfully used the Salomon supercomputer at IT4Innovations for this purpose.

Conclusion

The new RTM model for PALM was developed, and the performed tests successfully demonstrated the extended capabilities and significantly improved scalability of this new model version. With its size and the interconnect architecture, the Salomon supercomputer provided the opportunity to perform all the necessary tests, including the very large setups. The model was described and the test results were published in an article [1] in the top-class scientific journal GMD.

References

- [1] Krc, P., Resler, J., Sührling, M., Schubert, S., Salim, M. H., and Fuka, V. Radiative Transfer Model 3.0 integrated into the PALM model system 6.0. *Geosci. Model Dev.* 2021, 14(5), 3095–3120. DOI: 10.5194/gmd-14-3095-2021.
- [2] Maronga, B., Banzhaf, S., Burmeister, C., Esch, T., Forkel, R., Fröhlich, D., Fuka, V., Gehrke, K. F., Geletic, J., Giersch, S., Gronemeier, T., Groß, G., Heldens, W., Hellsten, A., Hoffmann, F., Inagaki, A., Kadasch, E., Kanani-Sührling, F., Ketelsen, K., Khan, B. A., Knigge, C., Knoop, H., Krc, P., Kurppa, M., Maamari, H., Matzarakis, A., Mauder, M., Pallasch, M., Pavlik, D., Pfafferoth, J., Resler, J., Rissmann, S., Russo, E., Salim, M., Schrempf, M., Schwenkel, J., Seckmeyer, G., Schubert, S., Sührling, M., von Tils, R., Vollmer, L., Ward, S., Witha, B., Wurps, H., Zeidler, J., and Raasch, S. Overview of the PALM model system 6.0. *Geosci. Model Dev.* 2020, 13(3), 1335–1372. DOI: 10.5194/gmd-13-1335-2020.
- [3] Resler, J., Krc, P., Belda, M., Juruš, P., Benesova, N., Lopata, J., Vlcek, O., Damaskova, D., Eben, K., Derbek, P., Maronga, B., and Kanani-Sührling, F. PALM-USM v1.0: A new urban surface model integrated into the PALM large-eddy simulation model. *Geosci. Model Dev.* 2017, 10(10), 3635–3659. DOI: 10.5194/gmd-10-3635-2017.

VALIDATION OF THE MODEL PALM-4U AGAINST OBSERVATION CAMPAIGN IN PRAGUE-DEJVICE

Research institution
Czech Hydrometeorological Institute; Czech Academy of Sciences, Institute of Computer Science; Charles University, Faculty of Mathematics and Physics

Principal investigator
Ondrej Vlcek

Researchers
Nina Benesova,
Michal Belda,
Vladimir Fuka,
Jaroslav Resler,
Krystof Eben,
Jan Geletic,
Pavel Krc,
Martin Rosecky

Project IDs
OPEN-15-64,
OPEN-18-23,
OPEN-19-44

Introduction

Investigation of the urban climate has become very important during recent years and aims to help urban city authorities to plan efficient and economically feasible mitigation strategies to counteract the adverse effects of the urban heat island phenomenon (UHI). Different modelling approaches have been used for this purpose and models based on computational fluid dynamic (CFD) techniques represent the most advanced method. Two main approaches are used in this category. The Reynolds-averaged Navier–Stokes equations (RANS) method calculates only the mean flow while the turbulence is fully parameterized, while the large-eddy simulation (LES) approach models explicitly the resolved turbulent flow and parameterizes only the subgrid-scale unresolved turbulence. The LES approach is more computationally demanding, but many studies have shown that it significantly outperforms RANS for simulations in complex urban environments.

PALM is a well-known and widely used atmospheric model based on LES principle. In recent years, the PALM model system has been rapidly developed in terms of its capability to simulate physical processes within urban environments [Resler2017], [Maronga2020]. Some examples in this regard are energy-balance solvers for building and land surfaces, a radiative transfer model to account for multiple reflections and shading [Krc2021], a plant-canopy model to consider the effects of plants on flow (thermo)dynamics, and a chemistry transport model to enable simulation of air quality. Consequently, this development provides the first available LES-based model able to realistically simulate the complex urban environment. With this new rapid development, the need for a thorough validation of the model against detailed observations became urgent. Three specialized observational campaigns took place for this purpose in Prague-Dejvice, Berlin, and Hamburg. In this project, we evaluate the model against observations in Prague-Dejvice.



Figure 1. Simulated fine domain with 2 m resolution. The 3D view shows an area around Vítězné náměstí square from the south-west. The extent of the domain is 1440 × 1440 m, the colours show the modelled surface temperature on 19 June 2018 at 14:00 UTC.

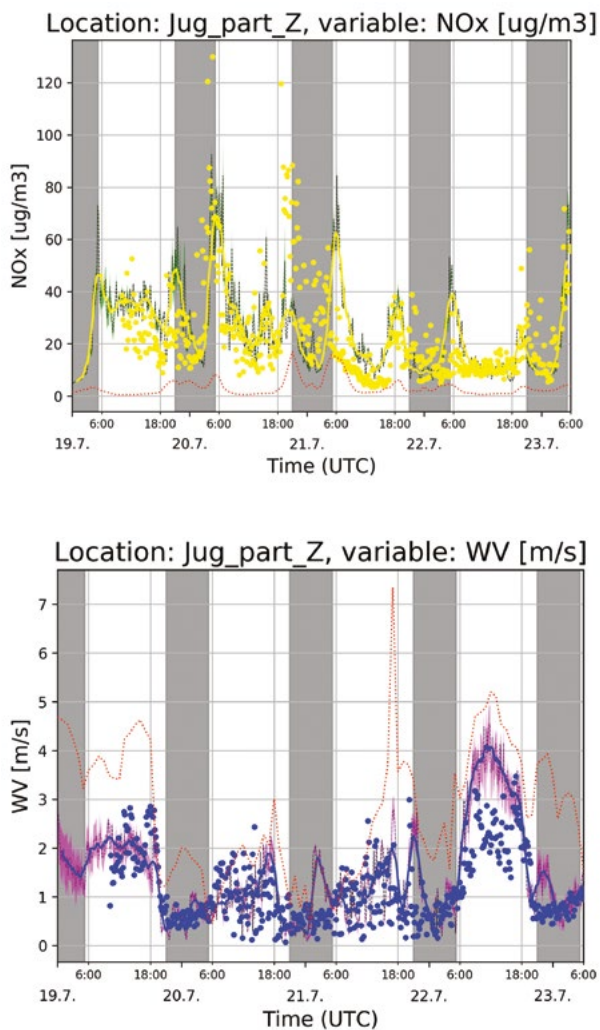


Figure 2. The modelled (solid line) and the observed (dots) wind speed (left) and concentrations of NO_x (right) on the west pavement in the street of Jugoslávských partyzánů on 19–23 June, 2018. The modelled values represent a one hour moving average while the black dashed line shows the 10-minute moving average. The cyan/green area represents the spread of the modelled values on grids adjacent to the evaluated grid cell and thus represents spatial variability of the modelled value. The thin dotted red line shows the corresponding background values from the mesoscale model and it provides information about contribution of the microscale model.

Methods and Results

This study provides a thorough evaluation of modelled meteorological, air chemistry, and ground and wall-surface quantities against dedicated in-situ measurements taken in an urban environment in Prague-Dejvice during the summer and winter of 2018. Measurements included monitoring of air quality and meteorology in street canyons, surface temperature scanning with infrared cameras, and monitoring of wall heat fluxes. The realistic modelling done by the LES model requires a sufficient domain extent, in the range of a few km, to allow the development of the large turbulent eddies in the model. To describe the convection flows, it must also vertically cover the whole boundary layer, which expands more than 2 km up from the surface during hot summer days. The PALM model was thus configured in two nested domains with a resolution of 10 m and 2 m with a horizontal extent of 400 × 400 and 720 × 720 grid boxes respectively. The simulations were parallelized to 880 MPI processes while we also tested the configuration with 1975 MPI processes during the preparatory phase. On the borders of the outer domain, the PALM model was driven by boundary conditions obtained from simulations of a mesoscale model. The PALM simulations were performed for multiple days within two summer and three winter observational episodes characterized by different atmospheric conditions. Moreover, many of the preparatory testing simulations were necessary to run to identify and tackle model issues as well as to find the optimal setting of the model and the experiment. As every simulation of one day required from two to four computational days on 880 processor cores depending on meteorological conditions, performing of all needed simulations represented a challenge. The simulations thus were split into three parts. The first part was processed in the in-house cluster in ICS, and the other two parts were processed at IT4Innovations (Czech Rep.) and HLRN (Germany) supercomputing centres. All the results were then gathered and post-processed in the ICS facilities. The results of this validation campaign were published in a paper [Resler2020]. The simulation results also served for analysis of the thermal exposure published in [Geletic2021].

Conclusion

The results of this study represent the first thorough comparison of the integrated LES-based urban model against an extensive set of observations gathered during a dedicated observational campaign. They significantly extend the validation done in [Resler2017] in the design of the observation campaign as well as in modelling design. They prove that this modelling approach can provide reliable and

realistic simulations which enables the model to serve the purpose of practical urbanistic studies. This study also allowed the finding and testing of a suitable configuration of the model and experiment, and to fix many modelling issues during the preparatory phase of the experiment. Finally, the simulations revealed many particular issues which considerably influence the direction of the model development in future, as well as the design of future specialised observational campaigns.

References

- [1] Resler, J., Eben, K., Geletic, J., Krc, P., Rosecky, M., Sührling, M., Belda, M., Fuka, V., Halenka, T., Huszar, P., Karlicky, J., Benesova, N., Doubalova, J., Honzakova, K., Keder, J., Napravnikova, S., and Vlcek, O. Validation of the PALM model system 6.0 in real urban environment; case study of Prague-Dejvice, Czech Republic. *Geosci. Model Dev. Discuss.* [preprint]. 2020. DOI: 10.5194/gmd-2020-175.
- [2] Geletic, J., Lehnert, M., Krc, P., Resler, J., Krayenhoff, E. S. High-resolution modelling of thermal exposure during a hot spell: A case study using PALM-4U in Prague, Czech Republic. *Atmosphere*. 2021, 12(2), 1–29. DOI: 10.3390/atmos12020175.
- [3] Maronga, B., Banzhaf, S., Burmeister, C., Esch, T., Forkel, R., Fröhlich, D., Fuka, V., Gehrke, K. F., Geletic, J., Giersch, S., Gronemeier, T., Groß, G., Heldens, W., Hellsten, A., Hoffmann, F., Inagaki, A., Kadasch, E., Kanani-Sührling, F., Ketelsen, K., Khan, B. A., Knigge, C., Knoop, H., Krc, P., Kurppa, M., Maamari, H., Matzarakis, A., Mauder, M., Pallasch, M., Pavlik, D., Pfafferoth, J., Resler, J., Rissmann, S., Russo, E., Salim, M., Schrempf, M., Schwenkel, J., Seckmeyer, G., Schubert, S., Sührling, M., von Tils, R., Vollmer, L., Ward, S., Witha, B., Wurps, H., Zeidler, J., and Raasch, S. Overview of the PALM model system 6.0. *Geosci. Model Dev.* 2020, 13, 1335–1372. DOI: 10.5194/gmd-13-1335-2020.
- [4] Krc, P., Resler, J., Sührling, M., Schubert, S., Salim, M. H., and Fuka, V. Radiative Transfer Model 3.0 integrated into the PALM model system 6.0. *Geosci. Model Dev.* 2021, 14, 3095–3120. DOI: 10.5194/gmd-14-3095-2021.
- [5] Resler, J., Krc, P., Belda, M., Jurus, P., Benesova, N., Lopata, J., Vlcek, O., Damaskova, D., Eben, K., Derbek, P., Maronga, B., and Kanani-Sührling, F. PALM-USM v1.0: A new urban surface model integrated into the PALM large-eddy simulation model. *Geosci. Model Dev.* 2017, 10, 3635–3659. DOI: 10.5194/gmd-10-3635-2017.

ASSESSING THE SENSITIVITIES OF URBAN CLIMATE MODEL PALM-4U

Research institution
Czech Academy of Sciences, Institute of Computer Science; Czech Hydrometeorological Institute; Charles University

Principal investigator
Jan Geletic

Researchers
Jana Radova, Jaroslav Resler, Pavel Krc, Krystof Eben, Michal Belda, Vladimir Fuka, Ondrej Vlcek

Project ID
OPEN-15-67

Introduction

Investigation of the urban climate, and especially that of the urban heat island (UHI) phenomenon, still faces new challenges. Even with increasing computational capabilities and geographic information systems (GIS), there is a need for standardized research methods. Furthermore, research output should be applicable in practise. Microscale meteorological and climate models have been increasingly used for simulations of real urban city environments and especially the impacts of changes in the city structure on the environmental conditions that affect the inhabitants. In this context, various UHI mitigation measures are being considered, with greening of the environment

as a typical example. Application of these measures, however, needs some prior information about their potential effectiveness or a cost-benefit analysis. For that, it is important to know how sensitive the environment is to the city layout (e.g., building height or street width) and the material-specific parameters used to describe urban surfaces (e.g., reflectivity or roughness). Currently, the demand for scientifically-based urban climate studies is growing, particularly model-based studies that can provide reliable projections on a city or street-level scale.

Solutions can be provided using modern microscale meteorological models, such as the PALM model system. PALM is a part of the large-eddy simulation

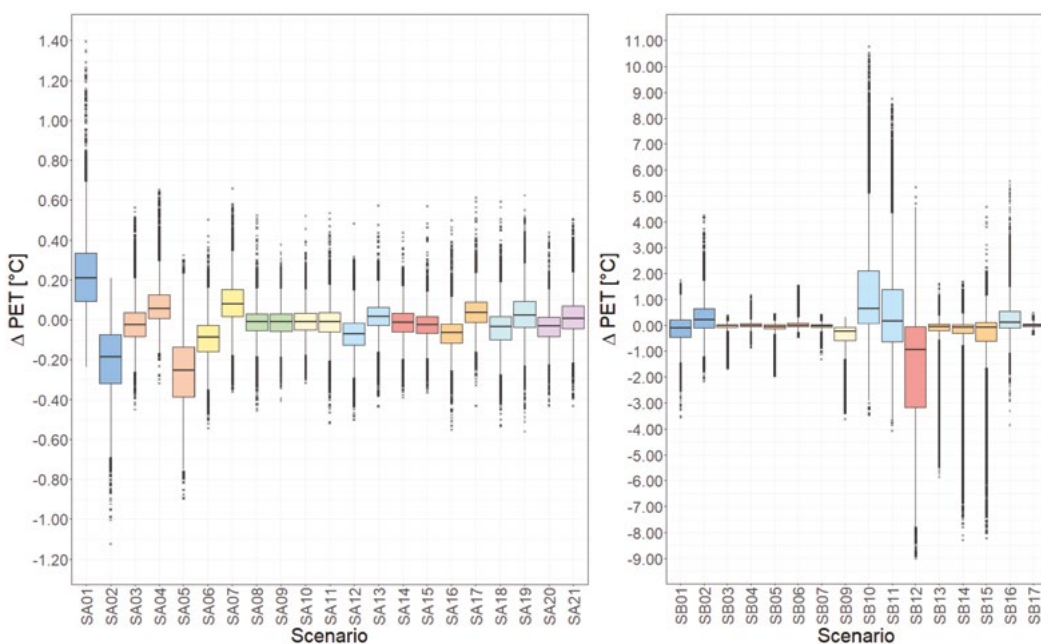


Figure 1. Sensitivity of physiological equivalent temperature (PET) in modelled scenarios. Values represent gridbox differences (scenario-baseline) of 24-hour averages. Whiskers: values within 1.5x interquartile range; crosses: outliers.

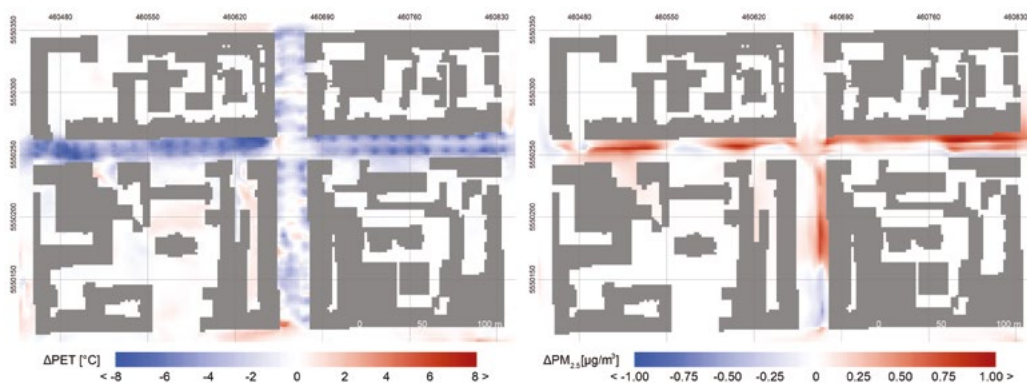


Figure 2. Example of opposite behaviour of thermal comfort and air quality indicators represented by average daily difference in PET and PM2.5 for a new alley scenario.

(LES) branch of computational fluid dynamics (CFD), in which the large turbulent eddies are explicitly resolved and simulated, unlike RANS where all turbulent eddies are parameterized. The LES method has been shown to perform better in resolving instantaneous turbulence structures in a complex urban environment. However, LES-based models are computationally demanding and HPC resources are needed for processing of realistic studies. The next issue for realistic simulation is the need for detailed model inputs. To the best of our knowledge, comprehensive sensitivity studies on how LES results for urban environments depend on input data accuracy are non-existent to date, and this study aims to fill this gap.

Methods and Results

The PALM model system consists of the PALM model core, several embedded modules, and PALM-4U (PALM for urban applications) components which have been specifically developed for modelling the urban environment. The PALM model core resolves the non-hydrostatic, filtered, incompressible Navier-Stokes equations for wind (u , v , w) and scalar quantities (potential temperature, water vapor mixing ratio, passive scalar) on a staggered Cartesian grid in Boussinesq-approximated form. One of the assets of PALM is its excellent scalability for massively parallel computer architectures (up to 50,000 processor cores) by means of hybrid MPI/OpenMP parallelization. The simulations of this study were configured in two nested domains with a horizontal extent of 400×400 and 400×256 grids, and were parallelized on 480 MPI processes.

For evaluating the influence of the parameter changes, a baseline simulation was performed in which the parameters tested were set to real values, that is, values measured or estimated based on materials used in the actual buildings and other surfaces in the domain. Then, we assessed the sensitivity of air and surface temperature, mean radiant temperature (MRT), physiological equivalent temperature (PET) and PM2.5 within the PALM model system as a response to the modification of basic surface material parameters as well as to common UHI mitigation strategies. For this we performed a set of semi-idealized model simulations for a diurnal cycle in a city quarter in Prague (37 in total).

The first set of scenarios shows the highest sensitivity and hence the importance of the correct setting of the radiation parameters albedo and emissivity. This can be expected as solar radiation is the main source of energy in the surface energy budget. Additionally, unlike some other parameters, radiation parameters are different for all surfaces. In addition to albedo and emissivity, thermal conductivity of walls and volumetric heat capacity of the materials play an important role. Other parameters show a limited average effect on the diurnal timescale which can however be quite significant in some parts of the day, such as surface roughness in the morning hours and window fraction in the evening. In the context of the chosen domain, with only a small percentage of the surface covered by vegetation, changing soil moisture by 20% is shown to be negligible overall except for surface temperature in the high-sun part of the day. Individual parts of the domain with larger coverage of vegetation show greater influence. Example of summary

sensitivity output is shown in Figure 1.

Urban vegetation is found to be the most effective measure when considering reduction of both physical and biophysical temperature indicators. Conversely, grey city scenarios that reduce the amount of urban vegetation show significant worsening of thermal comfort. Urban greenery is very often found an effective mitigation tool for UHI; recent studies have reported a vegetation-induced cooling of more than 3°C. However, some studies show that for the best effect it is necessary to combine several measures and also to consider that different parts of the city may need different measures. One of the most important results of our analysis is that it confirms an opposite behaviour of thermal comfort and air quality indicators (see Fig. 2).

Conclusion

This analysis shows that the proper setting of urban surface parameters is crucial for high-resolution LES models of the urban environment, and that collecting this large amount of data is an essential part of the modelling technique. High temporal and spatial variability also shows the importance of using truly local information for each area of interest. When assessing the very local influences, e.g., pedestrian-level thermal comfort, the local settings play a major role and thus need to be considered for proper evaluation. Altogether, the LES method proves to be an asset thanks to its capability to fully resolve the flow and to consider heterogeneity in the modelling domain. Hence, LES modelling results can be readily applied to support urban planning when aiming to mitigate UHI in urban neighbourhoods.

References

- [1] Belda, M., Resler, J., Geletic, J., Krc, P., Maronga, B., Sührling, M., Kurppa, M., Kanani-Sührling, F., Fuka, V., Eben, K., Benesova, N., and Auvinen, M. Sensitivity analysis of the PALM model system 6.0 in the urban environment. *Geosci. Model Dev. Discuss.* 2020, in review. DOI: 10.5194/gmd-2020-126.
- [2] Maronga, B., Banzhaf, S., Burmeister, C., Esch, T., Forkel, R., Fröhlich, D., Fuka, V., Gehrke, K. F., Geletic, J., Giersch, S., Gronemeier, T., Groß, G., Heldens, W., Hellsten, A., Hoffmann, F., Inagaki, A., Kadasch, E., Kanani-Sührling, F., Ketelsen, K., Khan, B. A., Knigge, C., Knoop, H., Krc, P., Kurppa, M., Maamari, H., Matzarakis, A., Mauder, M., Pallasch, M., Pavlik, D., Pfafferott, J., Resler, J., Rissmann, S., Russo, E., Salim, M., Schrempf, M., Schwenkel, J., Seckmeyer, G., Schubert, S., Sührling, M., von Tils, R., Vollmer, L., Ward, S., Witha, B., Wurps, H., Zeidler, J., and Raasch, S. Overview of the PALM model system 6.0. *Geosci. Model Dev.* 2020, 13, 1335–1372. DOI: 10.5194/gmd-13-1335-2020.
- [3] Resler, J., Krc, P., Belda, M., Juruš, P., Benesova, N., Lopata, J., Vlcek, O., Damaskova, D., Eben, K., Derbek, P., Maronga, B., and Kanani-Sührling, F. PALM-USM v1.0: A new urban surface model integrated into the PALM large-eddy simulation model. *Geosci. Model Dev.* 2017, 10, 3635–3659. DOI: 10.5194/gmd-10-3635-2017.

ENGINEERING

NUMERICAL MODELING OF LOAD OF STRUCTURES IN QUASI-STATIC EFFECT OF WIND

Research institution
VSB – Technical
University of Ostrava,
Faculty of Civil
Engineering

Principal investigator
Ivan Kolos

Researchers
Vladimira Michalcova,
Lenka Lausova

Project IDs
OPEN-15-35,
OPEN-17-13,
OPEN-19-6

Introduction

Wind load is one of the climatic loads that must be taken into account when designing almost any building or structure. Investigating the effects of wind on a structure requires dealing with turbulent flow, as most structures occur in the atmospheric boundary layer (ABL), which is characterized by a high degree of atmospheric turbulence and there are high gradients of velocity and intensity of turbulence. In addition, buildings often have a non-aerodynamic shape (bluff body), which further contributes to the formation of other vortices in the flowing wind.

In addition to the shape of the structure, the degree of its wind load is also affected by the surface roughness of the structure, i.e. the height, shape and location of the roughening elements [1]; it is the influence

of surface roughness on the wind load of the structure that is the subject of the long-term interest of our research team, and we have investigated it within this project. We focused on cylindrical structures with a circular cross-section (Fig. 1). This is a shape that often occurs in many areas of civil engineering, especially in industrial and bridge structures [2]. The cylinder, among semi-aerodynamic (or bluff) bodies, is still a commonly and often studied subject, as it generates a dynamically complex wake despite its simple geometry. The nature of the wind flow is described by the Reynolds number Re , on which the drag force of the object being flown around also depends. The degree of wind load on the structure can be expressed by the so-called drag coefficient c_d , which depends not only on Re , but is significantly affected by the surface roughness of the flowed body. Another important indicator in the design of structures is the distribution of the pressure load on the surface of the bluff body, which is defined as the pressure coefficient c_p . The long-term goal, solved within this and possible follow-up projects, is to compile a methodology of numerical calculation, which will enable reliable determination of the drag coefficient c_d and pressure coefficient c_p on the surface of the bluff body in the most efficient way, i.e. in a sufficiently short time and without excessively high demands on computing power.

Methods and Results

From the point of view of computational fluid dynamics (CFD) we use 2 procedures for the solution, which are described in a paper [3]: the first is computationally very demanding modelling of flow around a real shape of a rough surface (Fig. 2), the second is

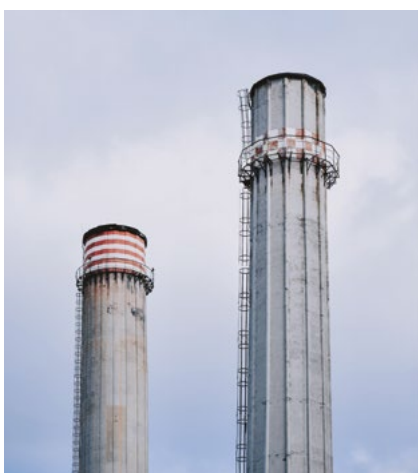


Figure 1. An example of circular cross-section objects with a corrugated surface exposed to wind.

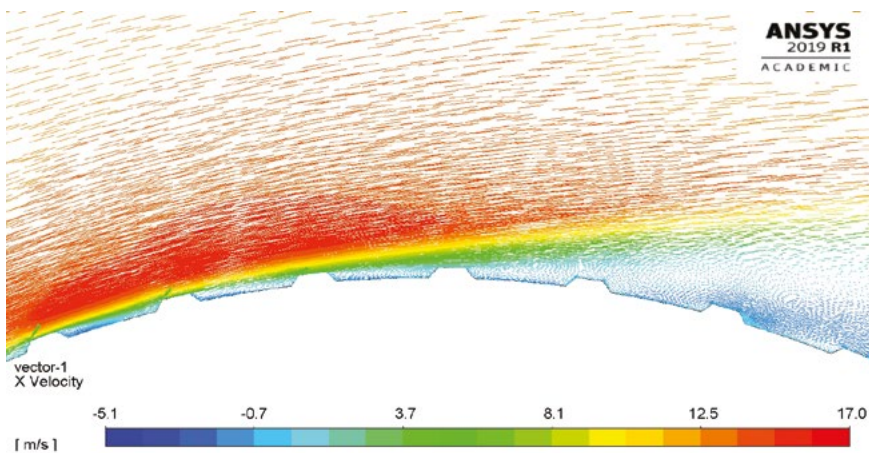


Figure 2. Detail of the rough surface with the velocity vectors.

a more computationally efficient approximate model, in which the real shape of the rough surface is expressed by a numerical approximation. We work with both 3D and 2D models. For calculations we use the finite volume method implemented in the commercial software ANSYS Fluent, in which the entire solution process from the generation of computational mesh to the analysis of results is carried out.

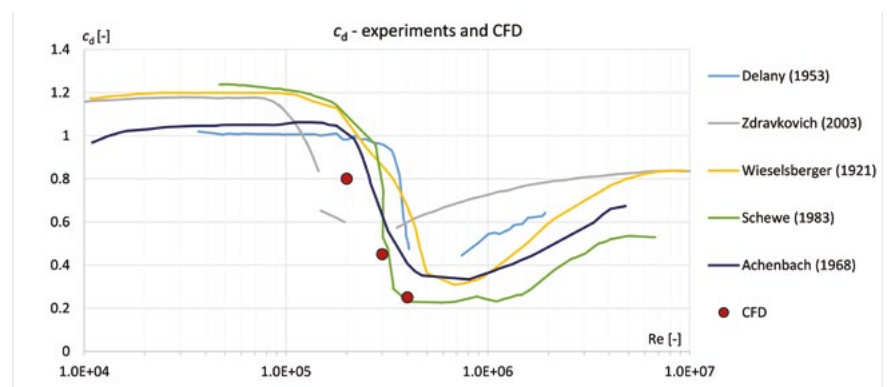
The essence of CFD calculation is the solution of governing equations: the continuity equation and the momentum equation (Navier-Stokes). The number of solved equations is directly proportional to the number of cells in the computational mesh. The number of cells in the mesh results from the size of the roughening elements and the dimensions of the smallest vortices that can occur in the flowing air. In order, the computational network of the unit forms up to tens of millions of cells, and from this number follows the time and computational complexity of the solution. The finite volume method is quite well parallelizable,

so it is advantageous to implement the solution on HPC.

Since we are simulating flow problems in ABL, this is the so-called critical regime in which there is a significant decrease in c_d due to a change in the boundary layer of the bypassed body. It is the change of the boundary layer that causes problems in numerical modelling. A certain complication and challenge, especially for 3D tasks, is the need to create a sufficiently fine mesh and set the parameters of the mathematical model of turbulent flow.

The results of the calculations so far give us hope that the chosen solution strategy will lead to the intended goal. For example, we were able to capture the c_d decrease in the critical regime relatively well using the LES turbulent model, (Figure 3). This means that we have approached an acceptable setting of calculation parameters (i.e. mutual combination of mesh, turbulence model and solution parameters).

Figure 3. Relationship of drag coefficient c_d and Reynolds number. Comparison with wind tunnel measurements.



Conclusion

Although we managed to publish some of the partial results [4,5], we can say that we are basically still at the beginning. The reason for the relatively slow progress is the extraordinarily time-consuming calculations and the high sensitivity of the numerical models

to a small change in the input parameters. Despite the difficulties described, however, we consider the researched topic to be meaningful, and we are determined to continue it. The use of CFD in design of buildings will make it possible in practice to effectively solve wind load of buildings with types of rough surfaces that are not described in technical standards.

References

- [1] Butt, U., Jehring, L., Egbers, C. Mechanism of drag reduction for circular cylinders with patterned surface. *International Journal of Heat and Fluid Flow*. 2014, 45, 128–134. DOI: 10.1016/j.ijheatfluidflow.2013.10.008.
- [2] Cheng, X., Zhao, L., Ge, Y., Dong, R., Demartino, C. Wind effects on rough-walled and smooth-walled large cooling towers. *Advances in Structural Engineering*. 2017, 20(6), 843–864. DOI: 10.1177/1369433216664354.
- [3] Michalcova, V., Lausova, L. Numerical approach to determination of equivalent aerodynamic roughness of Industrial chimneys. *Computers and Structures*. 2017. DOI: 10.1016/j.compstruc.2017.03.013.
- [4] Kolos, I., Michalcova, V., Lausova, L. Numerical modeling of the pressure coefficient of the circular cylinder. *Mathematical Methods in the Applied Sciences*. 2020, 43(13), 7579–7594. DOI: 10.1002/mma.5901.
- [5] Kolos, I., Michalcova, V., Lausova, L. Numerical Analysis of Flow Around a Cylinder in Critical and Subcritical Regime. *Sustainability*. 2021, 13(4), 2048. DOI: 10.3390/su13042048.

INFORMATICS

RESEARCH AND DEVELOPMENT OF LIBRARIES AND TOOLS IN THE INFRA LAB

Research institution
IT4Innovations
National
Supercomputing
Center

Principal investigator
Petr Strakos

Researchers
Ondrej Vysocky,
Ondrej Meca, Radim
Vavrik, Tomas Panoc,
Marketa Hrabankova,
Milan Jaros, Alena
Jesko, Tomas
Brzobohaty, Lubomir
Riha

Project ID
OPEN-15-29

Introduction

One of the goals of the Infrastructure Research (INFRA) laboratory is to bring improvements and extensions of available tools that can support users of the IT4Innovations clusters and boost their research. The key topics in the INFRA lab are energy-efficiency of parallel applications, development of the ESPRESO numerical library, and development of visualisation tools for scientific data.

The energy-efficiency topic focuses on the measurement and tuning of HPC applications in terms of possible energy savings without any performance penalty. This project is based on the MERIC library [1] for application behaviour profiling and tuning, and RADAR tools [2] for visualisation and analysis of MERIC's output data. The MERIC library and the RA-

DAR tools were extended with new features such as scalable methods of storing and reading output data and advanced visualisation techniques to analyse the results.

ESPRESO is a highly parallel library for solving large scale engineering problems. The ESPRESO project is already a well-established project at IT4Innovations; It is one of the flagships. The aim of this project was to vectorize and accelerate key parts of ESPRESO's assembler and implement interfaces for various direct and iterative solvers, as an alternative to the default FETI solver.

The visualisation tools topic focuses on leveraging the open-source 3D creation suite Blender [3] in conjunction with other open source simulation and post-processing tools. This lets us bring accurate re-

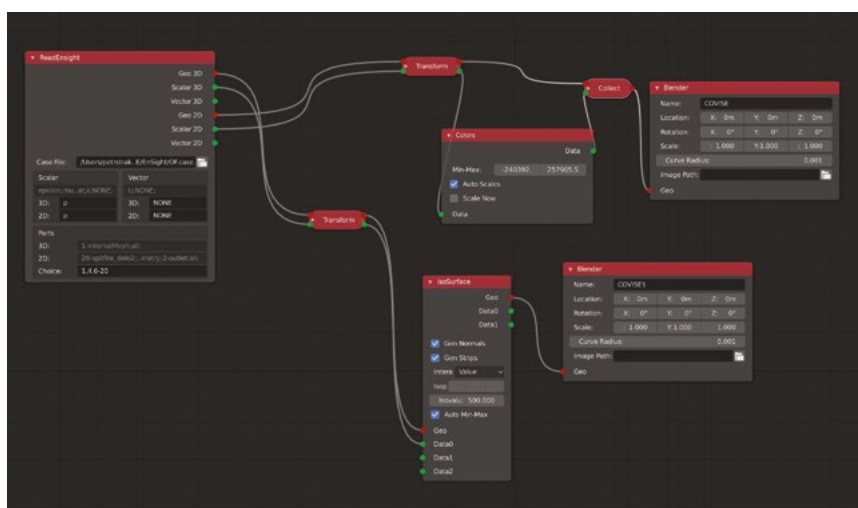


Figure 1. Structure of nodes in Blender-Convise editor.

sults of large scale simulation problems to life in a visually pleasing form. To be able to reach a high level of realism in visualisations, a powerful path tracing rendering method is used. We utilize the CyclesPhi [4] renderer, which is our modified version of Blender's Cycles renderer. CyclesPhi provides methods for effective utilization of non-accelerated as well as accelerated nodes of a supercomputer. The aim here was to integrate the functionality of simulation and post-processing tools into Blender, so the results of typical engineering tasks such as CFD or structural analysis could be visualized by path trace rendering.

Methods and Results

Energy-efficiency: For storing MERIC's output data, the tools newly supports the HDF5 data format, which is designed for parallel storing and processing of data stored in one object. Together with other improvements in the MERIC library, it was also necessary to add new visualisation techniques to be able to provide similar information as competitive tools. MERIC, as well as the RADAR tools, was successfully tested on the new IT4Innovations ARMv8 server TaiShan. During the project, the developed tools have been used for optimization of several HPC applications, some of which are presented in research papers [5,6,7].

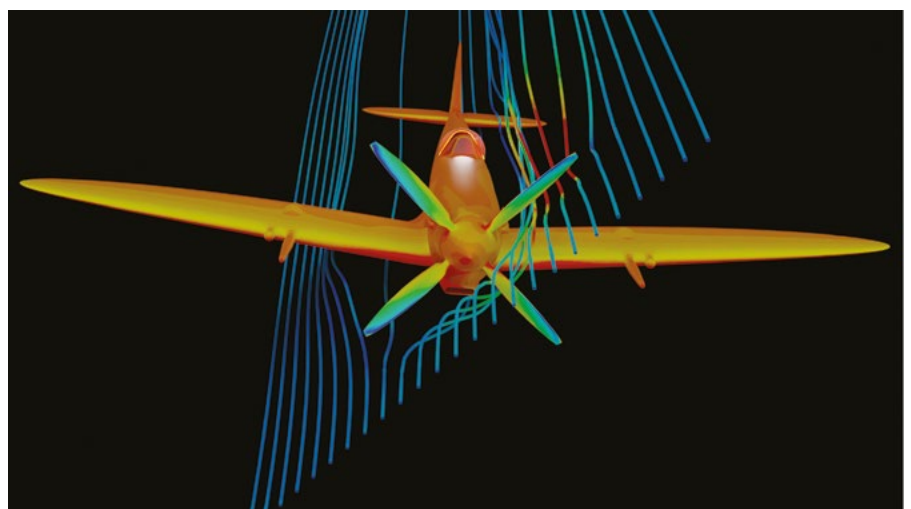
ESPRESO: Vectorization is a standard way to improve performance of SIMD operations, which are the major parts of our FEM assembler. We utilized known libraries for its implementation (OpenMP, libXSMM). To provide a composed system, we interfaced solvers

such as multigrid or parallel direct solvers from the Intel MKL library that can in some cases be more efficient than the currently implemented FETI solver. The vectorization improved single node performance of the ESPRESO library. Together with interface to the new solvers, the library is able to solve a wider range of engineering problems more efficiently and faster.

Visualisation tools: For the creation of the visualisation tools we connected two systems, Blender [3] and COVISE [8]. COVISE stands for COLlaborative VISualisation and SIMulation Environment, and it is available open source. It provided a simulation and post-processing environment that we integrated into Blender. Processing steps in COVISE are represented by modules. These modules, since they are implemented as separate processes, can be arbitrarily spread across different heterogeneous machine platforms. Similar to COVISE modules, Blender has editors such as Composite editor that can process data by feeding them through connected nodes of different functionality. In this way, a final effect or desired property is reached. We fit COVISE's modular hierarchy under the concept of Blender's composite nodes. An example of the resulting concept of nodes in Blender-Covise is depicted in Figure 1.

Thusly, a large number of different simulation formats can be read and processed to reach the final analysis, e.g. visualizing pressure fields, isosurfaces, streamlines, etc. Computationally demanding functions, such as Tracer (post-processing in CFD) and BlenderNode (conversion to proper Blender geome-

Figure 2. Analysis of streamlines and the pressure field around/at the Spitfire. Image rendered in CyclesPhi.



try and materials), have been optimized for parallel processing by OpenMP.

We have also extended the capabilities of the CyclesPhi renderer to increase users' comfort when rendering. An example of a scientific visualisation rendered by CyclesPhi is shown in Figure 2. The renderer has been extended to a remote rendering service on a cluster. A rendering client for Blender has been created. For this, an HPC-as-a-service [9] concept has been modified and used.

Conclusion

Three different sub-projects were solved within this project. They tackled the energy-efficiency of parallel applications in production runs, a library for solving large scale engineering problems, and scientific visualisation tools. Several papers have been published [5, 6, 7, 10] based on the results generated by this project. Besides that, two software applications have also been registered [2, 11].

Since all three topics create major research directions in the INFRA lab, they will also be researched and developed further in the future.

References

- [1] Vysocky, O., Beseda, M., Riha, L., Zapletal, J., Lysaght, M., Kannan, V. MERIC and RADAR generator: Tools for energy evaluation and runtime tuning of HPC applications. *Lect Notes Comput Sci.* 2018, 11087 LNCS:144-59. DOI: 10.1007/978-3-319-97136-0_11.
- [2] Peterek, I., Beseda, M., Vysocky, O. RADAR visualizer. 2019. Available at: <https://code.it4i.cz/vys0053/SGS18-READEX>.
- [3] Blender Foundation. *blender.org - Home of the Blender project - Free and Open 3D Creation Software.* 2021. Available at <https://www.blender.org/>.
- [4] Jaros, M., Riha, L., Karasek, T., Strakos, P., Krpelik, D. Rendering in Blender Cycles using MPI and Intel® Xeon Phi™. *ACM International Conference Proceeding Series.* 2017, Part F130523, art. no. a2.
- [5] Riha, L., Bartolini, A., Vysocky, O. Fine-grained application tuning on OpenPOWER HPC systems. *Proceedings of the Sixth International Conference on Parallel, Distributed, GPU and Cloud Computing for Engineering.* Civil-Comp Press, Stirlingshire, UK, Paper 33. 2019. DOI: 10.4203/ccp.112.33.
- [6] Jaros, M., Vysocky, O., Strakos, P., Spetko, M. Energy consumption evaluation of Blender's image renderer in HPC environment. *Proceedings of the Sixth International Conference on Parallel, Distributed, GPU and Cloud Computing for Engineering.* Civil-Comp Press, Stirlingshire, UK, Paper 32. 2019. DOI: 10.4203/ccp.112.32.
- [7] Spetko, M., Riha, L., Jansik, B. Performance, power consumption and thermal behavioral evaluation of the DGX-2 platform. *Adv Parallel Comput.* 2020. 36:614-23.
- [8] HLRS High Performance Computing Center Stuttgart - COVISE. 2021. Available at <https://www.hlrs.de/covise/>.
- [9] Svaton, V., Martinovic, J., Krenek, J., Esch, T., Tomancak, P. HPC-as-a-service via HEAppE platform. 2020. DOI: 10.1007/978-3-030-22354-0_26.
- [10] Jaros, M., Strakos, P., Riha, L., Maly, L. Interactive rendering with blender cycles for virtual reality using high performance computing clusters. *AIP Conference Proceedings.* 2019, 2116. DOI: 10.1063/1.5114327.
- [11] Jaros, M., Strakos, P., Riha, L. CyclesPhi renderer. 2019. Available at <https://code.it4i.cz/raas/cyclesphi>.

NATURAL COMPUTATION-BASED DESIGN TECHNIQUES FOR CELLULAR AUTOMATA AND APPLICATIONS

Research institution
Brno University of
Technology, Faculty
of Information
Technology

Principal investigator
Michal Bidlo

Project ID
OPEN-14-4

Introduction

Parallelism represents an important concept in performing various processes, mainly natural and computational. It allows accelerating them and achieving behaviour which would not be possible without parallelism. For example, ants, bees and birds form their specific social systems and swarms for obtaining food, building or defending their nests. Living species develop (grow) from a seed by dividing this seed in order to form multiple cells and further by dividing these cells (in parallel) form a complex body. Cellular automata represent a computational model that imitates the behaviour of cells in living organisms. They consist of a large number of cells which interact locally, change their states synchronously in discrete time steps, and give rise to behaviours which can be interpreted as solutions for specific tasks. Similarly, ant algorithms are inspired by real ants, and try to construct solutions for complex problems which are difficult to solve via conventional methods. This project investigated the possibilities for designing complex

cellular automata, the behaviour of which can create a predetermined pattern or computational process.

Methods and Results

The process of designing (programming) the cellular automata represents a non-trivial task because no universal deterministic approach is available that would lead to obtaining the most suitable transition rules; prescription for the time development of cell states. Therefore, evolutionary algorithms (EA, stochastic search methods) were taken into account. In particular, an adapted variant of Evolution Strategy (ES [1]) and a special representation of transition functions for cellular automata called Conditionally Matching Rules (CMR, published in [2]) were applied. The design of cellular automata for specific tasks by means of evolution represents a search process for which hundreds of independent runs of the EA needed to be executed in parallel. The environment provided by the Anselm and Salomon supercomputers were utilised for this purpose. Specifically, the CMR-

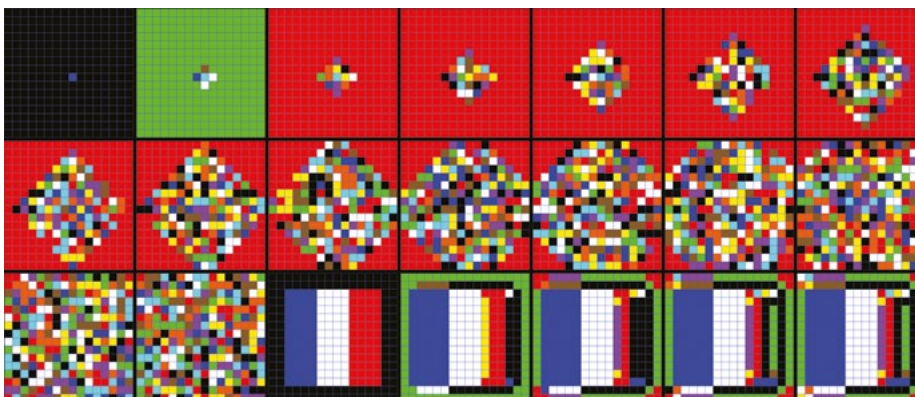


Figure 1. Example of development of a cellular automaton, the rules of which were obtained by means of Evolution Strategy and table-based representation. A pattern development problem for the French Flag was considered from a seed. The sequence of cellular automaton states reads from left to right, top to bottom. The development shows a rather chaotic approach to the pattern construction. The pattern is destroyed by subsequent development of the automaton.

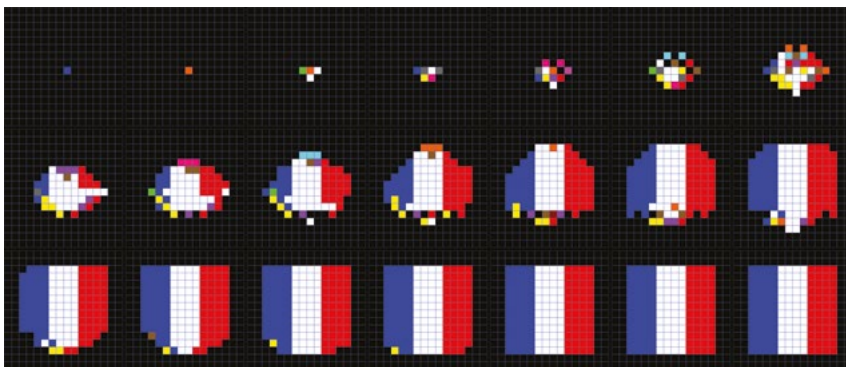


Figure 2. Example of development of a cellular automaton, the rules of which were obtained by means of Evolution Strategy and CMR representation. This approach showed a more systematic construction of the target pattern, 'growing' the French Flag from the seed, in comparison with the table representation and, moreover, the pattern remains stable during subsequent development of the automaton.

based representations of the transition functions for cellular automata were evolved by means of the ES, and the results were compared to those obtained by means of conventional table-based representation. Moreover, transition functions in the form of table-based representations were designed using a variant of the MAX-MIN Ant System [3].

The results proved the importance of utilising a representation for the evolution of transition functions for cellular automata. The proposed ES demonstrated the ability to provide solutions to some 2D pattern development problems in cellular automata using the conventional table representation, but was not able to achieve stability of target patterns. Figure 1 shows one of these results; the pattern is destroyed with further development of the automaton. The utilisation of the CMR representation allowed the observation of a progressive pattern construction in the successful results which eventually becomes stable during subsequent cellular automaton development as illustrated in Figure 2. These results were published in [4, 5] and an extended version in [6].

Another experiment explored the design of table-based transition functions by means of ant algorithms,

the MAX-MIN Ant System in particular. The goal was to verify a novel search method for the design of cellular automata. In this case, the problem of integer square calculations in 1D automata was considered. The results demonstrated its ability to obtain successful solutions for some given input values. However, this method is limited by the possibility of utilisation; it is only valid for the table representation in combination with the ant algorithm, which is not suitable for obtaining generic results. This study was published in [7].

Conclusion

The research dealt with possibilities for designing complex cellular automata and discovered the impact of various representations of transition rules on the behaviour of the resulting automata. In particular, the representation based on Conditionally Matching Rules allowed the achievement of stable states in the cellular automata, which may potentially be useful for advanced applications. Cellular automata as a massively parallel computational model represents a promising platform for future technologies and the knowledge of its design and behaviour is an important issue for their successful development.

References

- [1] Bäck, T., Foussette, C., Krause, P. Contemporary Evolution Strategies. Springer-Verlag Berlin Heidelberg. 2013. DOI: 10.1007/978-3-642-40137-4.
- [2] Dorigo, M., Stützle, T. Ant Colony Optimization. A Bradford Book. 2004. DOI: 10.7551/mitpress/1290.001.0001.
- [3] Bidlo, M. On Routine Evolution of Complex Cellular Automata. IEEE Transactions on Evolutionary Computation. 2016, 20(5), 742–754. DOI: 10.1109/TEVC.2016.2516242.
- [4] Bidlo, M. Evolution of Cellular Automata Development Using Various Representations. GECCO, 19 Proceedings of the Genetic and Evolutionary Computation Conference Companion. Association for Computing Machinery. 2019, 107–108. DOI: 10.1145/3319619.3321881.
- [5] Bidlo, M. Comparison of Evolutionary Development of Cellular Automata Using Various Representations. MENDEL Soft Computing Journal. 2019, 25(1), 95–102. DOI: 10.13164/mendel.2019.1.095.
- [6] Bidlo, M. Advances in the Evolution of Complex Cellular Automata. Computational Intelligence. International Joint Conference, IJCCI 2016 Porto, Portugal, November 9–11, 2016 Revised Selected Papers. Springer International Publishing. 2019, 123–146. DOI: 10.1007/978-3-319-99283-9.
- [7] Bidlo, M., Korgo, J. Ant Colony Optimisation for Performing Computational Task in Cellular Automata. MENDEL Soft Computing Journal. 2019, 25(1), 147–156. DOI: 10.13164/mendel.2019.1.147.

LIFE SCIENCES

IN SILICO DRUG DESIGN

Research institution
Czech Academy of
Sciences, Institute of
Organic Chemistry and
Biochemistry

Principal investigator
Pavel Hobza

Researchers
Jindrich Fanfrlik,
Jan Rezac,
Cemal Kopruluoglu,
Saltuk Eyrilmez,
Martin Lepsik

Project IDs
OPEN-14-17,
OPEN-16-31,
OPEN-18-22

Introduction

We have been developing our own computational framework to be used in computer-aided drug design. It uses corrected semiempirical quantum mechanics (SQM) methods for accurate description of protein-ligand interactions [1,2]. This SQM-based scoring function is by design capable of reliably describing both covalent and noncovalent bonding, including non-classical phenomena such as halogen or dihydrogen bonding and metal ion interactions. The method thus allows us to investigate any type of protein ligand without the need of system-specific parametrization. We aim to reduce the amount of experimental work and expenses by prioritizing compounds for synthesis and biological screening with a higher success. Moreover, the framework provides insight into the drug action at the molecular level. We previously demonstrated that such an approach outperforms classically used scoring functions in both ligand ranking and identifying the ligand native pose in cognate docking [3,4]. In this project, we have shown that the framework outperforms standard scoring functions in distinguishing known binders of the HSP90 target protein among a large database of presumed non-binding “decoy” molecules [5]. We also continue with validating our pipeline retrospectively by using well-curated virtual screening databases, and prospectively by collaborating with experimental groups and using their experimental results.

Methods and Results

In the development part of the project, we tested a new scoring function, based on the semiempirical quantum mechanical (SQM) PM6-D3H4X method combined with the conductor-like screening implicit solvent model (COSMO). The SQM/COSMO and a se-

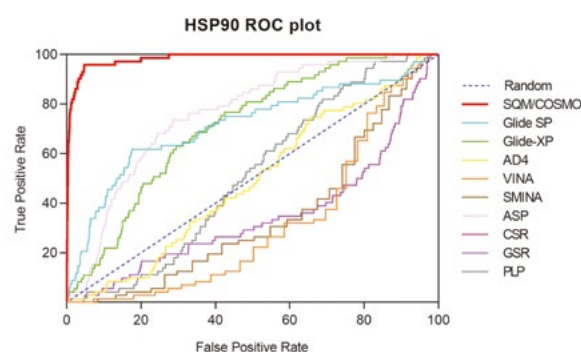


Figure 1. ROC curve plots for comparison of SQM/COSMO (red) versus other several docking functions. Random is shown in dashed dark blue. SQM/COSMO outperforms other popular and frequently used scoring functions by successfully isolating active molecules in the early enrichment stage of the virtual screening calculations.

ries of widely used scoring functions were evaluated in terms of ranking power on the HSP90 protein in the first step. The conventional scoring functions attained the early enrichment factor at 1% (EF1) of less than 10%. The rescoring by the SQM/COSMO scoring function increased EF1 to 48%. We almost reached the best possible receiver operator characteristic (ROC) curve for the HSP90 protein with an area under the curve (AUC) value of 98% (Fig. 1). We have thus demonstrated the applicability of the SQM/COSMO scoring function in a virtual screening pipeline. Such proof-of-concept studies show the power of further developments, e.g. the success rate of the SQM/COSMO scoring function was improved by introducing the enhanced solvation model COSMO2 [6].

In the application part of the project, various protein

ligands were designed using the SQM/COSMO scoring function. For example, norbornyl moiety has been examined as a novel structural motif for cyclin-dependent kinase 2 (CDK2) inhibitors [7]. In another project, critical hot spot interactions of the sub-nanomolar inhibitors of the *Schistosoma mansoni* cathepsin B1 (SmCB1) were identified by the scoring function (Fig. 2) [8]. Finally, we introduced two data sets for validation of approximate computational methods featuring the most common non-covalent interaction types of boron cluster containing inhibitors, the dihydrogen bond, and calculated reference interaction energies at the “golden standard” of quantum chemistry CCSD(T)/CBS level [9].

Conclusion

We have demonstrated the applicability of the SQM/COSMO scoring function in a virtual screening pipeline. Currently, we focus on enabling protein flexibility for extremely flexible drug targets and evaluation of entropy changes upon interactions. We also continue our studies with validating our pipeline retrospectively by using well-curated virtual screening databases and prospectively by collaborating with experimental groups and using their experimental results. The main outcome of this project is a powerful, pure physics-based virtual screening protocol. It aims not only to reduce the cost and estimated duration of drug design applications, but might also be used to generate training data for machine learning algorithms.

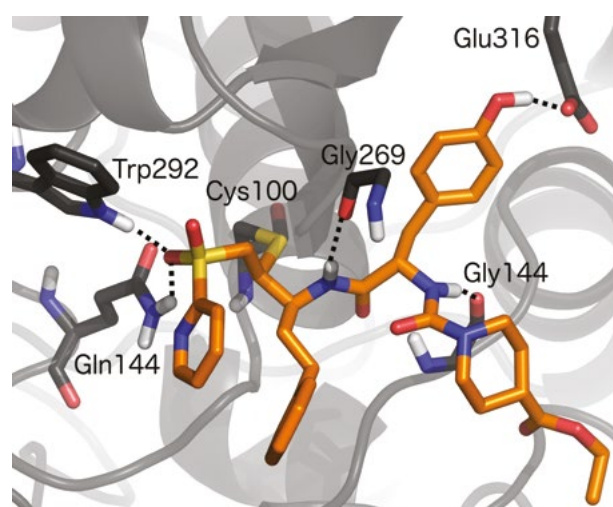


Figure 2. Critical hot spot interactions of the sub-nanomolar inhibitor of the Schistosoma mansoni cathepsin B1 (SmCB1) identified by quantum chemical SQM/COSMO computations.

References

- [1] Lepsik, M., Rezac, J., Pecina, A., Kolar, M., Hobza, P., Fanfrlik, J. The Semiempirical Quantum Mechanical Scoring Function for In Silico Drug Design. *ChemPlusChem*. 2013, 78, 921–931. DOI: 10.1002/cplu.201300199.
- [2] Pecina, A., Eyrilmez, S.M., Kopruluoglu, C., Miriyala, V.; Lepsik, M., Fanfrlik, J., Hobza, P. SQM/COSMO Scoring Function: Reliable Quantum-Mechanical Tool for Sampling and Ranking in Structure-Based Drug Design. *ChemPlusChem*. 2020, 85, 2362–2371. DOI: 10.1002/cplu.202000120.
- [3] Pecina, A., Brynda, J., Vrzal, L., Gnakasekaran, R., Horejsi, M., Eyrilmez, S., Rezac, J., Lepsik, M., Rezacova, P., Hobza, P., Majer, P., Veverka V., Fanfrlik, J. Ranking Power of the SQM/COSMO Scoring Function on Carbonic Anhydrase II-Inhibitor Complexes. *ChemPhysChem*. 2018, 19, 873–879. DOI: 10.1002/cphc.201701104.
- [4] Pecina, A., Meier, R., Fanfrlik, J., Lepsik, M., Rezac, J., Hobza, P., Baldauf, C. The SQM/COSMO filter: reliable native pose identification based on the quantum-mechanical description of protein–ligand interactions and implicit COSMO solvation. *Chemical Communications*. 2016, 52, 3312–3315. DOI: 10.1039/C5CC09499B.
- [5] Eyrilmez, S.M., Kopruluoglu, C., Rezac, J., Hobza, P. *ChemPhysChem*. 2019, 20, 2759–2766.
- [6] Kriz, K., Rezac, J. *J. Chem. Inf. Model*. 2019, 59, 229–235.
- [7] Kopruluoglu, C., Dejmek, M., Sala, M., Ajani, H., Hrebabecky, H., Fanfrlik, J., Jorda, R., Dracinsky, M., Prochazkova, E., Sacha, P., Krystof, V., Hobza, P., Lepsik, M., Nencka, R. *J. Mol. Recognit*. 2020, 33, e2842.
- [8] Jilkova, A., Rubesova, P., Fanfrlik, J., Fajtova, P., Rezacova, P., Brynda, J., Lepsik, M., Mertlikova-Kaiserova, H., Cory D., Renslo, A.R., Roush, W.R., Horn, M., Caffrey, C.R., Mares, M. Druggable Hot Spots in the Schistosomiasis Cathepsin B1 Target Identified by Functional and Binding Mode Analysis of Potent Vinyl Sulfone Inhibitors. *ASC Infect. Dis*. 2021, 7, 1077–1088. DOI: 10.1021/acsinfectdis.0c00501.
- [9] Fanfrlik, J., Pecina, A., Rezac, J., Lepsik, M., Sarosi, M. B., Hnyk, D., Hobza, P. Benchmark Data Sets of Boron Cluster Dihydrogen Bonding for the Validation of Approximate Computational Methods. *ChemPhysChem*. 2020, 21, 2599–2604. DOI: 10.1002/cphc.202000729.

RELIABLE STRUCTURAL ENSEMBLES OF INTRINSICALLY DISORDERED PROTEINS

Research institution
Central European
Institute of
Technology, Masaryk
University

Principal investigator
Jozef Hritz

Researchers
Krishnendu Bera,
Vojtech Zapletal,
Lukas Zidek

Project ID
OPEN-17-7

Introduction

Intrinsically disordered proteins (IDPs) are termed as polypeptide chains that are unable to fold into stable and well-defined tertiary structures. The IDP proteins are often involved in neurodegenerative diseases. The conformational and dynamic changes of IDPs regulated by post-translational modifications such as phosphorylation remain challenging to elucidate. It is also difficult to resolve hybrid systems (IDPs tethered to folded domains) using experimental techniques and computational methods. Experimentally, NMR is the method of choice to study IDPs at an atomic resolution [1], as current available methods are able to provide sufficient resolution to overcome the narrow distribution of chemical shifts [2]. Molecular dynamics (MD) simulation, a computational method, could serve as a possible approach to study behaviour of hybrid proteins (proteins containing intrinsically disordered regions of a length longer than 50-aa) at an atomic level. The NMR parameters can be reliably predicted from ensembles from MD simulation and compared with experimental data. However, the available biomolecular force fields and water models are optimized for folded proteins, and fail to reproduce properties of IDPs.

Methods and Results

All MD simulations were performed using the GROMACS 5.1.4 package [9]. The bond lengths along with hydrogen atoms were constrained using the LINCS algorithm [10]. The 2 fs integration time step was used. The Lennard-Jones interactions and short-range electrostatic interactions cut-off 1.0 nm was applied. The Long-range electrostatic interactions were calculated using particle mesh Ewald (PME) summation with 0.12 nm grid spacing and a fourth

order interpolation. All the simulations are computationally very demanding for two reasons: the need to use explicit water molecules in combination with large simulation boxes due to the disordered nature of IDPs. Another issue is the convergence of generated structural ensembles requiring extensive simulation periods.

The hybrid proteins investigated in this study included 1) the d subunit of RNA polymerase from *Bacillus subtilis* (dRNAP), 2) a regulatory domain of human tyrosine hydroxylase (RD-hTH), and 3) a fragment consisting of residues 159–254 of rat microtubule-associated protein 2c (MAP2c¹⁵⁹⁻²⁵⁴). The performance of force fields (AMBER99SB-ILDN [3], CHARMM22* [4], and CHARMM36m [5]) along with water models (TIP3P [6], TIPS3P [7], or TIP4P-D [8]) have been recommended in the community for IDPs in MD simulations. The obtained MD trajectories were used to predict measurable parameters, such as radii of gyration of the proteins, chemical shifts, residual dipolar couplings, paramagnetic relaxation enhancement, and NMR relaxation data of their individual residues. The predicted quantities were compared with experimental data.

All simulations started with protein conformations having R_g close to the experimental value (SAXS) of 2.5 nm. Regardless of the protein force field used in the initial 100 ns of simulations with TIP3P water models, R_g dropped to ~1.5 nm (Fig. 1B), which confirms that attractive interactions lead to the formation of unnaturally compact structures, as was also reported previously in [11]. Finally, we used the TIP4P-D water model combined with A99, C22*, and C36m for simulations. In agreement with the previous publication [8], the R_g of MAP2c¹⁵⁹⁻²⁵⁴ did not fall below the experimental SAXS data (Fig. 1B e). The TIP4P-D water

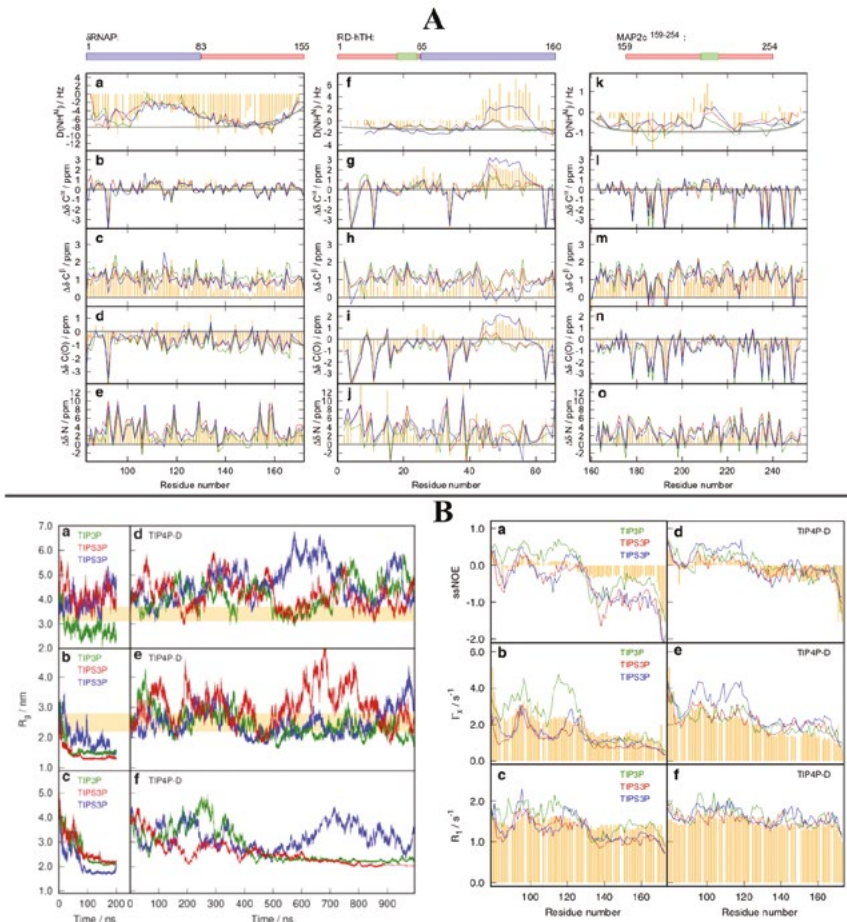


Figure 1. (A) Values of RDC (a, f, and k) and SCS (b–e, g–j, and l–o) in C-terminal IDR (residues 85–173) of dRNAP (a–e), N-terminal IDR (residues 1–65) of RD-hTH (f–j), and MAP2c159–254 (k–o) simulated with the TIP4P-D water model. The random-coil limits are shown in gray. The MD simulations started from structures with α -helices modelled for residues 40–53 of RD-hTH and 200–216 of MAP2c^{159–254}.

(B) R_g of dRNAP (a and d), MAP2c159–254 (b and e), and RD-hTH (c and f) obtained using the TIP3P (TIPS3P) in the case of C22* and C36m) water model (a–c) and TIP4P-D water model (d–f). Experimental data are shown in gold, and values calculated using A99, C22*, and C36m are shown in green, red, and blue, respectively. Figure taken from Zapletal et al. [13]

model acts significantly better than TIP3P or TIPS3P. Table 1 summarizes the comparison between the experimental data and the predicted quantities for all performed computational simulation here. Overall, the most reliable results were obtained from the MD simulations using C36m with the TIP4P-D water model, and this combination most efficiently prevented artificial collapse of disordered regions, an observation in agreement with Robustelli et al. [12]. It also retained transients of α -helices within the disordered regions.

Based on these results, the leading water model (TIP4P-D) and force fields (A99 and C36m) were selected to study the conformational and dynamic changes of the tau fragment (region: 210–240) upon phosphorylation. Microsecond time scale MD simulation studies were performed for apo and phosphorylated residues tau peptide using three different tem-

peratures (278 K, 298 K and 310 K) and two different force field parameters with TIP4P-D water model. We found that the phosphorylation caused an increase in the compactness of the Tau peptide. It also induces a strong structural transition, with Tau favouring a bent conformation. We compared the ability of the force fields to properly produce contacts between residues upon phosphorylation. Upon phosphorylation we noticed several contacts between residues in decreasing temperature for C36m, where A99 failed to make contacts. The strong salt bridges form with nearby lysine and arginine due to the phosphorylation, which may alter the binding of associated proteins like 14-3-3 with Tau. The MD simulation results were verified using NMR experimental parameters like chemical shift and 3J -coupling ($^3J_{H\alpha-H\beta}$). The experimental part was carried out by our collaborator Prof. Isabelle Landrieu.

Conclusion

Considering the rapid development of the force field for proteins, especially for IDPs [13], the prime objective of this study is to present a generally applicable benchmarking approach for IDPs, including NMR relaxation rates [12]. An important feature of the study is to check the experimental parameters from computational simulations and the ability of the force fields to reproduce a broad range of physical properties of the studied IDPs. Based on these results, we tried to solve dynamics and conformational changes of Tau peptide (210–240) upon phosphorylation. The C36m captured the better experimental agreement for the shift in the secondary structure preference, while for

A99 we noticed larger deviation. Upon phosphorylation we noticed from residue pairwise distance maps several contacts between residues in decreasing temperature for C36m. The shifts in R_g were noticed upon decrease in temperature and phosphorylation with the C36m force field. Despite the fact that the listed IDPs were simulated in a microseconds timescale, often the convergence was not obtained. Therefore, enhanced sampling methods is also considered for the future.

The ongoing research requiring these long microsecond simulations of large systems is computationally very demanding, and the vital support from IT4Innovations is highly appreciated.

TABLE 1 Comparison of Calculated RMSD from Experimental Values and Normalized scores

Metric	δ RNAP			RD-hTH			MAP2c ¹⁵⁹⁻²⁵⁴		
	A99	C22*	C36m	A99	C22*	C36m	A99	C22*	C36m
RMSD:									
$\Delta\delta C^\alpha$ /ppm	0.92	0.88	0.82	0.92	0.84	0.64	0.74	0.44	0.55
$\Delta\delta C^\beta$ /ppm	0.86	0.78	0.79	0.63	0.52	0.43	0.45	0.45	0.41
$\Delta\delta C(O)$ /ppm	0.74	0.67	0.62	0.96	0.90	0.56	0.84	0.55	0.65
$\Delta\delta N$ /ppm	1.71	1.92	1.67	3.55	3.40	2.88	1.54	1.90	1.07
Q for $D(NH^N)$	0.30	0.33	0.33	1.21	1.12	0.89	0.76	0.69	0.74
Local PRE ^a by MTSL at L110C	0.25	0.41	0.26	n.d. ^b	n.d.	n.d.	n.d.	n.d.	n.d.
Local PRE by MTSL at L132C	0.07	0.17	0.16	n.d.	n.d.	n.d.	n.d.	n.d.	n.d.
Local PRE by MTSL at L151C	0.12	0.13	0.14	n.d.	n.d.	n.d.	n.d.	n.d.	n.d.
Local PRE by MTSL at L168C	0.06	0.06	0.07	n.d.	n.d.	n.d.	n.d.	n.d.	n.d.
PRE (all data)	0.08	0.10	0.09	n.d.	n.d.	n.d.	n.d.	n.d.	n.d.
ssNOE	0.15	0.17	0.20	0.11	0.38	0.25	0.15	0.20	0.16
R_2 or T_2/s^{-1}	1.50	1.56	2.46	2.62	2.32	0.93	1.13	1.32	1.09
R_1/s^{-1}	0.12	0.15	0.14	0.19	0.24	0.13	0.21	0.19	0.23
Q for SAXS ($0.1 \text{ nm}^{-1} < q < 1 \text{ nm}^{-1}$)	0.057	0.040	0.084	n.d.	n.d.	n.d.	0.070	0.048	0.075
Q for SAXS (all data)	0.060	0.045	0.085	n.d.	n.d.	n.d.	0.084	0.066	0.083
Score:									
s_{CS}	1.11	1.08	1.00	1.46	1.32	1.00	1.42	1.22	1.11
s_{RDC}	1.00	1.09	1.08	1.33	1.20	1.00	1.06	1.00	1.36
s_{PRE} (all data)	1.00	1.25	1.11	n.d.	n.d.	n.d.	n.d.	n.d.	n.d.
s_{relax}	1.00	1.13	1.37	1.74	2.57	1.44	1.04	1.16	1.07
s_{SMR}	1.00	1.13	1.44	1.54	1.89	1.22	1.06	1.12	1.07
s_{SAXS} (all data)	1.32	1.00	1.87	n.d.	n.d.	n.d.	1.28	1.00	1.26
s_{all}	1.08	1.08	1.21	1.55	1.78	1.17	1.24	1.15	1.11
R_g/nm	4.13	4.03	4.66	n.d.	n.d.	n.d.	2.60	2.94	2.78
R_g penalty	0.13	0.10	0.28	n.d.	n.d.	n.d.	0	0.06	0
$s_{combined}$	1.21	1.18	1.49	1.55	1.78	1.17	1.24	1.21	1.11

Figure 2.

^a Calculated for PRE of residues 84–104 because of the indicated spin label.

^b Input experimental data not determined. Table taken from Zapletal et al. [13]

References

- [1] Nowakowski M., et al. Applications of high dimensionality experiments to biomolecular NMR. *Progress in Nuclear Magnetic Resonance Spectroscopy*. 2015, 90–91, 49–73. DOI: 10.1016/j.pnmrs.2015.07.001.
- [2] Novacek, J., et al. Toward optimal-resolution NMR of intrinsically disordered proteins. *Journal of Magnetic Resonance*. 2014, 241, 41–52. DOI: 10.1016/j.jmr.2013.12.008.
- [3] Lindorff-Larsen, K., et al. Improved side-chain torsion potentials for the Amber ff99SB protein force field. *Proteins: Structure, Function, and Bioinformatics*. 2010, 78(8), 1950–1958. DOI 10.1002/prot.22711.
- [4] Piana, S., et al. How Robust Are Protein Folding Simulations with Respect to Force Field Parameterization? *Biophysical Journal*. 2011, 100(9), L47–L49. DOI: 10.1016/j.bpj.2011.03.051.
- [5] Huang, J., et al. CHARMM36m: an improved force field for folded and intrinsically disordered proteins. *Nature Methods*. 2017, 14(1), 71–73. DOI: 10.1038/nmeth.4067.
- [6] Jorgensen, W. L. Quantum and statistical mechanical studies of liquids. 10. Transferable intermolecular potential functions for water, alcohols, and ethers. Application to liquid water. *J. Am. Chem. Soc.* 1981, 103(2), 335–340. DOI: 10.1021/ja00392a016.
- [7] MacKerell, A. D., et al. All-Atom Empirical Potential for Molecular Modeling and Dynamics Studies of Proteins. *J. Phys. Chem. B*. 1998, 102(18), 3586–3616. DOI: 10.1021/jp973084f.
- [8] Piana, S., et al. Water Dispersion Interactions Strongly Influence Simulated Structural Properties of Disordered Protein States. *J. Phys. Chem. B*. 2015, 119(16), 5113–5123. DOI: 10.1021/jp508971m.
- [9] Berendsen, H. J. C., et al. GROMACS: A message-passing parallel molecular dynamics implementation. *Computer Physics Communications*. 1995, 91(1), 43–56. DOI: 10.1016/0010-4655(95)00042-E.
- [10] Hess, B., et al. LINCS: A linear constraint solver for molecular simulations. *Journal of Computational Chemistry*. 1997, 18(12), 1463–1472. DOI: 10.1002/(SICI)1096-987X(199709)18:12<1463::AID-JCC4>3.0.CO;2-H.
- [11] Precechtelova, J. P., et al. Quantum Chemical Calculations of NMR Chemical Shifts in Phosphorylated Intrinsically Disordered Proteins. *J. Chem. Theory Comput.* 2019, 15(10), 5642–5658. DOI: 10.1021/acs.jctc.8b00257.
- [12] Robustelli, P., et al. Developing a molecular dynamics force field for both folded and disordered protein states. *PNAS*. 2018, 115(21), E4758–E4766. DOI: 10.1073/pnas.1800690115.
- [13] Zapletal, V., et al. Choice of Force Field for Proteins Containing Structured and Intrinsically Disordered Regions. *Biophysical Journal*. 2020, 118(7), 1621–1633. DOI: 10.1016/j.bpj.2020.02.019.

PHOTOACOUSTIC TOMOGRAPHY OF THE BREAST EXECUTED ON NVIDIA DGX-2 AND FAT GPU NODES

Research institution
Brno University of
Technology, Faculty
of Information
Technology

Principal investigator
Jiri Jaros

Researchers
Filip Vaverka

Project ID
OPEN-15-39

Introduction

Photoacoustic tomography (PAT) is a biomedical imaging modality based on the photoacoustic effect. In PAT, non-ionizing laser pulses are delivered into biological tissues. Some of the delivered energy will be absorbed and converted into heat, leading to transient thermoelastic expansion and thus wideband ultrasonic emission in the low MHz range. The generated ultrasonic waves are detected by ultrasonic transducers and then analyzed to produce images. Since the optical absorption is closely associated with physiological properties, such as hemoglobin concentration and oxygen saturation, the PAT is used to visualize the vasculature inside tumors with a very high resolution.

The computational process of PAT can be described as follows. At the beginning, there is an initial acoustic pressure distribution in the tissue corresponding to the final image. However, as we cannot directly

see into the tissue, we can only measure the acoustic pressure at the tissue boundary (skin). The goal is thus to solve an inverse problem, answering the question of what the initial pressure distribution should look like to produce the signal we detected at the skin boundary. The iterative process starts with an initial guess which is improved every iteration. After twenty to thirty iterations, the final image is accurate enough, see. Fig. 1.

The core of the iteration process consists of two runs of a relatively large-scale ultrasound model, a forward one simulating the wave coming out from the tissue, and a simulation of the inverse of the wave propagation, producing a new image. In order to achieve sufficient fidelity, a full-wave model taking into account frequency-dependent absorption and non-linearity is required. This model has been implemented using the k-space pseudospectral approach as part of the acoustic k-Wave toolbox [1,2].

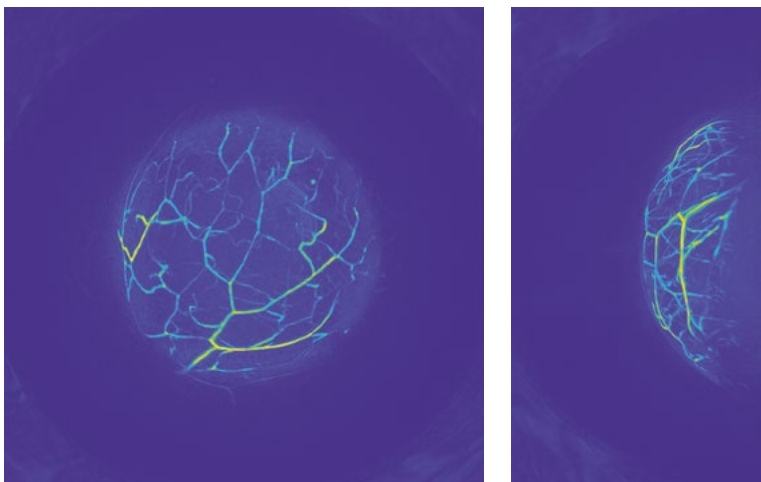


Figure 1. Breast vasculature reconstructed by iterative computational photoacoustic tomography.

Methods and Results

Application of the k-space pseudospectral approach in PAT leads to a system of partial differential equations solved over domains with more than 1024^3 grid points consuming over 100 GB of RAM for tens of thousands of time steps. This task would traditionally be solved on a CPU-based cluster since these codes are typically memory and communication heavy [2]. However, we developed a GPU accelerated simulation code running on a cluster of 512 single-GPU nodes of the Piz Daint supercomputer and investigated how our code can benefit from the use of CUDA peer-to-peer (P2P) communications in multi-GPU compute nodes based on PCI-Express interconnect [3].

In this project, we investigated the benefits of high-bandwidth low-latency NVlink interconnect in an Nvidia DGX-2 super-dense multi-GPU server in comparison to a more traditional PCI-Express 3.0 based multi-GPU server. Nvidia DGX-2 is a dual socket server based on Intel Xeon Platinum 8168 processors with 2×768 GB of main memory, and 16 Nvidia Tesla V100 Volta GPUs, each of which has 5120 CUDA cores and 32 GB of HBM memory. Our second system was a dual socket PNY server equipped with Intel E5-2620v4 CPUs, 2×256 GB of main memory, and 8 Nvidia Tesla P40 Pascal GPUs, each of which has 3840 CUDA cores and 24 GB of GDDR5X memory. The important

distinction between these two systems is the GPU interconnectivity. DGX-2 uses NVlink 2.0, which offers 300 GB/s bi-directional bandwidth between two GPUs and 2.4 TB/s bisection bandwidth (all-to-all). The PCI-E 3.0 based system has GPUs grouped into pairs connected through PCI-Express hubs, each of which is connected to the root hub in one of the CPUs. The sockets are connected together via an Intel QPI providing up to 64 GB/s of bandwidth, while each link in the PCI-Express structure has 16 PCI-Express 3.0 lanes with up to 32 GB/s.

The key component for efficient multi-GPU acceleration of the pseudo-spectral simulation codes is the minimization of the communication between GPUs. In the case of the k-Wave acoustic toolbox, this can be achieved by a restriction of the global Fourier basis resulting in a domain decomposition where the 3D simulation domain is partitioned into blocks, each of which being assigned to a single GPU [4]. Each partition is expanded to overlap with its neighbors by aspecified amount of grid points, and these overlaps are then periodically exchanged during each time step of the simulation. The domain is treated as periodic, thus the neighbor communications form a torus. The size of the overlaps is a primary determining factor to both the accuracy and the performance of the simulation.

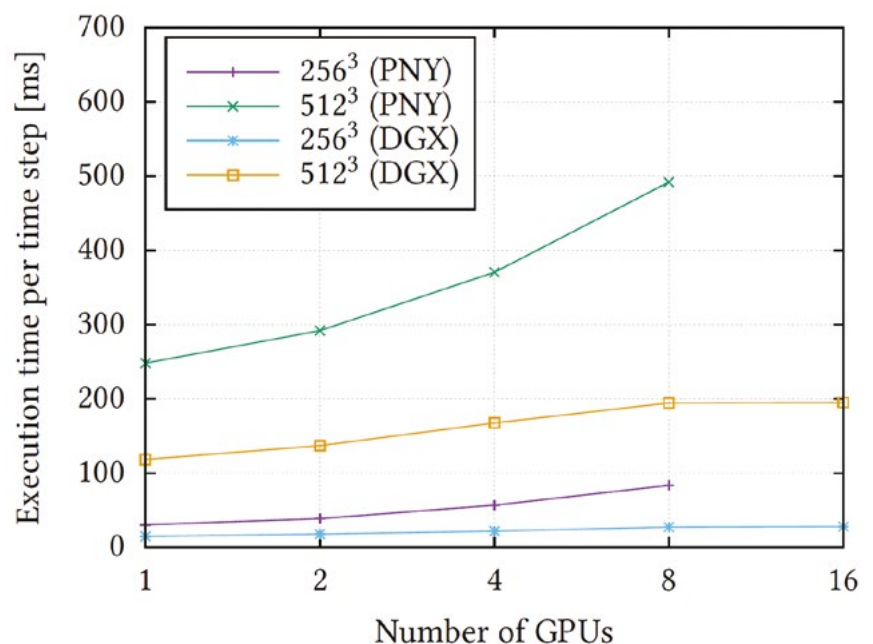


Figure 2. Weak scaling of the local approach using 16 point overlaps.

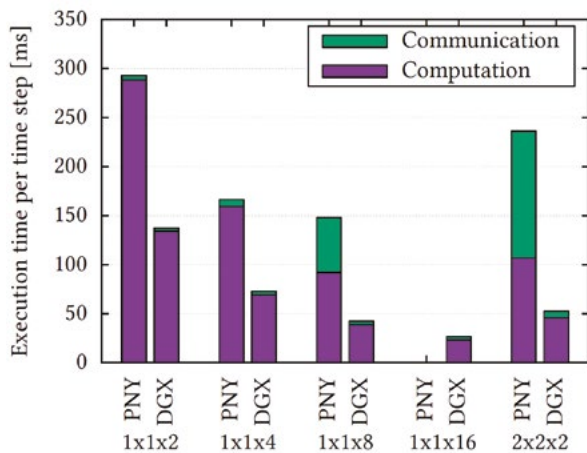


Figure 3. The impact of the communication through the QPI in a $512 \times 512 \times 1024$ grid point simulation with 16 point overlaps in various decompositions on both machines.

The computation of each subdomain is assigned to a single GPU and executed as a mix of CUDA FFT library and custom CUDA kernel calls. The CPU is dedicated to I/O, management, GPU control of CUDA Peer-to-Peer (P2P) routines where possible, with a fallback to CUDA-Aware MPI. The synchronization is always handled on the CPU side by MPI. The particular overlaps are packaged by CUDA kernels and transferred either by the GPU itself (P2P) or the CPU (MPI) to the target. This approach was successful on clusters with a single GPU per node such as Piz Daint1, and achieved almost linear scaling.

A single V100 is about 2.1× faster than a P40 in our workload (mostly due to an increase in the memory bandwidth). However, as a system, the DGX-2 server

achieves a 2–4× speedup over the PNY server while using the same number of GPUs. The additional speedup comes from the NVlink 2.0 interconnect implemented in DGX-2, which is almost 10× faster than the PCI-Express 3.0 $\times 16$ used in the PNY server. Figure 2 shows weak scaling on both machines. Although the scaling is rather poor on both machines due to the increasing rank of the decomposition, it can be seen that this behaviour is more severe on the PNY server, and that the scaling is very good beyond 8 GPUs (where full 3D decomposition is reached). Fig. 3 illustrates the importance of the decomposition and the necessity to avoid unnecessary communication through QPI, while the NVlink 2.0 interconnect in DGX-2 is immune to these issues.

Conclusion

The results obtained for various domain decomposition and subdomain mappings to GPUs show that the direct communication between GPUs in PCI-E based machines may severely suffer if the GPUs are distributed over multiple CPU sockets. The tree structure of the PCI-Express may also become somewhat of an issue as the number of GPUs per node grows. When using only 8 Tesla V100 GPUs, our simulation code achieved a 3× speedup over 8 Tesla P40 GPUs in the PCI-Express based server, showing the importance of fast communication between GPUs. The speedup is then doubled as expected when all 16 GPUs in the DGX-2 are used, and a sufficiently large simulation is considered. Compared to a processor cluster, one DGX-2 system can produce the output image in the same time as 1536 processor cores of the Salomon cluster.

References

- [1] Treeby, B. E., Jaros, J., Rendell, A. P., Cox, B. T. Modeling nonlinear ultrasound propagation in heterogeneous media with power law absorption using a k-space pseudospectral method. *J. Acoust. Soc. Am.* 2012, 131(6), 4324–4336. DOI: 10.1121/1.4712021.
- [2] Jaros, J., Rendell, A. P., Treeby, B. E. Full-wave nonlinear ultrasound simulation on distributed clusters with applications in high-intensity focused ultrasound. *International Journal of High Performance Computing Applications*, SAGE Publications. 2016, 30(2), 137–155. DOI: 10.1177/1094342015581024.
- [3] Vaverka, F., Spetko, M., Treeby, B. E., Jaros, J. Optimization of Ultrasound Simulations on Multi-GPU Servers. *SuperComputing 2018*, Dallas, 2018.
- [4] Jaros, J., Vaverka, F., Treeby, B. E. Spectral Domain Decomposition Using Local Fourier Basis: Application to Ultrasound Simulation on a Cluster of GPUs. *J. Supercomputing Frontiers and Innovations*. 2016, 3(3), 39–54. DOI: 10.14529/jsfi160305.

FIJI BIOIMAGE INFORMATICS ON HPC – PATH TO EXASCALE

Research institution
IT4Innovations
National
Supercomputing
Center

Principal investigator
Michal Krumnikl

Researchers
Pavel Tomancak,
Pavel Moravec,
Jan Kozusznik,
Stefanos Velissariou,
Vladimir Ulman,
Petr Bainar,
Vaclav Svaton

Project IDs
OPEN-15-12,
OPEN-17-47,
OPEN-19-3

Introduction

Bioinformatic data are currently one of the most valuable data types for clinical and biological research. The rapid development of microscopy techniques, such as Light-sheet microscopy, is allowing us to obtain more data of an unprecedented quality than ever before [1]. From this arises the problem of storage, processing, and transfer of such data. There are several commercial and open-source solutions that target the processing of bioinformatic image data, such as Imaris, Cell Profiler [2], KNIME [3] and Fiji [4]. The latter is a distribution of ImageJ [5] (an open-source Java image processing framework inspired by NIH Image) that is especially popular among life scientists.

Fiji targets mainly desktop systems, nevertheless it is starting to find its way to HPC installations due to increasing computational demands. Currently, Fiji supports GPU parallelization through CLIJ plugins [6], and allows the execution of automated HPC workflows [7] for processing embarrassingly parallel jobs based on Snakemake pipelines [8]. However, there are still no genuine internally parallel plugins developed specifically for deployment on large scale parallel machines like HPC clusters or supercomputers. To address this, we have created an OpenMPI interface for Fiji, and model parallel implementations of the most common image processing operations included in ImageJ.

Methods and Results

The exploitation of parallelism in a cluster is not automatic. Programmers need to modify the software to explicitly make use of multiple compute nodes. In modern HPC clusters this is frequently done through the use of message passing interface. OpenMPI [9]

is a freely available implementation of this standard. OpenMPI bindings are usually used in programs written in the C++ programming language or Fortran, which is still popular in HPC as it is used by computational scientists. Since Fiji is a Java-based application it requires a C++ binding to OpenMPI libraries. Fortunately, Java provides a Java Native Interface (JNI) to call native applications or libraries from the code being executed inside a Java virtual machine, and OpenMPI provides an official JNI wrapper, thus making it possible to combine them easily.

To this end, we developed a set of three Fiji plugins. The first, called 'HPC Workflow Manager' is used to simplify the use of HPC clusters by non-experts and provide feedback about the progress of the parallelized workload. The second plugin called 'Parallel Macro' is used to provide functions for parallelism and progress reporting in Fiji macro scripts when they are executed on the cluster. The third plugin delivers a set of Ops (Fiji internal image processing operations) designed for clusters by internally utilizing a message passing mechanism by leveraging the OpenMPI library. Our OpenMPI-based Ops contain implementations for fundamental image processing functions as well as basic maths, logical, and statistical operations.

We demonstrated the performance of the OpenMPI-powered parallelization on synthetic benchmark image data and real biological datasets. In order to mimic the discretization of biological image datasets, we generated a matrix of synthetic images that vary the number of images and the individual image sizes. Figure 1 shows the results of this experiment and illustrates the bridge between OpenMPI and Fiji.

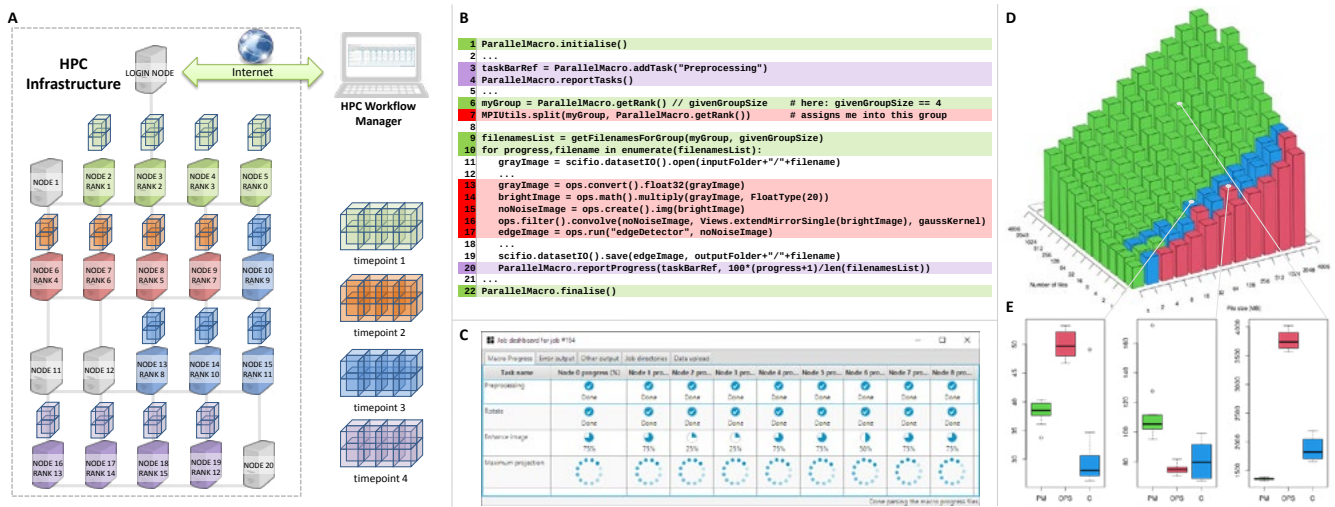
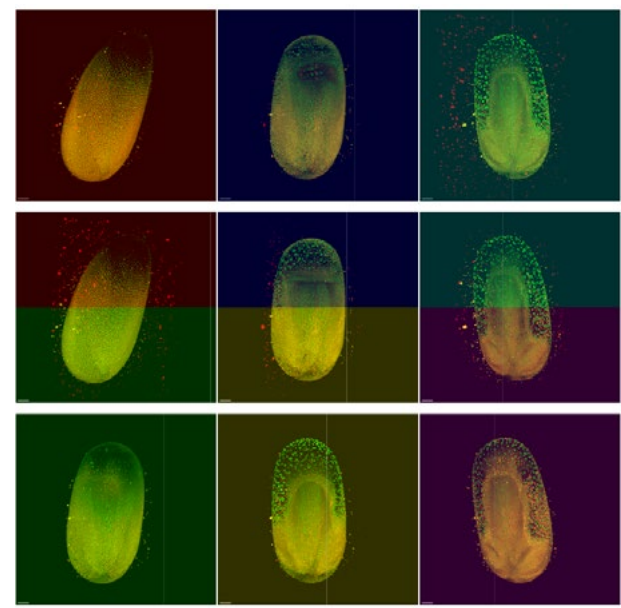


Figure 1. (a) Schematic representation of splitting a large image processing task (timelapse dataset) in a client computer running Fiji and distributing it across an HPC resource. Colors indicate splitting by timepoint while boxes denote within timepoint splitting of the image data into smaller chunks. (b) Abridged source code of an example parallel macro executed as a job on remote HPC. Blue lines show macro code elements used to split the task by timepoints. Red lines highlight Fiji OpenMPI-based Ops elements used to process the chunks. (c) Graphical User Interface element enabling monitoring of the progress of parallel computation within Fiji. (d) Running times of the different parallelization approaches (parallel macro alone, parallel Ops alone and combination of both) evaluated on the benchmark artificial datasets with varying image sizes and image counts. Colour reflects the best winning strategy achieving the lowest time (green parallel macro, red parallel Ops and blue combination of both). Running times are plotted in a logarithmic scale; each box depicts the median value from ten benchmark runs on a cluster with eight nodes. (e) Boxplots for three sample dataset configurations drawn for (d) illustrate different behaviour of strategies based on varying dataset parameters.

To evaluate the merits of deploying OpenMPI-powered Fiji, we also performed the experiments on real biological data on two distinct clusters. By inserting a few simple control statements into a macro for processing of light sheet microscopy data, we achieved the distribution of the processing of time points to individual cluster nodes. Figure 2 depicts a visualisation of a convolution filter applied to a stack of ARGB biological images (part of the Tribolium dataset kindly provided by Akanksha Jain) processed by six nodes. Colorization is an artificially created artifact for debugging purposes caused by adding a constant (derived from the node rank) to one of the color channels. As a result of this, it is clearly visible how the dataset was divided between the nodes.

The experiments were run on Salomon, a supercomputer operated by IT4Innovations National Supercomputing Center at VSB – Technical University of Ostrava and Madmax, a supercomputer of the Max Planck Institute of Molecular Cell Biology and Genetics in Dresden.

Figure 2. A visualisation of a convolution filter applied to a stack of ARGB biological images (part of the Tribolium dataset kindly provided by Akanksha Jain) processed by six nodes.



Conclusion

Thanks to our work, Fiji now supports two kinds of parallelization – GPU acceleration performed by CLIJ plugins and HPC parallelization implemented by the use of our OpenMPI based plugins. The experimental results show that, as long as the user is able to fit the input into the GPU and the computational task is reasonable in its complexity, CLIJ provides currently the

best solution available in Fiji. However, when it comes to large datasets, then CLIJ will reach its limit, and we have to look for more advanced concepts like the newly implemented OpenMPI plugins. To prove this, we have provided several examples of parallelization on a large scale involving convolution and filtering of multidimensional datasets. The source codes of the herein mentioned software are available on GitHub: <https://github.com/fiji-hpc/hpc-workflow-manager-full>.

References

- [1] Olarte, O. E., Andilla, J., Gualda, J. E., Alvarez, P. L. Light-sheet microscopy: a tutorial. *Advances in Optics and Photonics*. 2018, 10(1), 111–179. DOI: 10.1364/AOP.10.000111.
- [2] Carpenter, A. E., Jones, T. R., Lamprecht, M. R., et al. CellProfiler: image analysis software for identifying and quantifying cell phenotypes. *Genome biology*. 2006, 7(10), 1–11. DOI: 10.1186/gb-2006-7-10-r100.
- [3] Berthold, M. R., Cebon, N., Dill, F., Gabriel, T. R., Kötter, T., Meinel, T., Ohl, P., Thiel, K., Wiswedel, B. KNIME—the Konstanz information miner: version 2.0 and beyond. *AcM SIGKDD explorations Newsletter*. 2009, 11(1), 26–31. DOI: 10.1145/1656274.1656280.
- [4] Schindelin, J., Arganda-Carreras, I., Frise, E., Kaynig, V., Longair, M., Pietzsch, T., Preibisch, S., et al. Fiji: an open-source platform for biological-image analysis. *Nature methods*. 2012, 9, 676–682. DOI: 10.1038/nmeth.2019.
- [5] Schneider, C. A., Rasband, W. S., Eliceiri, K. W. NIH Image to ImageJ: 25 years of image analysis. *Nature methods*. 2012, 9(7), 671–675. DOI: 10.1038/nmeth.2089.
- [6] Haase, R., Royer, L. A., Steinbach, P., Schmidt, D., Dibrov, A., Schmidt, U., Weigert, M., et al. CLIJ: GPU-accelerated image processing for everyone. *Nature methods*. 2020, 17(1), 5–6. DOI: 10.1038/s41592-019-0650-1.
- [7] Kozusznik, J., Bainer, P., Klimova, J., Krumnikl, M., Moravec, P., Svaton, V., Tomancak, P. SPIM workflow manager for HPC. *Bioinformatics*. 2019, 35(19), 3875–3876. DOI: 10.1093/bioinformatics/btz140.
- [8] Köster, J., Rahmann, S. Snakemake—a scalable bioinformatics workflow engine. *Bioinformatics*. 2012, 28(19), 2520–2522. DOI: 10.1093/bioinformatics/bts480.
- [9] Message Passing Interface Forum. MPI: A Message–Passing Interface Standard 2019 Draft Specification. MPI Standard. (2019).

INTERACTIONS OF MACROCYCLIC INHIBITORS WITH STING PROTEIN – NOVEL ROUTE TO TREAT CANCER AND CHRONIC HEPATITIS B

Research institution
Czech Academy of
Sciences, Institute of
Organic Chemistry and
Biochemistry

Principal investigator
Lubomir Rulisek

Researchers
Ondrej Gutten,
Zahra Aliakbar
Tehrani

Project ID
OPEN-15-18

Introduction

Computational treatment of ligand:protein interactions is an old yet unsolved challenge in theoretical chemistry. It has been shown by us and others [1,2] that quantum chemical methods are a preferred option in (semi)quantitative description of ligand binding. Sometimes denoted as “QM/MM-scoring”, [2] the hybrid quantum mechanical and molecular mechanical (QM/MM) approach, combined with X-ray crystallography, molecular docking and conformational sampling, seems to be the most promising approach for computational ligand (drug) design. [2] However, the accuracy of the QM/MM approaches comes at the price of the huge computational resources required for the calculations; these resources are available in supercomputer centres.

Specifically, within the OPEN-15-18 IT4Innovations project, we have focused on the stimulator of interferon genes (STING), a protein that is central to the

immune system and whose activation and inhibition represents an underexplored therapeutic target in medicinal chemistry.

The natural ligand of the STING is the cyclic dinucleotide 2',3'-cGAMP (cyclic [G(2',5')pA(3',5')p]), which is synthesized by the cyclic- GMP-AMP synthase, upon detection of double-stranded DNA in the cytosol.[3,4] As an adaptor protein the STING recruits and activates a TANK binding kinase (TBK1) and inhibitory kappa B kinases (IKK). Through transcription factors IRF3 and NFκB, the activation of the pathway results in a secretion of type I interferons and proinflammatory cytokines (such as TNF-α and IP-10) which are essential for the host's defense against invading pathogens and the induction of an antitumoral immunity.

Our computational efforts, carried out at the IT4Innovations National Supercomputing Center, and described in more detail below, aimed at (1) the quantitative evaluation and interpretation of the observed

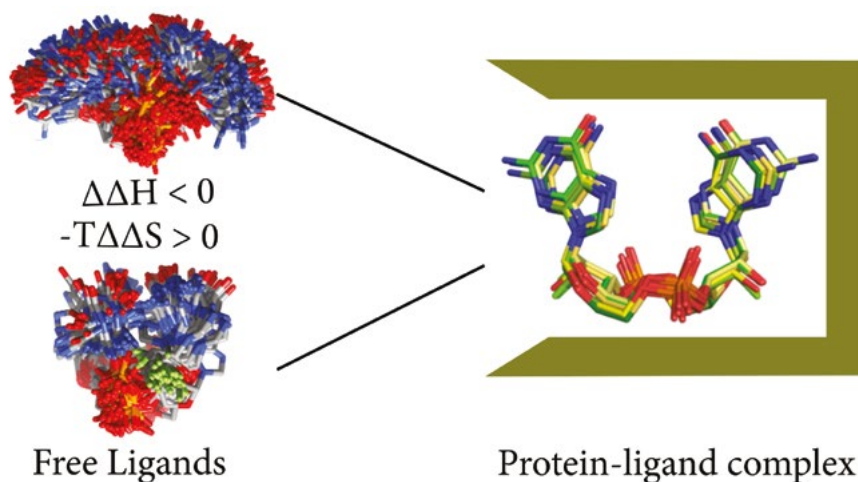


Figure 1. Huge enthalpy/entropy compensation of protein:ligand complexes with identical binding modes can only be explained by complementing the analysis of the complex with conformational analysis of unbound ligands.

STING:CDN binding constants (CDN = cyclic dinucleotide), (2) elucidation of the structural and energetic details accompanying the STING ligand binding and ultimately to (3) predictions of new molecular scaffolds to synthesize and test experimentally.

Methods and Results

Computational Methods: QM/MM calculations. QM/MM calculations were carried out by employing the ComQum software,[5] using the standard (ONI-OM-like) hydrogen-link approach. The quantum system consisted of approximately 600 atoms: ~70 atoms of the ligands, 18 water molecules, and 486 atoms of the STING protein which included all interacting residues in the vicinity of the ligand. The QM system was described by the density functional theory (DFT), typically at the BP86-D3/DZVP-DFT level, while the MM system was described by Amber ff03. The QM/MM calculations (ComQum program) coupled QM code Turbomole with the Amber MM code.

Computational Methods: Ligand Binding. Having the QM/MM equilibrium (optimized) geometries, only a quantum system representing the protein binding site, active site waters, and the ligand (vide supra), was considered and immersed into an implicit solvent. This computational strategy is sometimes denoted as the “cluster model” approach. Interaction (free) energies were calculated as the difference between the free energy of a protein-ligand (+waters) complex and the free energies of the standalone ligand and protein in their fully relaxed geometries (i.e.

global minima):

$$G'_{int} = G'^{protein:ligand}_{complex} - G'^{ligand}_{complex} - G'^{protein}_{complex},$$

where G'^X_Y denotes the free energy value of the system X in the geometry Y, e.g. G'^{ligand}_{ligand} is the free energy of the ligand in its global minimum in a solvent. Since the $G'^{protein}_{protein}$ is a constant for all systems studied, this value is not needed for the relative G'_{int} .

Free energies of a particular system, be it a protein, complex or ligand, were defined as

$$G' = E_{COSMO} + \Delta E + \mu$$

where E_{COSMO} corresponds to the BP86-D3B/COSMO($\epsilon = \infty$) energy of the molecule, ΔE is the averaged COSMO-RS correction for the dielectric energy, and μ is the chemical potential of the conformer (standard DFT/COSMO-RS protocol). Global minima for the ligand were obtained using a combination of the PRIME conformational sampling algorithm as implemented in the Schrodinger 2019-1 suite, and our in-house cross-morphing program that morphs the geometry of a particular CDN into the one of its low-energy cognate in similar CDN, thus guaranteeing that none of the important minima found for any CDN escapes our attention.[6]

Quest for an efficient STING agonist. A series of approximately 300 compounds with the CDN scaffold were prepared enzymatically and synthetically at

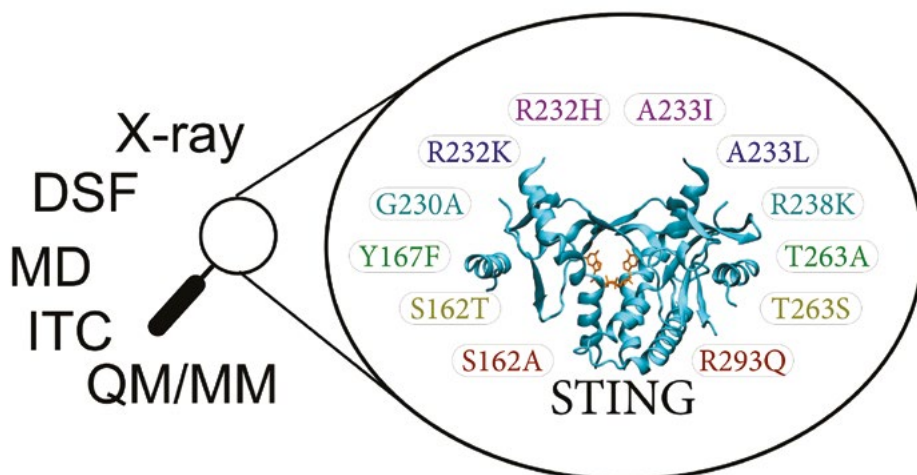


Figure 2. Rationally designed mutations in the STING proteins probing the role of various types of protein:ligand interactions, and evaluated by employing multiple computational and experimental methods.

IOCB, by medicinal chemistry and biology groups. These efforts were complemented by large-scale QM/MM calculations [7,8] that interpreted the experimental findings (both structural and thermodynamic) and motivated the more detailed investigations mentioned below.

Ligand Strain and Its Conformational Complexity Is a Major Factor Determining Binding of Cyclic Dinucleotides to STING Protein. In a joint theoretical and experimental study [9], the thermodynamics of the ligand binding were thoroughly investigated. We correlated structural biology, isothermal calorimetry (ITC) and computational modelling to elucidate factors contributing to binding of six CDNs; three pairs of natural (ribo) and fluorinated (2'-fluororibo) 3,3'-CDN's. X-ray structural analyses of six {STING:CDN} complexes did not offer any explanation for different affinities of the studied ligands. ITC showed huge entropy/enthalpy compensation, up to 25 kcal.mol⁻¹, for this set of apparently similar ligands. The higher affinities of fluorinated analogues were indeed explained with help of computational methods by smaller loss of entropy upon binding and by smaller strain (free) energy (c.f., Figure 1).

Protein-Ligand Interactions in the STING Binding Site Probed by Rationally Designed Single Point Mutations: Experiment and Theory. We aimed to provide complementary information to large-scale "ligand-profiling" studies by probing the importance of STING:CDN protein:ligand interactions on the protein side.[10] We examined in detail six typical CDNs each in a complex with 13 rationally devised mutations in STING. The mutations switch various types of protein:ligand interactions on and off – π - π stacking,

hydrogen bonding, ionic pairing and non-polar contacts. We correlated experimental data obtained by differential scanning fluorimetry, X-ray crystallography, and isothermal titration calorimetry with theoretical calculations. This enabled us to provide a mechanistic interpretation of the differences in the binding of representative CDNs to STING. A very good correlation ($R^2= 0.6$) between the experimental binding affinities and interaction energies computed by quantum chemical methods enabled us to explain the effect of the studied mutations in detail, and evaluate specific interactions quantitatively. This work may inspire the development of high-affinity ligands against the common STING haplotypes by targeting the key (sometimes non-intuitive) protein:ligand interactions.

Conclusion

Massive computational efforts resulted in several joint experimental and theoretical contributions dealing with the STING:ligand interactions. The best systems were synthesized and patented, and currently a small biotechnology company is involved in further development of the designed compounds with the hope objective of exploring their promising therapeutic potential. Throughout the whole STING project, carried out through the joint efforts of half a dozen research groups at IOCB, the theory has rationalized experimental findings, provoked many intriguing questions and represented an integral part of the above IOCB STING project team lead by Dr. Gabriel Birkuš. All this was possible because of the generous time granted by IT4Innovations, which is gratefully acknowledged.

References

- [1] Barinka, C., Novakova, Z., Hin, N., Bim, D., Ferraris, D. V., Duvall, B., Kabarriti, G., Tsukamoto, R., Budesinsky, M., Motlova, L., Rojas, C., Slusher, B. S., Rokob, T. A., Rulisek, L., Tsukamoto, T. Structural and computational basis for potent inhibition of glutamate carboxypeptidase II by carbamate-based inhibitors. *Bioorg. Med. Chem.* 2019, 27(2), 255–264. DOI: 10.1016/j.bmc.2018.11.022.
- [2] Pecina, A., Eyrilmez, S. M., Kopruluoglu, C., Miriyala, V. M., Lepsik, M., Fanfrik, J., Rezac, J., Hobza, P. SQM/COSMO Scoring Function: Reliable Quantum-Mechanical Tool for Sampling and Ranking in Structure-Based Drug Design. *ChemPlusChem.* 2020, 85, 2362–2371. DOI: 10.1002/cplu.202000120.
- [3] Wu, J., Sun, L., Chen, X., Du, F., Shi, H., Chen, C., and Chen, Z. J. Cyclic GMP-AMP Is an Endogenous Second Messenger in Innate Immune Signaling by Cytosolic DNA. *Science.* 2013, 339(6121), 826–830. DOI: 10.1126/science.1229963.
- [4] Sun, L., Wu, J., Du, F., Chen, X., and Chen, Z. J. Cyclic GMP-AMP Synthase Is a Cytosolic DNA Sensor That Activates the Type I Interferon Pathway. *Science.* 2013, 339(6121), 786–791. DOI: 10.1126/science.1232458.
- [5] Ryde, U., Olsson, M. H. M. Structure, Strain, and Reorganization Energy of Blue Copper Models in the Protein. *Int. J. Quantum Chem.* 2001, 81(5), 335–347. DOI: 10.1002/1097-461X(2001)81:5<335::AID-QUA1003>3.0.CO;2-Q.
- [6] Gutten, O., Jurecka, P., Aliakbar Tehrani, Z., Budesinský, M., Rezac, J., Rulisek, L. Conformational energies and equilibria of cyclic dinucleotides in vacuo and in solution: computational chemistry vs. NMR experiments. *Phys. Chem. Chem. Phys.* 2021, 23, 7280–7294. DOI: 10.1039/D0CP05993E.
- [7] Novotna, B., Vanekova, L., Zavrel, M., Budesinsky, M., Dejmek, M., Smola, M., Gutten, O., Tehrani, Z. A., Pimkova Polidarova, M., Brazdova, A., Liboska, R., Stepanek, I., Vavrina, Z., Jandusik, T., Nencka, R., Rulisek, L., Boura, E., Brynda, J., Pav, O., Birkus, G. Enzymatic Preparation of 2'-5', 3'-5' Cyclic Dinucleotides, Their Binding Properties to Stimulator of Interferon Genes Adaptor Protein, and Structure/Activity Correlations. *J. Med. Chem.* 2019, 62, 10676–10690. DOI: 10.1021/acs.jmedchem.9b01062.
- [8] Pimkova Polidarova, M., Brehova, P., Kaiser, M. M., Smola, M., Dracinsky, M., Smith, J., Marek, A., Dejmek, M., Sala, M., Gutten, O., Rulisek, L., Novotna, B., Brazdova, A., Janeba, Z., Nencka, R., Boura, E., Pav, O., Birkus, G. Synthesis and Biological Evaluation of Phosphoester and Phosphorothioate Prodrugs of STING Agonist 3',3'-c-Di(2'F,2'dAMP). *J. Med. Chem.* 2021, 64, 7596–7616. DOI: 10.1021/acs.jmedchem.1c00301.
- [9] Smola, M., Gutten, O., Dejmek, M., Kozisek, M., Evangelidis, T., Aliakbar Tehrani, Z., Novotna, B., Nencka, R., Birkus, G., Rulisek, L., Boura, E. Ligand Strain and Its Conformational Complexity Is a Major Factor in the Binding of Cyclic Dinucleotides to STING Protein. *Angew. Chem. Int.* 2021, 60, 10172–10178. DOI: 10.1002/anie.202016805.
- [10] Vavrina, Z., Gutten, O., Smola, M., Zavrel, M., Aliakbar Tehrani, Z., Charvat, V., Kozisek, M., Boura, E., Birkus, G., Rulisek, L. Protein-Ligand Interactions in the STING Binding Site Probed by Rationally Designed Single-Point Mutations: Experiment and Theory. *Biochemistry.* 2021, 60, 607–620. DOI: 10.1021/acs.biochem.0c00949.

MATERIAL SCIENCES

NOVEL 2D MAGNETIC SEMICONDUCTING MATERIALS; MULTISCALE DESIGN OF NOVEL RARE EARTH FREE PERMANENT MAGNETS

Research institution
IT4Innovations
National
Supercomputing
Center; Polish
Academy of Sciences,
Institute of Nuclear
Physics

Principal investigator
Dominik Legut

Researchers
Przemyslaw
Piekarz

Project ID
OPEN-17-8

Introduction

Magnetite (Fe_3O_4) is a mineral whose strong magnetic properties were already known in ancient Greece. Initially, it was used mainly in compasses, and later in many other devices, such as data recording tools. It is also widely applied to catalytic processes. Even animals benefit from the properties of magnetite in detecting magnetic fields; for example, birds are known to use it in navigation.

Physicists are also very interested in magnetite because at a temperature of around 125 K it shows the Verwey phase transition [1]; historically it was the first phase metal-to-insulator transformation observed. During this extremely complex process, the electrical conductivity changes by as much as two orders of magnitude and a rearrangement of the crystal structure takes place. Verwey proposed a transformation mechanism based on the location of electrons on iron ions, which leads to the appearance of a periodic spatial distribution of Fe^{2+} and Fe^{3+} charges at low temperatures.

In recent years, structural studies and advanced calculations have confirmed the Verwey hypothesis, while revealing a much more complex charge distribution (16 non-equivalent positions of iron atoms) and proving the existence of orbital order. The fundamental components of this charge-orbital ordering are polarons, which take the form of trimers, complexes made of three iron ions, where the inner atom has more electrons than the two outer atoms.

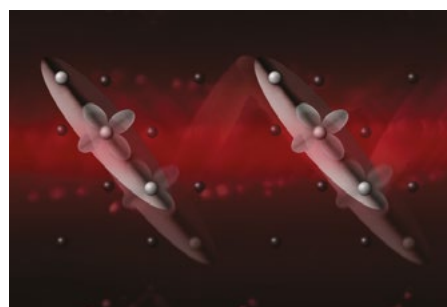


Figure 1. Illustration of the newly discovered charge fluctuations in the trimeron order of magnetite triggered by a laser beam. (Source: Ambra Garlaschelli and MIT).

Methods and Results

The new study, published in the journal *Nature Physics*, was carried out by scientists from many leading research centers around the world. Its purpose was to experimentally uncover the excitations involved in the charge-orbital order of magnetite and describe them by means of advanced theoretical methods. Magnetite samples were synthesized at the AGH University of Science and Technology. The optical conductivity and pump-probe experiments were performed at MIT. The scientists at MIT measured the optical response of magnetite in the extreme infrared for several temperatures. Then, they illuminated the crystal with an ultrashort laser pulse (pump beam) and measured the change in the far-infrared absorption with a de-

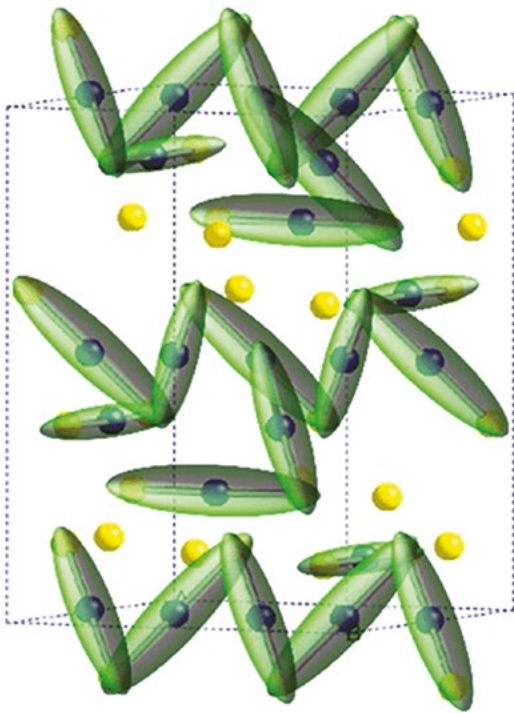


Figure 2. The schematic plot of trimerons in magnetite (from Nature 481, 173 (2012)).

layed probe pulse. The experiments revealed the existence of low-energy excitations of the trimeron order, which correspond to charge oscillations coupled to a lattice deformation. The theoretical analyses were carried out in several places: the Institute of Nuclear Physics of the Polish Academy of Sciences, the Jagiellonian University and the Max Planck Institute,

the University of Rome “La Sapienza”, Northeastern University, the University of Texas at Austin, and the Technical University in Ostrava. Advanced theoretical models allowed the description of the newly-discovered excitations as a coherent tunneling of polarons. The energy barriers for the tunneling process and other model parameters were calculated using density functional theory (DFT). The involvement of these low-energy excitations in the Verwey transition was confirmed using the Ginzburg-Landau model. Finally, the calculations also ruled out other possible explanations for the observed phenomenon, including conventional phonons and orbital excitations.

Conclusion

The obtained results [2] lead to several important conclusions. First, the trimeron order in magnetite has elementary excitations with a very low energy, absorbing radiation in the far-infrared region of the electromagnetic spectrum. Second, these excitations are collective fluctuations of charge and lattice deformations that exhibit critical behaviour and are thus involved in the Verwey transition. Finally, the results shed new light on the cooperative mechanism and dynamical properties that lie at the origin of this complex phase transition. Future plans include studies that will focus on conducting theoretical calculations aimed at forming a better understanding of the observed coupled electronic-structural waves. Mode detail analysis and explanation of the trimerons lattice dynamics behaviour at low temperature were given in Ref. 3.

References

- [1] Verwey, E. J. W. Electronic conduction of magnetite (Fe₃O₄) and its transition point at low temperatures. *Nature*. 1939, 144, 327–328. DOI: 10.1038/144327b0.
- [2] Baldini, E., Belvin, C. A., Rodríguez-Vega, M., Ozel, I. O., Legut, D., Kozłowski, A., Oles, A. M., Parlinski, K., Piekarz, P., Lorenzana, J., Fiete, G. A., Gedik, N. Discovery of the soft electronic modes of the trimeron order in magnetite. *Nature Physics*. 2020, 16, 541–545. DOI: 10.1038/s41567-020-0823-y.
- [3] Piekarz, P., Legut, D., Baldini, E., Belvin, C. A., Kolodziej, T., Tabis, W., Kozłowski, A., Kakol, Z., Tarnawski, Z., Lorenzana, J., Gedik, N., Oles, A. M., Honig, J. M., Parlinski, K. Trimeron-phonon coupling in magnetite. *Phys. Rev.* 2021, B 103, 104303. DOI: 10.1103/PhysRevB.103.104303.

ENERGETICS AND DYNAMICS OF THE INITIAL STEP OF THE BIRCH REDUCTION

Research institution
Czech Academy of
Sciences, Institute of
Organic Chemistry and
Biochemistry; Charles
University, Faculty
of Mathematics and
Physics

Principal investigator
Pavel Jungwirth

Researchers
Krystof Brezina

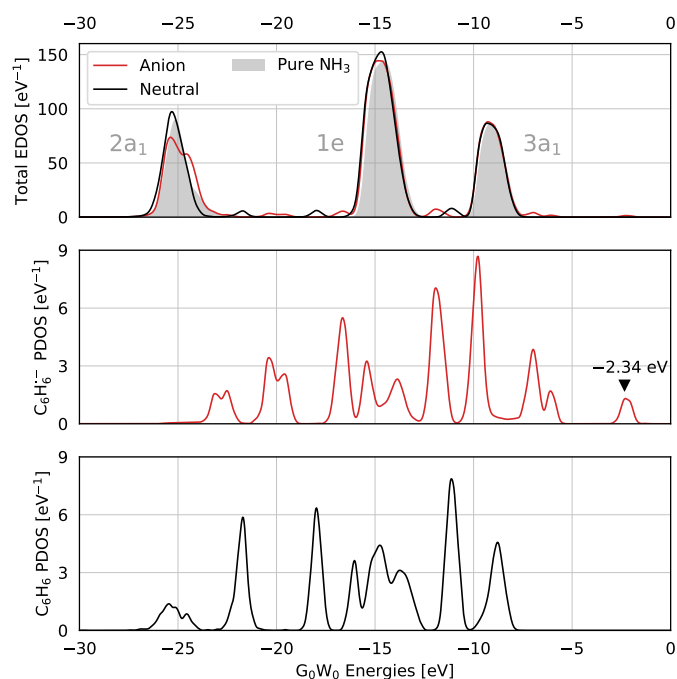
Project ID
OPEN-14-41

Introduction

The benzene radical anion is a molecular ion that appears as an intermediate in several organic reactions, notably including the Birch reduction of benzene by sodium in liquid ammonia [1]. The presence of the solvent seems to be crucial for the stability of the anion. Specifically, the species behaves as a resonance with an extremely short lifetime in gas-phase electron scattering experiments [2] but can be captured in spectroscopic measurements realized in various polar solvents over long periods of time [3-5]. While the conclusions of the gas phase investigations are supported by static ab initio electronic structure calculations [6], the condensed-phase stability re-

mained unexplored until recently. Structurally, the benzene radical anion is no less intriguing in the context of physical chemistry than in the energy domain. Its molecular structure does not adopt the hexagonal symmetry of the parent benzene molecule due to the dynamic Jahn-Teller (JT) effect [7,8]. This is a consequence of the degenerate open-shell electronic structure of the benzene radical anion and gives rise to several new configurational space minima of lower symmetry on the respective potential energy hypersurface between which the system evolves. Our work [9,10] uses state-of-the-art computational methodologies to describe this non-trivial species in liquid ammonia: a solvent in which the species must

Figure 1. Electronic structure of the benzene radical anion. Top panel: the total electronic density of states (EDOS) of benzene radical anion (red) as well as neutral benzene (black) in liquid ammonia. The gray shading represents the EDOS of neat liquid ammonia reported in our previous work [20] and the presented symmetry labels refer to the assigned molecular orbitals of the isolated ammonia molecule. Middle panel: projected density of states (PDOS) of the benzene radical anion. Bottom panel: PDOS of neutral benzene.



be stable due to the feasibility of the Birch reduction. We describe both the molecular [9] and the electronic [10] structure of the studied system to explicitly address the solvent-induced stability as well as to show that these two components are highly correlated through the dynamic JT effect.

Methods and Results

The sampling of thermal structures of the benzene radical anion in a periodic box of 64 ammonia molecules at the experimental density at $-50\text{ }^{\circ}\text{C}$ is realized using ab initio molecular dynamics (AIMD) with the revPBE0-D3 [11-14] hybrid density functional theory (DFT) electronic structure in periodic boundary conditions at a constant temperature [15] of $-50\text{ }^{\circ}\text{C}$. The hybrid functional provides a sufficient level of theory to describe the challenging species in question [9], but brings about very high computational requirements of the AIMD simulations. These were mitigated by employing the highly parallelized implementation of the CP2K 5.1 software [16,17] publicly available as a module on the Salomon high-performance computing (HPC) cluster. Since DFT itself is unable to provide physically meaningful one-electron binding energies, we access these using G_0W_0 calculations [18,19] performed ex post on the AIMD thermal structures. Again, the CP2K software was employed to this end, however this time using a private compilation of the newer version (7.1) on the Salomon cluster.

We begin the discussion of our key findings with the energetics of the electronic structure and its implications for the stability of the solvated benzene radical anion. Our results are shown in Figure 1 in terms of the electronic density of states (EDOS) of the ther-

malized, condensed-phase system. In the top panel of this Figure, we present the total density of states obtained as a statistical distribution of the calculated G_0W_0 energies for both the radical anion (red) and neutral benzene (black, as well as the neat liquid ammonia reported in our previous work [20] (gray shading). Clearly, the EDOS of the simulated systems with solutes is closely related to neat liquid ammonia as the solvent is still the major component in the studied systems.

However, additional low-intensity features arise due to the presence of the solutes. To isolate these features, we use a projection approach [21] where the individual energies are weighted by the square of projection of the corresponding canonical orbital onto a localized atomic basis. This approach yields results qualitatively like the more common subtraction of neat solvent, but circumvents the contribution of solvent molecules electronically changed by the proximity of the solute and, in addition, suppresses numerical noise. In the middle panel, we present this projected density of states (PDOS) for the benzene radical anion. Here, one can notice that the highest occupied state is clearly localized in the negative energy range with its mean at -2.34 eV . This corresponds to the fact that the solvated benzene radical anion represents a bound system, and thus is electronically stable in the liquid ammonia solution. In the bottom panel, we show the same kind of data for the neutral system, which is clearly shifted from the anionic counterpart. This shift is relevant in the interpretation of future experimental photoelectron spectra, where a chemical equilibrium between the radical anion and neutral benzene can be expected.

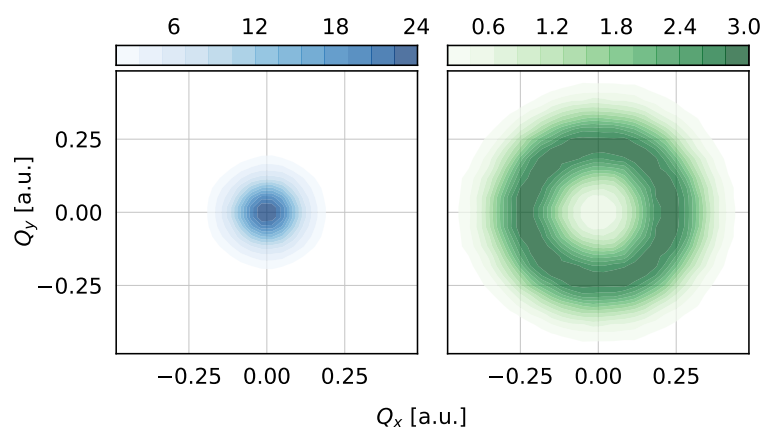


Figure 2. The thermal distribution of molecular geometries in the JT-active-normal-mode subspace. Left panel: neutral benzene which does not exhibit a JT effect. Right panel: benzene radical anion which exhibits a JT effect.

The spatial aspect of both the electronic and molecular structure of the benzene radical anion can be shown to be affected by the dynamic JT effect. In this contribution, we focus on the molecular structure only, but the effect on the electronic structure is equally clear and, moreover, the two domains are shown to correlate in a non-trivial way. The JT effect on molecular geometry can be concisely described in the language of vibrational normal modes, where the relevant potential energy hypersurface takes on the well-known “Mexican hat” shape as the high-symmetry centre is elevated in energy in comparison to its surroundings. Using this description, the JT distortions can be tracked easily in our simulations by identifying the relevant JT-active modes in an optimal solute monomer and projecting the immediate solute distortions encountered in the condensed-phase simulations onto them. Here, we select two orthogonal modes denoted Q_x and Q_y for this purpose. The thermal distributions over the subspace spanned by these two modes are shown in Figure 2 for both the benzene radical anion (green) and neutral benzene (blue). As a closed-shell molecule, neutral benzene does not exhibit any JT behaviour and thus is represented in this subspace by a simple bell-shaped distribution centered around the high-symmetry origin. In contrast, the benzene radical anion clearly shows a very different pattern, in which the high-symmetry

point is significantly depopulated, consistent with the underlying principles of the JT effect, and most of the configurations lie on a circular path around the origin through which the anion evolves. This dynamic pseudorotation causes the structure of the anion not to be fixed, but rather flexible and always changing.

Conclusion

The present work addresses the molecular and the electronic structure of the benzene radical anion in liquid ammonia. We conclusively show that, unlike in the gas phase, the benzene radical anion is a bound and stable system in a liquid ammonia solution, which validates the implicit experimental evidence for its condensed-phase stability. Additionally, our research provides data that can directly corroborate future experimental photoelectron spectroscopy measurements of the systems in question. From the point of view of theory, our results showcase the power of accurate AIMD simulations to model and address even relatively subtle quantum effects such as the JT effect that are experimentally difficult to observe as well as to interpret. This highlights the significance of high-performance computing in the context of quantum electronic structure calculations which will become even more important in the future as more advanced methodologies and bigger systems will become accessible for routine simulations.

References

- [1] Birch, A. J. Reduction by Dissolving Metals. *Nature*. 1946, 158(4017), 585. DOI: 10.1038/158585c0.
- [2] Sanchez, L., Schulz, G. J. Electron Transmission Spectroscopy: Resonances in Triatomic Molecules and Hydrocarbons. *J. Chem. Phys.* 1973, 58(2), 479–493. DOI: 10.1063/1.1679228.
- [3] Moore, J. C., Thornton, C., Collier, W. B., Devlin, J. P. Vibrational Spectra, Jahn-Teller Distortion, and the Structure of the Benzene Radical Anion. *J. Phys. Chem.* 1981, 85(4), 350–354. DOI: 10.1021/j150604a010.
- [4] Shida, T., Iwata, S. Electronic Spectra of Ion Radicals and Their Molecular Orbital Interpretation. III. Aromatic Hydrocarbons. *J. Am. Chem. Soc.* 1973, 95(11), 3473–3483. DOI: 10.1021/ja00792a005.
- [5] Tuttle, T. R., Weissman, S. I. Electron Spin Resonance Spectra of the Anions of Benzene, Toluene and the Xylenes. *J. Am. Chem. Soc.* 1958, 80(20), 5342–5344. DOI: 10.1021/ja01553a005.
- [6] Bazante, A. P., Davidson, E. R., Bartlett, R. J. The Benzene Radical Anion: A Computationally Demanding Prototype for Aromatic Anions. *J. Chem. Phys.* 2015, 142(20), 204304. DOI: 10.1063/1.4921261.
- [7] Bersuker, I. B. The Jahn-Teller Effect. Cambridge University Press. 2006. DOI: 10.1017/CBO9780511524769.
- [8] O'Brien, M. C. M., Chancey, C. C. The Jahn-Teller Effect: An Introduction and Current Review. *Am. J. Phys.* 1993, 61(8), 688–697. DOI: 10.1119/1.17197.
- [9] Brezina, K., Jungwirth, P., Marsalek, O. Benzene Radical Anion in the Context of the Birch Reduction: When Solvation Is the Key. *J. Phys. Chem. Lett.* 2020, 11(15), 6032–6038. DOI: 10.1021/acs.jpcllett.0c01505.
- [10] Brezina, K., Kostal, V., Jungwirth, P., Marsalek, O. Electronic Structure of the Solvated Benzene Radical Anion. arXiv:2105.04543. 2021.
- [11] Perdew, J. P., Burke, K., Ernzerhof, M. Generalized Gradient Approximation Made Simple [*Phys. Rev. Lett.* 77, 3865 (1996)]. *Phys. Rev. Lett.* 1997, 78, 1396–1396. DOI: 10.1103/PhysRevLett.77.3865.
- [12] Zhang, Y., Yang, W. Comment on “Generalized Gradient Approximation Made Simple.” *Phys. Rev. Lett.* 1998, 80, 890–890. DOI: 10.1103/PhysRevLett.80.890.
- [13] Adamo, C., Barone, V. Toward Reliable Density Functional Methods without Adjustable Parameters: The PBE0 Model. *J. Chem. Phys.* 1999, 110, 6158–6170. DOI: 10.1063/1.478522.
- [14] Goerigk, L., Grimme, S. A. Thorough Benchmark of Density Functional Methods for General Main Group Thermochemistry, Kinetics, and Noncovalent Interactions. *Phys. Chem. Chem. Phys.* 2011, 13(14), 6670. DOI: 10.1039/C0CP02984J.
- [15] Bussi, G., Donadio, D., Parrinello, M. Canonical Sampling through Velocity Rescaling. *J. Chem. Phys.* 2007, 126(1), 014101. DOI: 10.1063/1.2408420.
- [16] Hutter, J., Iannuzzi, M., Schiffmann, F., Vandevondele, J. Cp2k: Atomistic Simulations of Condensed Matter Systems. *Wiley Interdiscip. Rev. Comput. Mol. Sci.* 2014, 4(1), 15–25. DOI: 10.1002/wcms.1159.
- [17] Vandevondele, J., Krack, M., Mohamed, F., Parrinello, M., Chassaing, T., Hutter, J. Quickstep: Fast and Accurate Density Functional Calculations Using a Mixed Gaussian and Plane Waves Approach. *Comput. Phys. Commun.* 2005, 167(2), 103–128. DOI: 10.1016/j.cpc.2004.12.014.
- [18] Hüser, F., Olsen, T., Thygesen, K. S. Quasiparticle GW Calculations for Solids, Molecules, and Two-Dimensional Materials. *Phys. Rev. B - Condens. Matter Mater. Phys.* 2013, 87(23), 235132. DOI: 10.1103/PhysRevB.87.235132.
- [19] Wilhelm, J., Del Ben, M., Hutter, J. GW in the Gaussian and Plane Waves Scheme with Application to Linear Acenes. *J. Chem. Theory Comput.* 2016, 12(8), 3623–3635. DOI: 10.1021/acs.jctc.6b00380.
- [20] Buttersack, T., Mason, P. E., McMullen, R. S., Martinek, T., Brezina, K., Hein, D., Ali, H., Kolbeck, C., Schewe, C., Malerz, S., et al. Valence and Core-Level X-Ray Photoelectron Spectroscopy of a Liquid Ammonia Microjet. *J. Am. Chem. Soc.* 2019, 141(5), 1838–1841. DOI: 10.1021/jacs.8b10942.
- [21] Hunt, P., Sprik, M., Vuilleumier, R. Thermal versus Electronic Broadening in the Density of States of Liquid Water. *Chem. Phys. Lett.* 2003, 376(1–2), 68–74. DOI: 10.1016/S0009-2614(03)00954-0.

ACCURACY AND PRECISION FOR EXTENDED SYSTEMS

Research institution
Charles University,
Faculty of
Mathematics and
Physics

Principal investigator
Jiri Klimes

Researchers
Marcin Modrzejewski,
Sirous Yourdkhani,
Pham Ngoc Khanh

Project ID
OPEN-15-15

Introduction

Each day we experience how different materials have different properties, usually even without thinking about it. Water will soak into a towel, but not into plastics; two sheets of paper will not stick together when dry but will do so when wet. The different behaviour that we see is a consequence of the interactions between individual atoms and molecules going on at the nanoscale. Therefore to understand the properties of materials and develop new ones with desirable properties we need to be able to reliably describe the interactions at the nanoscale. This is more easily said than done as the properties of atoms and molecules are governed by quantum mechanics and its Schrödinger's equation. This equation is impossible to solve exactly for all but the simplest systems. Fortunately, a range of approximations of Schrödinger's equation or of the wavefunction exists which allows us to treat larger and more complex systems. Some of these approximations are widely used, but as they are not exact, it is crucial to understand how reliable they are. This testing is especially important when using approximate methods to study interactions between atoms and molecules as the approxi-

mations can deteriorate the accuracy. In this work we picked one system which is a difficult test for the approximate methods; the methane clathrate cluster. This is a single methane molecule in a cage formed by twenty water molecules. It is a model for methane clathrate crystals that can be found at the bottom of the sea and are a large reservoir of methane. We performed a detailed analysis of the accuracy of several more or less approximate methods. Moreover, we were able to obtain a very accurate and precise estimate of the binding energy of methane with the water cage. Finally, the results with all the energies are freely available so that other researchers can rather easily test their methods or fit simpler approaches on the data.

Methods and Results

The property we are interested in is the interaction energy between methane and the water cage, that is the energy difference between methane in the cage and isolated methane and the cage, as illustrated in Figure 1. In this way, the water cage is treated as a single molecule, and such calculation is thus called a supermolecular approach. However, it's not possi-

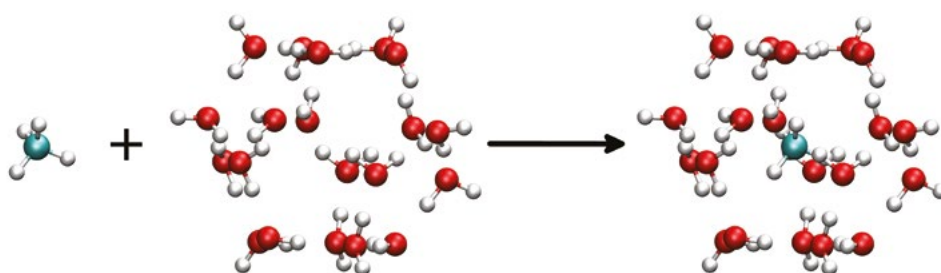
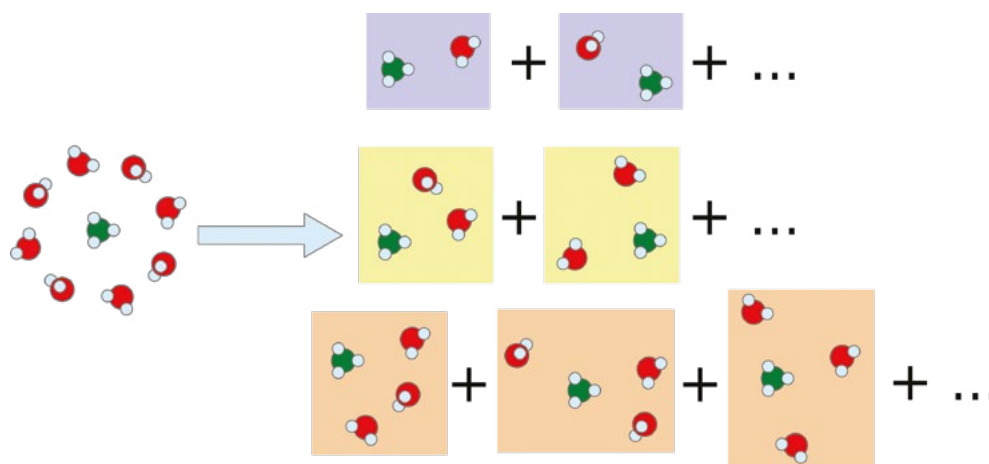


Figure 1. The interaction energy of a methane clathrate cluster is obtained from the energies of isolated methane and water cage and from the whole cluster.

Figure 2. Schematic illustration of many-body expansion of the interaction energy of methane with the water cage.



ble to evaluate the interaction energy using highly accurate methods, such as the coupled clusters CCSD(T) scheme, as the system is too large, at least for our hardware and software. Therefore, we need to use the so-called many-body expansion (MBE) where the total interaction energy is collected from contributions of dimers and correction terms of trimers, tetramers, and so on, as illustrated schematically in Figure 2. The terms are then called 2-, 3-, and 4-body contributions. Even though thousands of calculations are needed to converge the interaction energy using MBE, the individual calculations have a manageable computational cost.

In our work we have primarily focused on a method called random phase approximation to the correlation energy (RPA). This is an approach based on widely used approximate density functional theory (DFT), but includes a seamless description of electron correlations. These are forces that substantially contribute to binding between molecules, but that are difficult to describe. To evaluate the RPA energy we currently use a set of DFT eigenstates. In our work we were interested in how the choice of the DFT approximation affects the accuracy of the interaction energy. Crucially, we had all the reference interaction energies of dimers and corrections of trimers and tetramers at the accurate CCSD(T) level. We were therefore able to analyse not only the total RPA interaction energy but also see all the individual contributions to the total error.

The RPA calculations were performed with an in-house code developed by Dr. Modrzejewski [1]. Apart from RPA, the code is also capable of obtaining stand-

ard DFT and Hartree-Fock energies. The code was optimized for vector instructions (such as AVX-512) and uses coarrays for parallelization over different compute nodes and OpenMP for parallelization on a single node. The reference CCSD(T) calculations were obtained using Molpro [2] on our local hardware due to the lower scalability of these routines.

Using MBE the total interaction energy equals -4.72 kcal/mol for the reference quality CCSD(T) scheme. Analysis of the MBE data in Table 1 shows the somewhat expected results: dominant attractive binding of dimers, repulsive contribution of trimers, and less important higher-order contributions [3], all of which agree with previous work [4]. The total binding energy of PBE0-D4, which is a dispersion corrected hybrid DFT functional, is in a good agreement with the reference value. However, this is mostly due to error compensation between too attractive two- and four-body terms and too repulsive three-body contributions. The RPA based on PBE0 shows the opposite errors, binding too weakly for the dimers and not being repulsive enough for trimers. Overall, the total interaction energy is even worse than that predicted by PBE0-D4. The too weak dimer binding is a known problem and can be reduced by using so-called singles corrections (RSE) [5,6]. The RSE scheme improves the orbitals and reduces the errors inherited from the approximate DFT states. Apart from improving the binding of dimers, the RSE terms also substantially reduce the errors of RPA(PBE0)+RSE for the 3- and 4-body contributions. With RSE, the largest errors occur in the dimers where RPA is not capable to describe some of the complex electron correlations.

Table 1. Two-body interaction energies, three- and four-body non-additive energies, and the total interaction energies of the methane clathrate cluster for the reference CCSD(T) scheme, a dispersion corrected DFT functional PBE0-D4, and RPA obtained on PBE0 states without and with singles corrections; all data are in kcal/mol.

	2-body	3-body	4-body	Total
CCSD(T)	-6.31	1.04	0.56	-4.72
PBE0-D4	-7.34	3.51	-0.14	-3.97
RPA(PBE0)	-4.14	-0.21	1.32	-3.30
RPA (PBE0))+RSE	-5.41	0.74	0.63	-4.03

Conclusion

We obtained a highly reliable interaction energy between a methane molecule and a surrounding water cage. We used the individual contributions to the MBE to analyse the accuracy of simpler methods, primarily of RPA, but also of DFT approximations and of perturbation theory up to the fourth order [3]. The results showed that DFT methods have large errors in the non-additive third- and fourth-order terms which cannot be corrected by simple dispersion corrections. The RPA results are strongly affected by the quality of the input DFT states. In fact, the larger the DFT errors

are, the larger error one can expect from the subsequent RPA calculation.

Based on the good results of RPA for larger clusters we used a correction scheme which combines CCSD(T) for compact clusters with RPA for large ones. This shows a promising performance for clathrate and substantially reduces the computational cost [3]. We performed the MBE analysis also for molecular crystals of small hydrocarbons. The data give us a detailed understanding of the problems occurring in various approximate methods. Moreover, we are testing how these problems can be reduced either by the use of the correction scheme or by other means.

References

- [1] Modrzejewski, M., Yourdkhani, S., Klimes, J. Random-Phase Approximation Applied to Many-Body Noncovalent Systems. *Journal of Chemical Theory and Computation*. 2020, 16, 427-442. DOI: 10.1021/acs.jctc.9b00979.
- [2] Werner, H. J., Knowles, P. J., Knizia, G., Manby, F. R., Schütz, M. Molpro: a general-purpose quantum chemistry program package. *WIREs Computational Molecular Science*. 2012, 2, 242-253. DOI: 10.1002/wcms.82.
- [3] Modrzejewski, M., Yourdkhani, S., Smiga, S., Klimes, J. Random-Phase Approximation in Many-Body Noncovalent Systems: Methane in a Dodecahedral Water Cage. *Journal of Chemical Theory and Computation*. 2021, 17, 804-817. DOI: 10.1021/acs.jctc.0c00966.
- [4] Deible, M. J., Tuguldur, O., Jordan, K. D. Theoretical Study of the Binding Energy of a Methane Molecule in a (H₂O)₂₀ Dodecahedral Cage. *Journal of Physical Chemistry B*. 2014, 118, 8257-8263. DOI: 10.1021/jp501592h.
- [5] Ren, X., Rinke, P., Scuseria, G. E., Scheffler, M. Renormalized second-order perturbation theory for the electron correlation energy: Concept, implementation, and benchmarks. *Physical Review B*. 2013, 88, 035120. DOI: 10.1103/PhysRevB.88.035120.
- [6] Klimes, J., Kaltak, M., Maggio, E., Kresse, G. Singles energy contributions in solids. *Journal of Chemical Physics*. 2015, 143, 102816. DOI: 10.1063/1.4929346.

LARGE-SCALE BENCHMARKING OF NON-COVALENT INTERACTIONS – LONDON DISPERSION AND SIGMA-HOLE BONDS

Research institution
Czech Academy of
Sciences, Institute of
Organic Chemistry and
Biochemistry

Principal investigator
Jan Rezac

Researchers
Kristian Kriz

Project ID
OPEN-19-15

Introduction

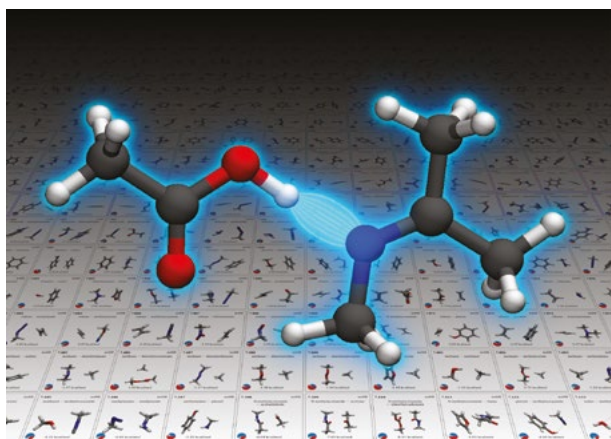
To apply computational chemistry to real-world chemical problems, it is often necessary to work with large systems with thousands of atoms. This is especially true in the two currently most prominent research directions, in the applications of computational methods to biochemistry and to (nano)materials. This requires the use of approximate methods, the development of which relies on accurate reference data that can be used for their parametrization and validation.

We are developing benchmark data sets covering intermolecular interactions, using the most accurate computational methods available to compute refer-

ence interaction energies. These data sets are more than an order of magnitude larger than their predecessors, more diverse, and more accurate.

Methods and Results

To establish a true benchmark, we compute the interaction energies using the coupled-clusters with singles, doubles and perturbative triples; the CCSD(T) method which is considered to be the 'gold standard' of computational chemistry. Moreover, we extrapolate the results from very large basis sets, aiming for the highest accuracy possible. Such calculations are computationally very demanding, what is also the reason for the limited size and accuracy of the previous data sets. We combine our expertise in both building and using benchmark data sets with HPC resources to overcome these limitations. So far, we have published four data sets covering hydrogen bonds [1,2] and repulsive contacts [3] in broad chemical space that feature 1514 non-covalent complexes in more than 11 thousands geometries. Now we are working on an even larger data set of complexes driven by London dispersion, and on a dataset of sigma-hole interactions that will add about 6000 more data points.



Conclusion

This unique collection of data sets is published openly at our website (www.nciatlas.org), and it can be expected that it will serve the scientific community as a useful tool for the development of new computational methods and for the validation of the accuracy

of existing ones. We are now finishing the coverage of the remaining important classes of non-covalent interactions, and once the database is complete, we will apply it ourselves to the development of novel semiempirical quantum-mechanical computational methods applicable to the study of biomolecules.

References

- [1] Rezac, J. Non-Covalent Interactions Atlas Benchmark Data Sets: Hydrogen Bonding. *J. Chem. Theory Comput.* 2020, 16(4), 2355–2368. DOI: 10.1021/acs.jctc.9b01265.
- [2] Rezac, J. Non-Covalent Interactions Atlas Benchmark Data Sets 2: Hydrogen Bonding in an Extended Chemical Space. *J. Chem. Theory Comput.* 2020, 16(10), 6305–6316. DOI: 10.1021/acs.jctc.0c00715.
- [3] Kriz, K., Novacek, M., Rezac, J. Non-Covalent Interactions Atlas Benchmark Data Sets 3: Repulsive Contacts. *J. Chem. Theory Comput.* 2021, 17(3), 1548–1561. DOI: 10.1021/acs.jctc.0c01341.

STRUCTURE AND PROPERTIES OF NOVEL NANOCOMPOSITES FORMED BY INTERMETALLIC COMPOUNDS

Research institution
Masaryk University;
Czech Academy of
Sciences, Institute of
Physics of Materials;
CEITEC – Central
European Institute
of Technology;
Brno University of
Technology

Principal investigator
Mojmir Sob

Researchers
Martin Friak, Petr Sestak,
Petr Rehak, Miroslav Cerny,
Monika Vsianska, Jana Pavlu,
Ivana Mihalikova,
Anton Slavik,
Martina Mazalova,
Vojtech Kopecky,
Nikola Koutna, David Nezval,
Eliska Kohoutkova

Project ID
OPEN-16-2

Introduction

This computational research aims to investigate the structure and properties of promising novel nanocomposites formed by intermetallic compounds, such as various and selected Ti-, Fe-, Ni- and Al-based compounds, which may elucidate potential technological foundations for a variety of engineering innovations and transition-metal nitrides. The central topic of our work is a detailed investigation of interfaces in these intermetallic nanocomposites which are decisive for their technologically important properties. We consider both the “clean” interfaces as well as the effect of segregated impurities and vacancies, which has been studied very little or not at all. The prime objectives of this project are to deliver a deeper understanding of structural and mechanical properties of intermetallic nanocomposites (such as strength, elastic moduli and stability), provide a solid theoretical basis for interpretation of corresponding experimental data, contribute to the design of new advanced materials and, in this way, foster a system of innovation comprising basic and engineering research.

Methods and Results

During the last two decades, theoretical calculations regarding atomic configuration and properties of advanced materials became possible using ab initio electronic structure calculations, i.e. fundamental quantum theory (the Schrödinger equation). To ob-

tain the relevant physical characteristics described above as well as technologically important properties, such as strength, elastic moduli, and fracture toughness, we use the state-of-the-art first-principles electronic structure methods implemented in the program VASP; Vienna Ab initio Simulation Package code (<http://www.vasp.at/>). It is very well parallelized and allows the running of one particular simulation on multiple threads/nodes. VASP is also very well optimized and tested for its usage in high-performance computing (HPC), and can be compiled for each HPC individually using the Fortran Compiler (Intel, PGI or other), MPI libraries (Open MPI, LAM or others), or the Linear Algebra Package libs (LAPACK and BLAS lib). The VASP code runs on an Intel x86 CPU (32bit or 64bit) platform. A part of this code is optimized for running on GPUs.

Our scientific activity was distributed into several scientific subjects. They are listed below, together with the most important results achieved.

(i) Surface-induced magnetism in intermetallics

We investigated the magnetic properties of four low-index surfaces in the bulk nonmagnetic Ni_3Ge intermetallic compound with an $L1_2$ structure [1]. We predict that the (1 1 1) surface of Ni_3Ge is magnetically ordered, with all magnetic moments located at the Ni sites. Magnetic order is also found at the Ni-terminated (0 0 1), (1 1 0), and (2 1 0) surfaces, however, the nonmagnetic NiGe-terminated surfaces are more stable, similarly as in other $L1_2$ compounds. Apparent-

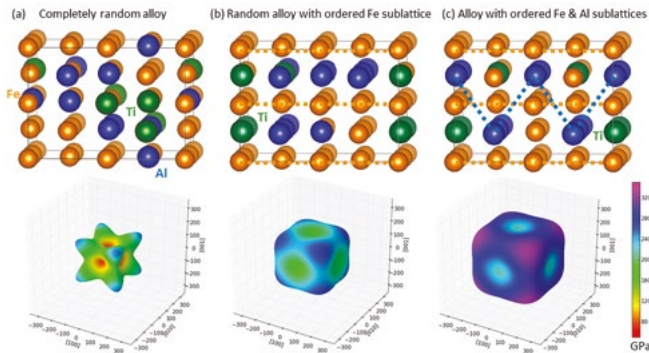


Figure 1. (Upper row) Schematic visualisation of the employed 32-atom computational supercells with the chemical composition $\text{Fe}_{62.5}\text{Al}_{25}\text{Ti}_{12.5}$ used for modelling a cuboid phase in Fe-Al-Ti superalloys. The supercells differ in the distribution of atoms. Yellow and blue dashed lines indicate ordered sublattices as in a stoichiometric Heusler structure. (Lower row) Visualisation of the anisotropic elastic properties for each atomic distribution in the form of directional dependences of the Young's modulus; a very significant dependence on the distribution of atoms is found; see Ref. [6].

ly, the magnetic order in bulk Ni_3Ge is destroyed completely by the hybridization of Ge-p and Ni-d states, and it is recovered at some surfaces due to the reduced coordinate number of Ni atoms.

(ii) Structural, elastic, thermodynamic and electronic properties of Al_3Ti and Al_3V compounds

We studied structural, mechanical, thermodynamic and electronic properties of the intermetallic compounds Al_3Ti and Al_3V in the L_{12} structure in the pressure range of 0–100 GPa [2]. The compound Al_3V in the L_{12} structure possesses interesting properties, including ductility in low pressure regions (up to 20 GPa) but weakly brittle behaviour at high pressures (above 30 GPa), and the minimum value of the Poisson ratio is negative under high pressure.

(iii) Structure and properties of nitride nanocomposites

In collaboration with scientists from the Institute of Materials Science and Technology, Technische Universität Wien, and the Department of Materials Science, Montanuniversität Leoben, we investigated the properties of various nitride structures. The first study [3] concerned the correlation of structural and mechanical properties of AlN/TiN superlattice films. Combining first-principles and experimental techniques, we established Young's modulus dependence of AlN/TiN superlattices on the film-forming phases, and their thicknesses and crystallographic orientations. The disparate character of cleavage properties within different layers of the superlattice (providing indications regarding crack initiation processes) is linked to the changes in bond lengths. Such changes present a direct consequence of the predicted inter-

planar spacing oscillations which are experimentally confirmed by high resolution transmission electron microscopy analyses.

The second study [4] was devoted to point-defect engineering of MoN/TaN superlattice films and included both first-principles and experimental approaches. Superlattice (nanocomposite) architecture represents an effective strategy to improve performance of hard protective coatings. We revealed and interpreted peculiar structure-stability-elasticity relations for MoN/TaN , combining modelling and experimental approaches. The vibrational spectra analysis together with the close overlap between the experimental indentation modulus and the calculated Young's modulus points towards $\text{MoN}_{0.5}/\text{TaN}$ as the most likely chemistry of our coatings.

(iv) Structure and properties of Fe-Al-based systems

We performed an ab initio study of vacancies in disordered magnetic Fe-rich Fe-Al phases [5]. The vacancy formation energies as well as the volumes of (fully relaxed) supercells with vacancies showed a large scatter for the disordered systems. The vacancy formation energies decrease with increasing concentration of Al atoms in the first coordination shell around the vacancy (an anti-correlation) for all disordered cases studied. Lastly, we analysed interactions between the vacancies and the Fe atoms and evaluated vacancy-induced changes in local magnetic moments of Fe atoms.

Further, we investigated the impact of atomic order and anti-phase boundaries on elasticity of phases in Fe-Al-Ti superalloys [6]. Quantum-mechanical calculations were employed to obtain an insight into the

elastic properties of the phases found (see Fig. 1). Three distributions of chemical species were simulated for the phase of cuboids (A2, B2 and $L2_1$) in order to determine a sublattice preference of the excess Fe atoms. The lowest formation energy was obtained when the excess Fe atoms formed a solid solution with the Ti atoms at the Ti-sublattice within the Heusler $L2_1$ phase ($L2_1$ variant). Finally, a nano-scale dynamical mechanical analysis (nanoDMA) was used to probe the elasticity of phases.

Further results on the Fe-Al system (see Fig. 2) were published in papers [7, 8, and 9].

(v) Ti-Al and Ti-Al-Mo system

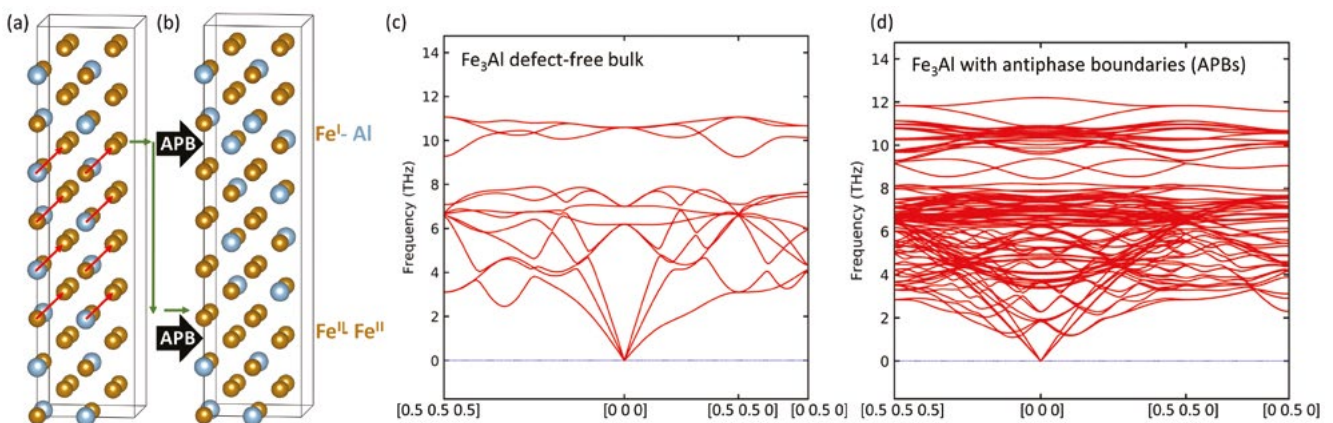
In collaboration with scientists from the Department of Materials Science, Montanuniversität Leoben, we studied selected properties of a Ti-Al-based system [10]. Namely, to shed a new light on the complex microstructural evolution in the Ti-Al-Mo system, we employed ab initio calculations to study bcc-fcc structural transformations of ordered β_0 -TiAl(+Mo) and disordered β -TiAl(+Mo) to ordered γ -TiAl(+Mo) and hypothetically assumed disordered γ_{dis} -TiAl(+Mo) alloys, respectively. In particular, tetragonal (Bain's path) and trigonal transformations were combined with the concept of special quasirandom structures

(SQS). Our calculations of the ordered phases show that the $\beta_0 \rightarrow \gamma$ tetragonal transformation of TiAl is barrierless, i.e., proceeds spontaneously, reflecting the genuine structural instability of the β_0 phase. Upon alloying of ≈ 7.4 at.%Mo, a small barrier between β_0 and γ -related local energy minima is formed. Yet a higher Mo content of ≈ 9 at.% leads to an opposite-direction barrierless transformation $\gamma \rightarrow \beta_0$, i.e., fully stabilizing the β_0 phase.

(vi) Development of software tools

We developed a new web-based tool called MELASA (Multi-phase ELASTic Aggregates), available open-access at <https://melasa.cerit-sc.cz>, for computations and visualisations of anisotropic elastic properties of lamellar (nano-)composites [11]. MELASA implements a linear-elasticity method by Grimsditch and Nizzoli (1986), originally developed for superlattices of any symmetry. Our tool may be used for computation of anisotropic elastic properties of a specific type of periodically separated lamellar (nano-)composites using matrices of elastic stiffnesses of co-existing phases as an input. Elastic properties are visualized in the form of directional dependencies of selected elastic characteristics (Young's modulus and linear compressibility).

Figure 2. Antiphase boundaries (APBs) were studied in Fe_3Al (a), in particular the APBs that are characterized by a shift of a part of the crystal along the $\langle 111 \rangle$ crystallographic direction (see red vectors in part (b)). The phonon spectra of both defect-free bulk Fe_3Al (c) and those of APB-containing crystal (d) were compared, and a very significant impact of APBs was found; see Ref. [9].



Conclusion

The present project provided us with a more detailed and realistic insight into the behaviour of nanocomposites formed by intermetallic compounds and contributed to their potential industrial applications. It elucidated a fundamental understanding of their structural and mechanical properties and suggested new possibilities in designing advanced materials. Such approaches have the potential to save economic resources as they reveal the relations between physical phenomena and material properties, which are usually only experimentally accessible at a very high economic cost, if at all.

The realization of our research enabled us to predict theoretically new phenomena, stimulate further experimental investigations, and provide the theoretical basis for their future technological and industrial use. Last but not least, it gave an opportunity to three PhD students and four undergraduate students to participate in contemporary scientific activities.

We gratefully acknowledge the financial support from the Ministry of Education, Youth and Sports of the Czech Republic under the Project CEITEC 2020 (Project No. LQ1601), the Czech Science Foundation (Project No. 20-08130S) and the Academy of Sciences of the Czech Republic (Institutional Project No. RVO:68081723). Computational resources were provided by the Ministry of Education, Youth and Sports of the Czech Republic under the Projects e-INFRA CZ (ID:90140) at the IT4Innovations National Supercomputing Center and e-Infrastruktura CZ (e-INFRA LM2018140) at the MetaCentrum as well as CERIT Scientific Cloud, both provided within the program Projects of Large Research, Development and Innovations Infrastructures.

References

- [1] Meng, F.-S., Vsianska, M., Friak, M., Sob, M. Surface-induced magnetism in intermetallics: Ni₃Ge compound as a case study. *J. Magn. Magn. Mat.* 2019, 474, 273–281. DOI: 10.1016/j.jmmm.2018.11.055.
- [2] Meng, F.S., Yao, Z., Vsianska, M., Friak, M., Sob, M. Theoretical investigations on structural, elastic, thermodynamic and electronic properties of Al₃Ti and Al₃V compounds in L1₂ structure under high pressure. *Mater. Res. Express* 6. 2019, 056536 (19 pp). DOI: 10.1088/2053-1591/aafec0.
- [3] Koutna, N., Rehak, P., Chen, Z., Bartosik, M., Fallmann, M., Cerny, M., Zhang, Z., Friak, M., Sob, M., Mayrhofer, P. H., Holec, D. Correlating structural and mechanical properties of AlN/TiN superlattice films. *Scripta Mat.* 2019, 165, 159–163. DOI: 10.1016/j.scriptamat.2019.02.021.
- [4] Koutna, N., Hahn, R., Zalesak, J., Friak, M., Bartosik, M., Keckes, J., Sob, M., Mayrhofer, P. H., Holec, D. Point-defect engineering of MoN/TaN superlattice films: A first-principles and experimental study. *Materials and Design*. 2020, 186, 108211. DOI: 10.1016/j.matdes.2019.108211.
- [5] Mihalikova, I., Friak, M., Koutna, N., Holec, D., Sob, M. An Ab Initio Study of Vacancies in Disordered Magnetic Systems: A Case Study of Fe-Rich Fe-Al Phases. *Materials* 12. 2019, 1430. DOI: 10.3390/ma12091430.
- [6] Friak, M., Bursikova, V., Pizurova, N., Pavlu, J., Jiraskova, Y., Homola, V., Mihalikova, I., Slavik, A., Holec, D., Vsianska, M., Koutna, N., Fikar, J., Janickovic, D., Sob, M., Neugebauer, J. Elasticity of Phases in Fe-Al-Ti Superalloys: Impact of Atomic Order and Anti-Phase Boundaries. *Crystals* 9. 2019, 299. DOI: 10.3390/cryst9060299.
- [7] Friak, M., Vsianska, M., Sob, M. A Quantum-Mechanical Study of Clean and Cr-Segregated Antiphase Boundaries in Fe₃Al. *Materials* 12. 2019, 3954. DOI: 10.3390/ma12233954.
- [8] Friak, M., Golian, M., Holec, D., Koutna, N., Sob, M. An ab initio study of magnetism in disordered Fe-Al alloys with thermal antiphase boundaries. *Nanomaterials* 10. 2020, 44. DOI: 10.3390/nano10010044.
- [9] Friak, M., Cerny, M., Vsianska, M., Sob, M. Impact of Antiphase Boundaries on Structural, Magnetic and Vibrational Properties of Fe₃Al. *Materials* 13. 2020, 4884. DOI: 10.3390/ma13214884.
- [10] Abdoshahi, N., Spoerk-Erdely, P., Friak, M., Mayer, S., Sob, M., Holec, D. Ab initio study of chemical disorder as an effective stabilizing mechanism of bcc-based TiAl(+Mo). *Phys. Rev. Materials* 4. 2020, 103604. DOI: 10.1103/PhysRevMaterials.4.103604.
- [11] Friak, M., Lago, D., Koutna, N., Holec, D., Rebok, T., Sob, M. Multi-phase ELASTic Aggregates (MELASA) software tool for modeling anisotropic elastic properties of lamellar composites. *Computer Phys. Commun.* 2020, 247, 106863. DOI: 10.1016/j.cpc.2019.106863.

PLASMA AND PARTICLE PHYSICS

LASER-DRIVEN ACCELERATION OF CHARGED PARTICLES

Research institution
Czech Academy of Sciences,
Institute of Physics; ELI
Beamlines Centre; Czech
Technical University in
Prague; Kansai Photon Science
Institute, National Institutes
for Quantum and Radiological
Science and Technology;
Institute of Laser Engineering,
Osaka University; TAE
Technologies

Principal investigator
Martin Matys

Researchers
Petr Valenta, Mariana
Kecova, Katsunobu
Nishihara, Jan Psikal,
Timur Zh. Esirkepov,
James K. Koga,
Ales Necas, Gabriele
M. Grittani, Carlo M.
Lazzarini, Ondrej Klimo,
Georg Korn,
Sergei V. Bulanov

Project ID
OPEN-15-68

Introduction

Laser driven ion and electron acceleration has been the focus of scientific research for several decades now [1, 2]. The development of short pulse (multi)-petawatt class lasers with ultra-high field intensities, such as at the ELI Beamlines Centre, provides the future possibility of generation of high-quality beams of accelerated protons and electrons through laser target interaction, which could replace very expensive particle accelerators, e.g. in hospitals for biomedical applications [3].

Currently, laser-driven particle acceleration still needs to face several challenges, such as further improvement of produced particle beam quality and proper understanding of the inner mechanisms. Therefore, two specific schemes for ion and elec-

tron acceleration are investigated in this project. 1.) Interaction of high-intensity laser pulse with thin, high-density (solid), double layer targets with initial corrugation on the interface, resulting in generation of collimated high-density proton bunch. 2.) Interaction of high-intensity laser pulse with low-density (gas) targets for controlled production of electron beams.

We performed several demanding 3D and 2D particle-in-cell simulations and thereby demonstrated the quasi-monoenergetic behaviour of accelerated protons and explained the mechanism responsible for the wakefield periodical polarity reversal in electron acceleration analytically and via simulations. The results were presented at international scientific conferences and four publications were produced.

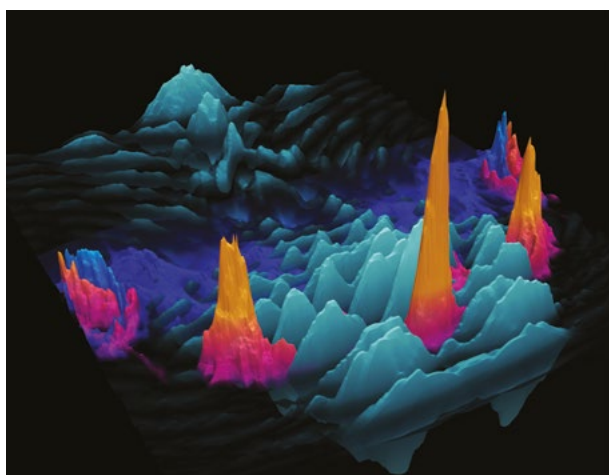
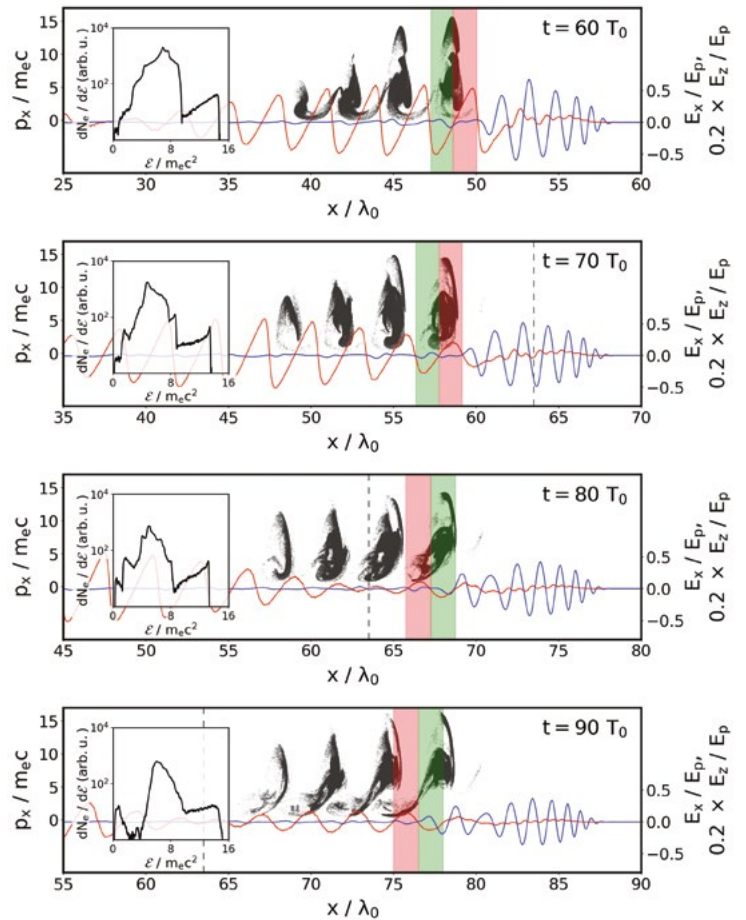


Figure 1. Visualisation of the simulation of the laser pulse (electric field in grey) interacting with a double-layer target with interface modulation (density of deuterium (heavy) and hydrogen (light) layer in blue and in red, respectively). The central proton bunch of relatively high density is enfolded by a propagating electric field preventing perpendicular particle expansion, and is accelerated by the laser radiation pressure to high energy.

Figure 2. Electron phase space (black), the on-axis wakefield, E_x (red), and the on-axis driver electric field, E_z (blue), at four successive time instants of the 3D particle-in-cell simulation. The corresponding inset shows the energy spectrum of electrons located in the first wake wave bucket behind the driver pulse, where N_e stands for the number of electron quasiparticles. For the first wake wave bucket, the accelerating and decelerating phases of the wakefield are highlighted by green and red stripes, respectively. The longitudinal coordinate at which the wakefield polarity reversal occurs is marked by the dashed line.



Methods and Results

Within the scope of this project, we have investigated the acceleration of ions and electrons using the particle-in-cell code EPOCH [4].

In the first branch of this work we investigate ion acceleration driven by high power laser pulse, relevant to cutting-edge laser systems such as ELI Beamlines (Czech Republic), APOLLON (France) and the proposed system SEL (China). In our simulations, the high-intensity laser pulse interacts with a double-layer target consisting of heavy and light materials. Relativistic versions of instabilities with Rayleigh-Taylor and Richtmyer-Meshkov like features [5] are developed at the interface between these two layers. The instability development can be at least partially controlled by prefabricated modulation introduced on the target interface, and by the use of a steep-front laser pulse. Initially small perturbations are then amplified during the laser-target interaction, leading

to the formation of low-density plasma regions and high-density bunches between them, corresponding to the initial target geometry, as can be seen in Figure 1. The plasma bunches are then accelerated from behind by the laser radiation pressure [6] as whole compact structures, while the laser pulse can propagate through the low density regions on their sides. The propagated part of the laser pulse then enfolds the central plasma bunch, retaining the particles within it. That results in a collimated quasi-monoenergetic proton beam with high average energy and low emittance.

Within the second branch of this work, we reveal that the wakefield, being excited by a few-cycle laser pulse in plasma, periodically reverses its polarity. As shown by the analytical model and computer simulations, the wakefield polarity reversal is caused by the dispersion and the corresponding difference between the propagation speed of the carrier and the envelope of the driving pulse. The discovery of this

phenomenon will be helpful in controlling the electron beam parameters, particularly in experiments carried out with high-repetition-rate laser systems.

Laser-wakefield acceleration (LWFA) is a well-established technique [7] for producing high-energy electrons in plasma. Within the framework of this concept, a relativistically intense laser pulse propagating through underdense plasma induces a strong electric field (wakefield) which in turn accelerates duly injected electrons. In fact, ionized plasmas can sustain electric fields several orders of magnitude larger than conventional radio-frequency technology, allowing one to substantially reduce the acceleration length. This paves the way towards a new generation of compact and cost-effective electron accelerators.

In this work, we show that the novel phenomenon of the wakefield polarity reversal occurs on spatial scales shorter than the dephasing length (i.e., the distance over which the electrons outrun the accelerating field), therefore significantly affecting the energies of accelerated electrons. In the nonlinear regime however, there may exist a case for which the polarity reversal length is equal to the dephasing length. In such a case, the dephasing limit is overcome and the electrons are accelerated until the energy of the driver pulse depletes. The study presented in this work is important for the LWFA under the conditions

relevant to present-day high-repetition-rate lasers, where the results obtained are useful for better control of the parameters of accelerated electron beams (e.g., by adjusting the initial phase of the driver or by controlling the phase of the electron injection).

Conclusion

We investigated the mechanisms of laser driven acceleration of charged particles under specific conditions. The collimated, quasi-monoenergetic proton beam of high energy was generated in our simulations of the interaction of a high intensity laser pulse with a high-density double-layer target having a modulated interface. The mechanism of the wakefield polarity reversal in electron acceleration from low-density targets was described by simulations and by an analytical model.

This project is directly related to solving the projects: High Field Initiative (CZ.02.1.01/0.0/0.0/15_003/0000 449) from the European Regional Development Fund and Czech Science Foundation project 18-09560S. The support of Grant Agency of the Czech Technical University in Prague, grant no. SGS19/192/OHK4/3T/14 is appreciated. Computational resources were provided by IT4Innovations National Supercomputing Center - LM2015070.

References

- [1] Bulanov, S. V., Esirkepov, T. Zh., Kando, M., et al. Relativistic mirrors in plasmas. Novel results and perspectives. *Physics – Uspekhi*. 2013, 56, 429. DOI: 10.3367/UFNe.0183.201305a.0449.
- [2] Esarey, E., Schroeder, C. B., Leemans, W. P. Physics of laser-driven plasma-based electron accelerators. *Rev. Mod. Phys.* 2009, 81(3), 122913. DOI: 10.1103/RevModPhys.81.1229.
- [3] Bulanov, S. V., Wilkens, J. J., Esirkepov, T. Z., et al. Laser ion acceleration for hadron therapy. *Phys. Usp.* 2014, 57(12), 1149–1179. DOI: 10.3367/ufne.0184.201412a.1265.
- [4] Arber, T. D., Bennett, K., Brady C. S., et al. Contemporary particle-in-cell approach to laser-plasma modelling. *Plasma Phys. Controlled Fusion*. 2015, 57, 113001. DOI: 10.1088/0741-3335/57/11/113001.
- [5] Zhou, Y. Rayleigh-Taylor and Richtmyer-Meshkov instability induced flow, turbulence, and mixing. I, *Phys. Rep.* 2017, 720–722, 1–136. DOI: 10.1016/j.physrep.2017.07.005.
- [6] Esirkepov, T., Borghesi, M., Bulanov, S. V., et al. Highly efficient relativistic-ion generation in the laser-piston regime. *Phys. Rev. Lett.* 2004, 92, 175003. DOI: 10.1103/PhysRevLett.92.175003.
- [7] Tajima, T., Dawson, J. M. Laser Electron Accelerator. *Phys. Rev. Lett.* 1979, 43, 267. DOI: 10.1103/PhysRevLett.43.267.
- [8] Matys, M., Nishihara, K., Kecova, M., Psikal, J., Korn, G., Bulanov, S. V. Laser-driven generation of collimated quasi-monoenergetic proton beam using double-layer target with modulated interface. *High Energy Density Physics*. 2020, 36, 100844. DOI: 10.1016/j.hedp.2020.100844.
- [9] Matys, M., Nishihara, K., Danielova, M., Psikal, J., Korn, G., Bulanov, S. V. Generation of collimated quasi-mono-energetic ion beams using a double layer target with interface modulations. *Proc. SPIE* 11037, 110370Z, 2019. DOI: 10.1117/12.2520951.
- [10] Valenta, P., Esirkepov, T. Zh., Koga, J. K., Nečas, A., Grittani, G. M., Lazzarini, C. M., Klimo, O., Korn, G., Bulanov, S. V. Polarity reversal of wakefields driven by ultrashort pulse laser. *Phys. Rev.* 2020, 102(5). DOI: 10.1103/PhysRevE.102.053216.
- [11] Valenta, P., Klimo, O., Grittani, G. M., Esirkepov, T. Zh., Korn, G., Bulanov, S. V. Wakefield Excited by Ultrashort Laser Pulses in Near-Critical Density Plasmas. *Proc. SPIE* 11037, 110370T, 2019. DOI: 10.1117/12.2521040.

PARTICLE-IN-CELL SIMULATIONS OF COMBINED THERMIONIC AND SECONDARY ELECTRON EMISSION

Research institution
Czech Academy of
Sciences, Institute of
Plasma Physics; KTH
Stockholm

Principal investigator
Michael Komm

Researchers
S. Ratynskaia,
P. Talias,
A. Podolnik

Project ID
OPEN-18-6

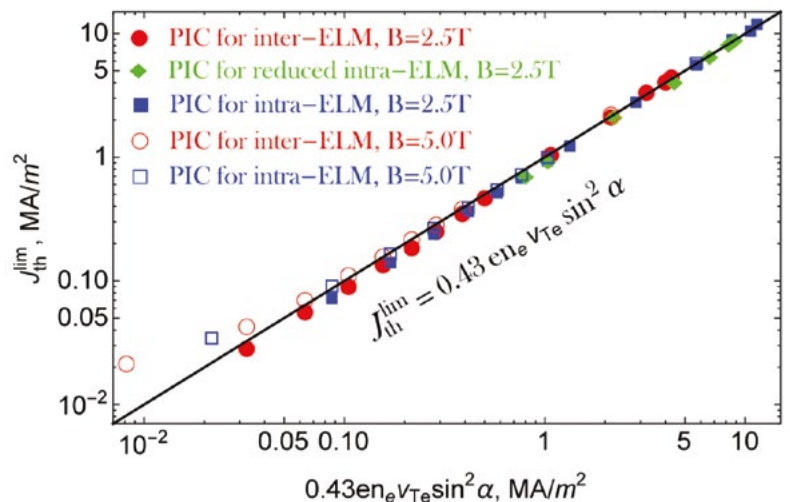
Introduction

One of the outstanding issues on the way towards power harnessing from nuclear fusion reactions is the problem of power exhaust; how to effectively remove the heat delivered by hot plasma to the plasma-facing components (PFCs) of the reactor. The interaction of plasma particles with solid surface of the PFCs is complex, especially in case of a tungsten surface at temperatures close to the melting point, where thermionic emission occurs, and also where secondary emission and electron back-scattering can become significant. The objective of our project is to study such interaction by means of particle-in-cell modeling in order to predict the behavior of the real PFCs in ITER tokamak. We focus on the properties of accidentally over-heated PFCs either due to the presence of off-normal events or mechanical misalignment of the PFCs.

Methods and Results

For our calculations, we have employed a cartesian 2D3V particle-in-cell code SPICE2 [1-3], which is capable of resolving the fine structure of a plasma sheath in front of solid surfaces. SPICE2 assumes a fixed magnetic field and calculates the electric field self-consistently, using a fast Poisson solver based on LU decomposition. Although the code operates in two spatial dimensions, the simulations effectuated within this project were essentially “1D-like” (with infinite surface at the lower boundary) and the dimension running tangentially to surface served only to improve the statistics of the calculations. Particle-in-cell simulations are notorious for being computationally demanding, and indeed the typical runtime of the simulations was about 1 week (running on 1-2 nodes). SPICE2 does not have very strong scaling with number of cores (maximum 64 cores), however

Figure 1. Scaling of the escaping thermionic current and the proposed scaling formula. Figure reprinted from [6].



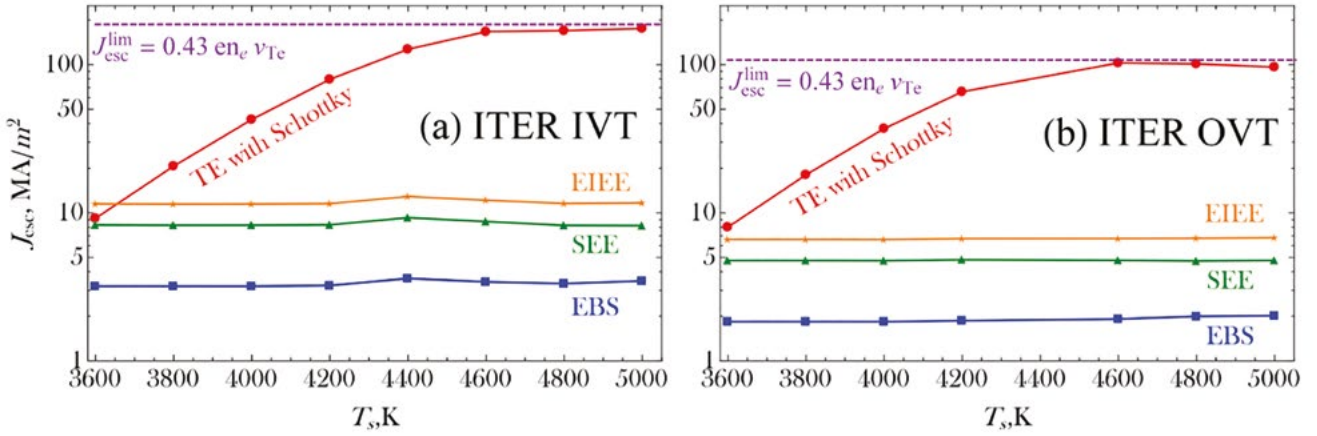


Figure 2. Escaping currents of TE, SEE, and EBS as a function of surface temperature for the inner (A) and outer (B) divertor target in the ITER tokamak. Figure reprinted from [8].

since we had to perform a large number of simulations with scans in input parameters (mainly surface temperature), this was not an issue for this particular task.

The primary objective of the work was to complement a previously performed series of simulations (project OPEN-12-7)[1-2], which aimed to characterize the magnitude of the escaping current of thermionic emission j_{esc} in varying plasma conditions and under different orientations of magnetic field. The plasma conditions were based on those achieved in experimentation with melting of tungsten lamellas in tokamak Asdex Upgrade [4]. We were able to identify the functional dependence of j_{esc} on the angle of incidence and to extend the existing formula developed by Takamura [5] for unmagnetized plasmas (as shown in Figure 1):

$$j_{\text{esc}} [\text{MA/m}^2] = 0.43 e n_e v_{Te} \sin^2 \alpha,$$

Where n_e is the plasma density v_{Te} is the electron thermal velocity, and α is the angle of incidence of the magnetic field with respect to the surface. This extended formula [6] is now implemented in the MEMOS-U code [7], which calculates the motion of molten tungsten in the tokamak environment.

The second task was to study the interplay of thermionic emission (TE) with secondary electron emission (SEE) and electron back-scattering (EBS). These processes can become important in ITER during off-normal events, such as edge-localised modes

(ELMs), when the plasma temperature is expected to exceed 100 eV. In order to perform such simulations, a detailed model of both SEE and EBS needed to be implemented in SPICE2 [8]. Once this activity was completed, we targeted simulations with a normal incidence of B field, corresponding to a molten leading edge of an accidentally misaligned divertor plasma-facing component (which is the easiest to interpret and cross-check). A series of simulations with varying surface temperature were performed, each yielding escaping currents for each process of electron emission. The results have shown that in the studied configuration, all the processes are virtually independent, meaning that the escaping currents are not affected by the presence of other emission processes (as shown in Figure 2). At the same time, for temperatures in the vicinity of the tungsten melting point, the escaping current of SEE is of comparable magnitude for the TE current, and this should be taken into account for modelling of the molten layer motion (which is driven primarily by the $j \times B$ force).

Conclusion

We have performed studies of the escaping current from thermionic emission, secondary electron emission and electron back-scattering in magnetized plasmas under conditions which are expected in ITER during ELMs. We have observed that all three processes are practically independent, however, the escaping current generated by SEE should be taken into account for modelling of the molten layer motion.

References

- [1] Komm, M., et al. On thermionic emission from plasma-facing components in tokamak-relevant conditions. *Plasma Phys. Control.* 2017, 59. DOI: 10.1088/1361-6587/aa78c4.
- [2] Komm, M., et al. Simulations of thermionic suppression during tungsten transient melting experiments. *Phys. Scripta.* 2017, T170. DOI: 10.1088/1402-4896/aa9209.
- [3] Komm, M., et al. Particle-in-cell simulations of the plasma interaction with poloidal gaps in the ITER divertor outer vertical target. *Nucl. Fusion.* 2017, 57(12). DOI: 10.1088/1741-4326/aa8a9a.
- [4] Komm, M., et al. Experiments on transient melting of tungsten by ELMs in ASDEX Upgrade. *Nucl. Fusion.* 2018, 58(2). DOI: 10.1088/1741-4326/aa9a05.
- [5] Takamura, S., et al. Space-Charge Limited Current from Plasma-Facing Material Surface. *Contrib. Plasma Phys.* 2004, 44(1-3), 126-137. DOI: 10.1002/ctpp.200410017.
- [6] Komm, M., et al. Space-charge limited thermionic sheaths in magnetized fusion plasmas. *Nucl. Fusion.* 2020, 60(5). DOI: 10.1088/1741-4326/ab7c27.
- [7] Thoren, E., et al. The MEMOS-U code description of macroscopic melt dynamics in fusion devices. *Plasma Phys. Control.* 2021, 63(3). DOI: 10.1088/1361-6587/abd838.
- [8] Toliás, P., et al. Origin and nature of the emissive sheath surrounding hot tungsten tokamak surfaces. *Nucl. Mat. Energy.* 2020, 25. DOI: 10.1016/j.nme.2020.100818.

SUPERCOMPUTING IN SCIENCE AND ENGINEERING 2019-2020

IT4Innovations National Supercomputing Center
Ostrava, Czech Republic

ISBN 978-80-248-4567-8

